

Development of UV MCP Detectors

Dissertation

der Mathematisch-Naturwissenschaftlichen Fakultät
der Eberhard Karls Universität Tübingen
zur Erlangung des Grades eines
Doktors der Naturwissenschaften
(Dr. rer. nat.)

vorgelegt von
Dipl. Phys. Lauro Conti
aus Berlin

Tübingen
2021

Gedruckt mit Genehmigung der Mathematisch-Naturwissenschaftlichen
Fakultät der Eberhard Karls Universität Tübingen.

Tag der mündlichen Prüfung:	21.06.2021
Dekan:	Prof. Dr. Thilo Stehle
1. Berichterstatter:	Prof. Dr. Klaus Werner
2. Berichterstatter:	Prof. Dott. Andrea Santangelo

Abstract

With its excellent instruments, the Hubble Space Telescope (HST) has served the UV community for over thirty years, providing the opportunity to acquire data for its projects. With the HST expected to be in operation for only five more years and the future James Webb Space Telescope not covering the UV spectral region, there may be an observational gap in the UV. Delays in the WSO-UV space telescope and long lead times on even larger missions mean that this gap can only be filled by smaller, more specialized telescopes. In turn, the instruments installed in these smaller telescopes must meet relatively stringent space, power, and mass requirements.

Therefore, an imaging microchannel plate (MCP) detector for the near to far ultraviolet spectral range is being developed at the Institute for Astronomy and Astrophysics Tübingen (IAAT), combining high spatial resolution with relatively low mass (3 kg), power consumption (15 W) and size. The detector is also photon counting and does not require active cooling to achieve a dark count rate superior to that of cooled CCDs.

The focus of this work is to present the steps in the development of the detector. In the first chapter an overview of the design of the detector is given. The setup must allow to determine the position of up to 300000 UV photons per second with a positional accuracy of about 20 μm . The working principle of the detector electronics is only outlined. Instead, the components installed in the detector head and their characteristics are described in detail. Particularly worth mentioning are the possibilities offered by the use of MCPs, in which glass capillary arrays are coated using atomic layer deposition. In addition to a longer lifetime and a further reduced dark count rate, this is primarily their temperature resistance of 450°C. With optimised annealing processes in the manufacturing process of a resistive layer, these temperatures can be even higher. This enables the growth of GaN on such MCPs and the activation of getter films in the detector head.

The detector uses a photocathode with negative electron affinity to convert incident UV photons into photoelectrons. This combines a high conversion rate, called quantum efficiency (QE), with a low dark current. The focus of

the corresponding chapter is on the detailed description of the external photoelectric effect in the case of caesium-activated and p-doped gallium nitride (GaN) photocathodes.

In the third part of this work, the experimental setup and the results of the performed experiments are presented. The first experiment is the sealing of diodes with 2.5 cm diameter substrates and caesium activated photocathode. Two diodes were successfully sealed, and it was shown that the photocathode does not degrade. The main requirement for successful sealing is properly coated sealing surfaces. The caesium telluride photocathodes needed for the sealing tests are fabricated and measured in another ultra-high vacuum chamber. A further series of experiments involves optimizing the growth and activation parameters of GaN photocathodes on magnesium fluoride (MgF_2) substrates. Since MgF_2 is transparent in a broader spectral range compared to sapphire and even includes the Lyman- α line, its use in an encapsulated UV detector is usually advantageous. However, poor results are initially obtained on MgF_2 compared to GaN on sapphire substrates. This is mainly because the parameters obtained from cleaning or annealing sapphire substrates cannot be easily transferred to MgF_2 . For example, MgF_2 is more sensitive to the high temperatures during growth, annealing, and bakeout. Therefore, many parameters need to be optimised in the fabrication of such a photocathode. Experiments include optimization of the growth temperature and p-doping of the corresponding films. After optimization, it was shown that a QE equally high as found in literature for comparable films on sapphire is obtained. This means that these films are suitable to achieve a QE of 20–30 % in semi-transparent mode, provided that an ohmic contact can be created by “soft annealing”.

Finally, high-resolution STIS spectra from the hot white dwarfs WD0455-282, WD0621-376, and WD2211-495 are analysed. There are three main goals in this analysis. First, when building a detector, a good understanding of the properties of the measured data obtained with the detector should also be acquired. Second, the main scientific goal of a mission is to use the instrument with the IAAT detector to acquire data from astronomical objects of interest. The knowledge needed to analyse and interpret these data can already be acquired with the analysis of existing data. Finally, the obtained results are compared with the analyses of the same spectra found in literature.

Zusammenfassung

Mit seinen exzellenten Instrumenten hat das Hubble-Weltraumteleskop der UV-Gemeinschaft über dreißig Jahre lang gedient und die Möglichkeit geboten, Daten für ihre Projekte zu erfassen. Da das Hubble-Teleskop voraussichtlich nur noch fünf Jahre in Betrieb sein wird und das James Webb Space Teleskop den UV-Spektralbereich nicht abdeckt, könnte eine Beobachtungslücke im UV-Bereich entstehen. Verzögerungen beim WSO-UV-Weltraumteleskop und lange Vorlaufzeiten bei noch größeren Missionen bedeuten, dass diese Lücke nur durch kleinere, spezialisiertere Teleskope geschlossen werden kann. Die in diesen kleineren Teleskopen installierten Instrumente müssen wiederum relativ strenge Platz- und Masseanforderungen erfüllen. Daher wird am Institut für Astronomie und Astrophysik Tübingen (IAAT) ein abbildender Mikrokanalplatten-Detektor (MCP) für den nahen bis fernen ultravioletten Spektralbereich entwickelt, der hohe räumliche Auflösung mit relativ geringer Masse (3 kg), Leistungsaufnahme und Größe kombiniert. Der Detektor ist zudem photonenzählend und benötigt keine aktive Kühlung, um eine geringe Dunkelzählrate zu erreichen.

Der Schwerpunkt dieser Arbeit liegt in der Darstellung der Schritte bei der Entwicklung des Detektors. Im ersten Kapitel wird ein Überblick über den Aufbau des Detektors gegeben. Der Aufbau muss es ermöglichen, die Position von bis zu 300000 UV-Photonen pro Sekunde mit einer Genauigkeit von jeweils etwa $20\ \mu\text{m}$ zu bestimmen. Das Funktionsprinzip der Detektorelektronik ist nur skizziert. Stattdessen werden die im Detektorkopf eingebauten Komponenten und deren Eigenschaften detailliert beschrieben. Besonders erwähnenswert sind die Möglichkeiten, die sich durch die Verwendung von MCPs ergeben, bei denen Glaskapillararrays mittels Atomlagenabscheidung beschichtet werden. Neben einer längeren Lebensdauer und einer nochmals reduzierten Dunkelzählrate ist dies vor allem ihre Temperaturbeständigkeit von 450°C . Dies ermöglicht das Wachstum von Galliumnitrid (GaN) auf solchen MCPs und die Aktivierung von Getterschichten im Detektorkopf.

Der Detektor verwendet eine Photokathode mit negativer Elektronenaffinität, um einfallende UV-Photonen in Photoelektronen umzuwandeln. Diese kombiniert eine hohe Umwandlungsrate, die sogenannte Quanteneffizienz (QE), mit einem geringen Dunkelstrom. Der Schwerpunkt des entsprechenden

Kapitels liegt auf der detaillierten Beschreibung des externen photoelektrischen Effekts im Falle von Cäsium-aktivierten und p-dotierten GaN-Photokathoden.

Im dritten Teil dieser Arbeit werden der Versuchsaufbau und die Ergebnisse der durchgeführten Experimente vorgestellt. Das erste Experiment ist die Versiegelung von Dioden mit 2,5 cm durchmessenden Substraten und cäsiumaktivierter Photokathode. Zwei Dioden wurden erfolgreich versiegelt und es wurde gezeigt, dass die Photokathode nicht degradiert. Die Hauptvoraussetzung für eine erfolgreiche Versiegelung sind richtig beschichtete Versiegelungsflächen. Die für die Versiegelungstests benötigten Cäsiumtellurid-Photokathoden werden in einer weiteren Ultrahochvakuumkammer hergestellt und vermessen. Eine weitere Versuchsreihe umfasst die Optimierung der Wachstums- und Aktivierungsparameter von GaN-Photokathoden auf Magnesiumfluorid (MgF_2)-Substraten. Da MgF_2 im Vergleich zu Saphir in einem breiteren Spektralbereich transparent ist und sogar die Lyman- α -Linie einschließt, ist sein Einsatz in einem gekapselten UV-Detektor meistens von Vorteil. Auf MgF_2 werden im Vergleich zu GaN auf Saphirsubstraten aber zunächst schlechtere Ergebnisse erzielt. Das liegt vor allem daran, dass die Parameter, die man beim Reinigen oder Glühen von Saphirsubstraten verwendet, für MgF_2 nicht einfach übernommen werden können. Zum Beispiel ist MgF_2 temperaturempfindlicher, was das Wachstum, Glühen und Ausheizen erschwert. Es wurde gezeigt, dass nach der Optimierung eine gleich hohe QE erreicht wird, wie in der Literatur bei vergleichbaren Schichten auf Saphir. Dies bedeutet, dass diese Schichten geeignet sind um im semi-transparenten Modus eine QE von 20–30 % zu erreichen, sobald ein ohmscher Kontakt durch „sanftes Glühen“ hergestellt werden kann.

Abschließend werden hochaufgelöste STIS-Spektren von den heißen Weißen Zwergen WD0455-282, WD0621-376 und WD2211-495 analysiert. Es gibt drei Hauptziele bei dieser Analyse. Erstens sollte beim Bau eines Detektors auch ein gutes Verständnis für die Eigenschaften der Messdaten, die mit dem Detektor gewonnen werden, erworben werden. Zweitens ist das wissenschaftliche Hauptziel einer Mission, mit dem Instrument Daten zu erfassen, die dann analysiert werden können. Mit der Analyse bestehender Daten kann das dafür benötigte Wissen angeeignet werden. Schließlich werden die erhaltenen Ergebnisse mit den in der Literatur gefundenen Analysen der gleichen Spektren verglichen.

Contents

1	Introduction and detector parts	1
1.1	Detector overview	1
1.1.1	Detector concept and parts	1
1.1.2	Detection chain	4
1.2	Detector head parts	6
1.2.1	Detector window	7
1.2.2	Micro channel plates	17
1.2.3	Anode	25
1.2.4	Ceramics and Kovar body	29
1.2.5	Getter and getter activation	30
1.3	Tube sealing	31
1.3.1	Wetting of materials	31
2	Photocathodes	35
2.1	Photocathode theory	37
2.1.1	Band structure of crystals	37
2.1.2	Band gap, solar-blindness and conductivity	40
2.1.3	Manipulating the band structure and three-step model	41
2.2	Optimization of NEA photocathodes	44
2.2.1	Semi-transparent and opaque mode	44
2.2.2	Low-energy cutoff and high-energy drop	50
2.2.3	Reflectivity of photocathodes	53
2.2.4	Electric field and temperature	57
2.2.5	Longevity of the photocathode	62

3	Measurements and results	67
3.1	Laboratory setup	67
3.1.1	UHV system	67
3.1.2	Residual gas measurements	75
3.1.3	Nitrogen box	78
3.2	Sealed diode bodies	79
3.2.1	Sealing process	79
3.2.2	Change in photocathode properties due to sealing	80
3.2.3	Change in photocathode properties after sealing	83
3.3	GaN photocathodes – measurements	84
3.3.1	Preparation of suitable (0 0 1) magnesium fluoride sub- strates for GaN growth	84
3.3.2	Activation and QE measurements of undoped GaN films	87
3.3.3	Activation and QE measurements of p-type GaN on ma- gnesium fluoride	95
3.4	CsTe photocathodes – measurements	100
3.4.1	NiCr thickness tests with samples CsTe-A1 to A5	101
3.4.2	Samples CsTe-B1 to CsTe-D1	104
3.5	Discussion of the measurement results	110
3.5.1	Discussion and next steps for GaN samples	110
3.5.2	Discussion and next steps for caesium telluride samples .	112
4	Analysis of UV spectra of hot white dwarfs	113
4.1	Stellar evolution and fundamental parameters of stars	113
4.2	Stellar atmospheres and their modelling	117
4.2.1	Observational data	120
4.2.2	Basic model without Fe-lines	121
4.2.3	Atmospheric model including Fe lines	128
4.2.4	Comparison of the results and discussion	128
5	Conclusions	133
A	Supplements to the photocathode measurements	135
B	Supplements to the analysis of the UV spectra of hot white dwarfs	139

List of Figures

1.1	CAD drawings of the main parts of the detector	2
1.2	Schematic diagram of the detector electronics	3
1.3	Rendered graphics of the whole detector assembly with a closed detector design	4
1.4	Working principle of the MCP detector	6
1.5	<i>Beetle</i> hybrid board with <i>Beetle</i> chip	7
1.6	Temperature dependent cut-off wavelength of UV window materials (Hunter and Malo, 1969)	8
1.7	Transmittance of a MgF ₂ thin-film	9
1.8	Metallization of laser polished MgF ₂ samples	11
1.9	MgF ₂ samples are cleaned with an argon plasma during glow discharge	13
1.10	Sheet resistance over the film thickness of titanium, nickel-chrome and gold	14
1.11	Transmittance of ITO in the UV	15
1.12	Transmittance of a 5 nm thick layer of silver, gold, nickel and chrome	16
1.13	Sketch of the multiplication of an electron into an electron cloud in a stack of two MCPs	18
1.14	Manufacturing steps of conventional MCPs	19
1.15	“Perfectly conformal films” grown with ALD by Ritala et al. (1999)	21
1.16	Sectional view through an ALD-MCP (Schindhelm et al., 2017)	21
1.17	MCP gain vs. voltage from a test report of a chevron pair of ordered Incom Inc. ALD-MCPs	23
1.18	Temperature dependent resistivity of MCPs	25

1.19	Working principle of a WSA	26
1.20	Render of crossing strips (golden) with insulating layers (white) (Diebold et al., 2013)	28
1.21	Principle of the coplanar CSA	28
1.22	Section of a high resolution image of an CSA	29
1.23	Ceramics and Kovar body with the anode	30
1.24	Definition of the contact angle between a solid surface and a droplet	32
1.25	DSA measurements of In-Bi on Kovar	33
1.26	DSA measurements of In-Bi on gold	34
2.1	Examples for planes described by the Miller indices	38
2.2	Probability densities of electrons in a crystal	39
2.3	Band structure of hexagonal GaN	41
2.4	Band structure of a p-doped NEA photocathode and three-step model of photoexcitation	42
2.5	Photocathode modes: semi-transparent and opaque mode	46
2.6	Absorption coefficient of $\text{Al}_x\text{Ga}_{1-x}\text{N}$	50
2.7	Monte Carlo simulations of photoexcitation in a p-doped but unactivated GaN photocathode by Marini et al. (2018a)	51
2.8	Relative QE of a GaN Schottky photodiode from 5 to 400 nm	54
2.9	Reflectivity $R(\lambda, \phi)$ of GaN for incident light in vacuum	56
2.10	SEM images of silicon nanowires (SiNWs) and their reflectivity	57
2.11	Schematic energy band diagram and QE of grade doped GaN	59
2.12	Left: Relative quantum efficiencies of GaN samples during ac- tivation and stability tests. Right: The stopping power of elec- tronic processes (Se) and interactions with atomic cores (Sn) plotted vs. the square root of the energy (\propto velocity) of ionizing particles	64
3.1	Cathode Vessel and Detector Vessel during the assembly of the heating tent	68
3.2	Cross sectional views of the Cathode Vessel	69
3.3	Three consecutive measurements of the lamp spectrum between 170 nm to 300 nm	71

3.4	NIST calibration compared to PTB calibration of Si-photodiode AXUV-100G, 09-911	73
3.5	Transfer fork and cathode transfer	74
3.6	Partial pressure in mbar over the AMU per charge	77
3.7	Partial pressures of molecules that have the greatest effect on the growth or activation of the photocathode	77
3.8	The most important parts to obtain a defined atmosphere in the current version of the nitrogen box	79
3.9	Diode body for sealing tests of 2.50 cm diameter samples in va- cuum with molten indium alloy	81
3.10	QE of photocathode CsTe-C2 before and after sealing	82
3.11	QE measurements versus wavelength of two sealed diode bodies with caesium telluride photocathode over a period of two weeks and several months	83
3.12	Metallization layer in cross form on two substrates with overly- ing GaN layer	85
3.13	Sample S008 and S009 before and after activation	88
3.14	Photocurrent during activation of S008	89
3.15	Photocurrent during activation of S009	90
3.16	QE of sample GaN S008 with Cs/O/Cs activation film	92
3.17	Sample GaN-S010 after removal from the activation chamber	93
3.18	Photocurrent of sample GaN-S013 and S011 near the oxygen cut-off	96
3.19	QE measurement of S011	97
3.20	Activation of the p-doped sample GaN-S030	98
3.21	Enhancement factor of the p-doped GaN samples S030–S033	99
3.22	Activation curve of samples CsTe-A1 to A5	103
3.23	Samples CsTe-A1 to A5 after activation	104
3.24	QE measurements of samples CsTe-A1 to A5	105
3.25	Photocurrent of CsTe-D1 shortly after activation and the follo- wing days	107
3.26	QE of CsTe-D1 shortly after activation and the following days	108
3.27	Internal QE of the photocathode CsTe-D1 and assumed trans- mittance of NiCr	109

3.28	Detector window with GaN film but without metallisation . . .	110
4.1	Spectrum of the red giant star Arcturus	114
4.2	Hertzsprung-Russell diagram of 32 open clusters	115
4.3	Evolutionary tracks through the HRD of stars with initial masses of 1.0 to 5 M_{\odot}	116
4.4	An estimation on the percentage of the origin of different elements due to different nucleosynthesis processes	117
4.5	Cooling tracks of DA-type white dwarfs with corresponding masses in M_{\odot}	118
4.6	Schematics how photospheric models were obtained with the goal of fitting the observational data of the three white dwarfs .	119
4.7	WD 0455-282, WD 0621-376, WD 2211-495 and surroundings .	120
4.8	Synthetic spectrum of two model atmospheres differing in iron abundance, and STIS observation data of WD 0455-282	122
4.9	Synthetic spectrum of a model atmosphere and the STIS observation including O IV lines on the left and an O IV on the right	123
4.10	Ionization fractions of iron versus column density in a model atmosphere of WD 0621-376	124
4.11	Temperature structure of models including Fe	125
4.12	Log-log diagram of the flux over the wavelength to determine the colour excess E_{B-V} of WD 2211-495	126
4.13	Rectification of a spectrum	129
4.14	Synthetic spectra including O and Fe lines and observational data of WD 2211-495	130
A.1	Interpolation of the PTB calibration data with error bars	135
B.1	Plot for determination of E_{B-V} of WD 0455-282	139
B.2	Detailed plot for the determination of E_{B-V} of WD 0455-282 . .	140
B.3	Plot for determination of E_{B-V} of WD 0621-376	140
B.4	Detailed plot for the determination of E_{B-V} of WD 0621-376 . .	141
B.5	Plot to determine the O abundance and T_{eff} of WD 0455-282 .	141

B.6	Plot to determine the Fe abundance of WD 0455-282. The synthetic spectra with +3 kK and -6 kK with respect to T_{eff} are plotted for comparison	142
B.7	Plot to determine the O abundance and T_{eff} of WD 0621-376	142
B.8	Plot to determine the Fe abundance of WD 0621-376. The synthetic spectra with +3 kK and -3 kK with respect to T_{eff} are plotted for comparison	143
B.9	Plot to determine the O abundance and T_{eff} of WD 2211-495	143
B.10	Plot to determine the Fe abundance of WD 2211-495. The synthetic spectra with +3 kK and -3 kK with respect to T_{eff} are plotted for comparison	144
B.11	Plot of the STIS data presented in Tab. 4.1	145
B.12	Plot of the STIS data listed in Tab. 4.1 of WD0621-376	146
B.13	Plot of the STIS data given in Tab. 4.1 of WD2211-495	147
B.14	Synthetic spectra of a region with Fe lines with parameters from Preval et al. (2019) and observational data of WD 0455-282	148
B.15	Synthetic spectra of a region with Fe lines parameters from Preval et al. (2019) and observational data of WD 0621-376	148
B.16	Synthetic spectra of a region with O lines parameters from Preval et al. (2019) and observational data of WD 0455-282	149
B.17	Synthetic spectra of a region with O lines parameters from Preval et al. (2019), own parameters and observational data of WD 0621-376	149

List of Tables

1.1	Cut-off wavelengths at room temperature for UV window materials	8
1.2	Parameters of currently used MCPs	18
3.1	Growth parameters of samples S008–S013	87
3.2	Growth parameters of GaN samples S030–S033 and enhancement factor	96
3.3	Overview about samples CsTe-A1 to A5	102
3.4	Overview on samples CsTe-B1 to CsTe-D1	106
4.1	List of datasets which were used as observational data	121
4.2	Photometric measurements and calculated fluxes of WD 0455-282, WD 0621-376 and WD 2211-495	127
4.3	Values for E_{B-V} for the three analysed WDs	128
4.4	Comparison of fit- and model-parameters	131
A.1	List of the partial pressures plotted in Fig. 3.7	137

Chapter 1

Introduction and detector parts

1.1 Detector overview

The following Section provides an overview of the appearance, dimensions and the working principles of the current micro channel plate (MCP) detector. At least three units are required to operate the detector: the detector head, the read-out electronics (ROE) and a high-voltage power supply (HV supply). Further details on the dimensions, interfaces and tasks of these units can be found in Sect. 1.1.1. Sect. 1.1.2 provides an overview of the working principles of an MCP detector, taking the current detector design of the ‘*Institut für Astronomie und Astrophysik Tübingen*’ (IAAT) as an example.

1.1.1 Detector concept and parts

Detector concept

This section will take a close look at the concept of the current photon counting UV MCP detector for imaging and spectroscopy. It is a flight-capable detector intended for satellite or balloon missions, and is radiation-hardened, e.g., by using space-qualified (SQ) components in the read-out electronics. Details of a stratospheric balloon mission using the current UV detector as an imaging detector are presented in Maier et al. (2018) or Pahler et al. (2020).

When designing the detector, the goal was to have a detector assembly that will need only slight adjustments depending on the requirements of the specific mission. Fig. 1.1 shows the detector units that are needed for every mission: the

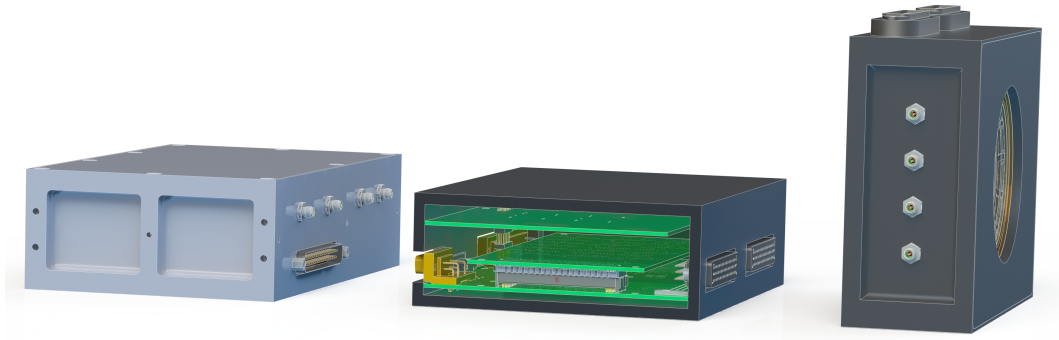


Fig. 1.1: CAD drawings of the main parts of the detector. From left to right: HV supply, cross sectional view through the read-out electronics and detector head unit

detector head, HV supply and the ROE with an integrated power supply. For example, the HV supply has a laboratory, a space-flight and a balloon-flight version, but they differ only slightly, e.g. in terms of the coatings or connectors.

The concept of the detector electronics is illustrated in Fig. 1.2. The whole UV detector has only one electronic interface to the back-end¹ electronics and one external power cable. Minimizing the number of external interfaces saves time and reduces the risk of errors in scientific space missions, which is why our detector is also designed according to this principle.

Detector parts

Fig. 1.2 presents the electronic schematics of the detector and takes a close look at the three units it consists of.

Inside of the detector head unit, the detector head is mounted with the *Beetle* hybrid board (Pfeifer et al., 2014) on its backside. In Chap. 1.1.2 a detailed description of its working principles will be provided, in 1.2 we will examine the parts inside of the detector head in detail. The detector head unit is connected to the HV supply via four HV cables.

The read-out electronics contains three boards as shown in Fig. 1.1. The power board has a single external power input and provides power to the HV supply, the *Beetle* hybrid board and the Field Programmable Gate Array (FPGA) board. On the static RAM (SRAM) board radiation hardened volatile

¹A synonymous term is “Instrument Control Unit” (ICU)

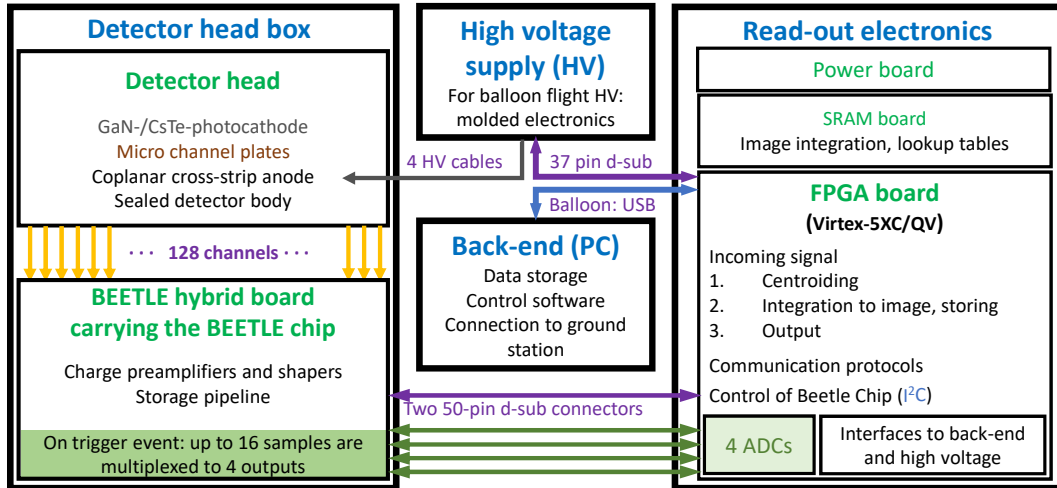


Fig. 1.2: Schematic diagram of the detector electronics. The back-end is a laboratory computer or the instrument control unit of a specific mission

memory can be used to store look-up tables or buffer image data. SRAM was chosen as it can be read out or be written to with a very low latency by the space-grade version of a VIRTEX-5 FPGA. Via two 50-pin d-sub connectors, the FPGA board processes the signals it receives by the detector head and controls the parameters of the charge preamplifier and shaper chip. The control of the voltage output of the HV supply is achieved by a 37-pin d-sub connection. A serial interface using standard USB connectors or d-sub connectors connects the ROE to the back-end electronics, making it possible to transfer data, e.g. imaging data, housekeeping data and commands.

The dimensions of the whole detector assembly are comparable to a “shoe box” as shown in Fig. 1.3. Cables and mounting brackets for fixing the detector parts to a telescope instrument platform are missing in the otherwise complete render graphics. The transparent detector window on top of the detector head is visible through its light reflection and implies that the detector head has a closed design (see Sect. 2.2.1). It would also be possible to use an open design (Sect. 2.2.1) with a simple door that can be opened under space conditions or a gate valve on top.

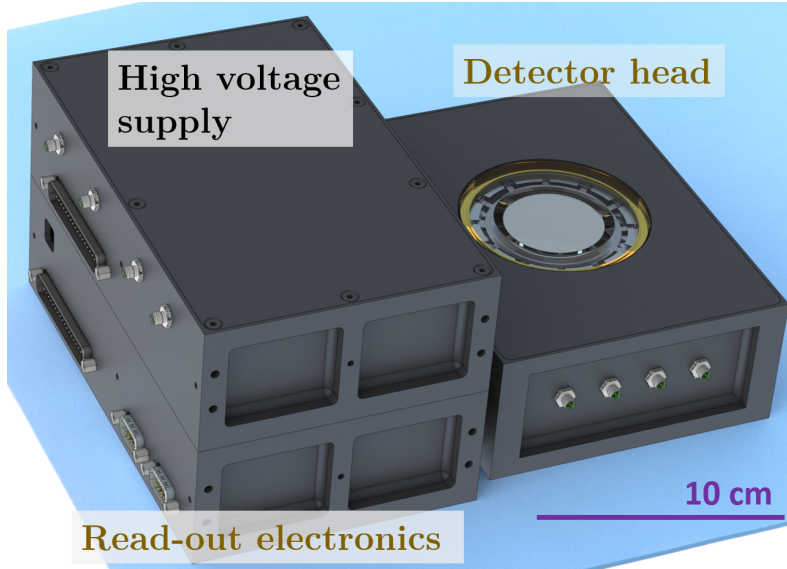


Fig. 1.3: Rendered graphics of the whole detector assembly with a closed detector design

1.1.2 Detection chain

This section will briefly go through the detection chain in the detector head of the current detector. The goal is to get an overview over the processes that are taking place to measure the positions of up to 300,000 UV-photons per second. The detector creates images by integrating single photon events. Therefore, it is sufficient to follow the processes triggered by a single photon. The numbers of the following enumeration will refer to the numbers in Fig. 1.4:

1. On its way to the photosensitive layer a photon first has to pass through the *detector window*, as the current detector is sealed (Sect. 2.2.1). To lose as few photons as possible, the window needs to have a low reflectivity and a high transmittance in the desired wavelength range. For the current detector, magnesium fluoride (MgF_2) is used as a window material with a reflectivity of only a few percent and a transmittance of more than 90 percent between 400 nm and a cut-off wavelength at about 120 nm (for details see Chap. 1.2.1).
2. After passing through the detector window the photon is inside of the sealed detector and will enter the *photocathode*. The purpose of using a photocathode is to maximize the probability of converting the photon

into a photo-electron. The conversion is accomplished in three steps, the first step is the excitation of an electron into the conduction band of the photocathode crystal by an incident UV photon. In a second step, the electron is accelerated to the surface with the help of an electric field and can tunnel into the vacuum in the third step due to a negative electron affinity (NEA) of the photocathode. GaN is to be used as the photocathode material for the detector, this has the advantage of a high quantum efficiency over a wide wavelength range. For a detailed discussion of possible photocathode positions and the properties of NEA photocathodes, see Sect. 2.

3. The next step in the detection chain is to multiply the photo-electron into an electron cloud while maintaining its position information. This is possible with the help of so called *micro channel plates*. In the current IAAT UV detector a single photo-electron is multiplied into an electron cloud of about 10^5 electrons. In Sect. 1.2.2 a more elaborate description of different MCP types used in the current detector can be found.
4. In the fourth step outlined in Fig. 1.4 the electron cloud is accelerated towards a *cross-strip anode* (CSA) and deposits a certain amount of charge on each of the individual 128 channels of the CSA. The CSA is discussed in Sect. 1.2.3.

In case of an event, the charge deposited on each individual channel of the CSA must be amplified and measured very precisely and with a time resolution that is sufficient to achieve the desired count rate for the detector. This sophisticated charge amplification and shaping is achieved by the *Beetle* chip (Löchner and Schmelling, 2006) carried by the *Beetle* hybrid board (Pfeifer et al., 2014, Fig. 3). The analogue charge data is multiplexed and sent to four analogue-to-digital converters (ADCs) on the FPGA board. On a current laboratory version of a Virtex-4 FPGA board the charge data is cached and sent to a PC in raw format, where different centroiding algorithms can be used to analyse the charge data and determine its centre of charge. The progress made in finding simple and yet very precise centroiding algorithms are discussed in detail in Hanke (2018). Also, a promising fully integer-based, fast and precise algorithm could be implemented on a commercial Virtex-7 board soon. The

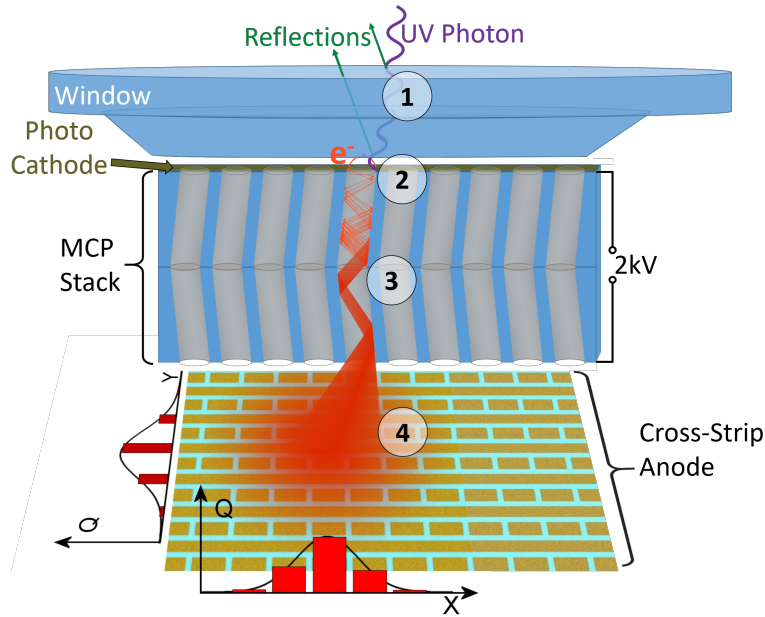


Fig. 1.4: Working principle of the MCP detector

centroiding algorithms will allocate each event an x and y position. The pixel data and a timestamp can then be sent directly to a back-end computer or it is integrated into an image in the SRAM of the FPGA board before being sent to the back-end computer (ICU).

1.2 Detector head parts

This chapter will deal in detail with the properties, composition and functionality of the parts installed in the detector head. Sect. 1.2.1 describes the numerous conditions that must be met in order to obtain an optimal UV window.

In the field of MCPs much progress has been achieved in the last couple of years. The advantages and disadvantages of conventional MCPs and the results achievable with technologies like the atomic layer deposition are presented in Sect. 1.2.2. The anode of an UV MCP detector is used to collect the charges of the charge cloud leaving the bottom of the MCP and is discussed in 1.2.3. Two anode designs are presented, the cross-strip anode (CSA) and the wedge and strip anode as it was used in the MCP detector for the ORFEUS² telescope,

²Orbiting and Retrievable Far and Extreme Ultraviolet Spectrometer

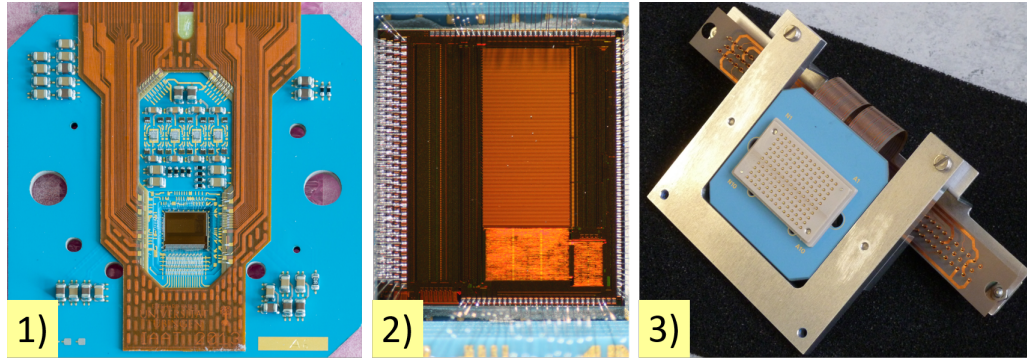


Fig. 1.5: *1)*: Front view of the *Beetle* hybrid board with *Beetle* chip. *2)*: *Beetle* chip connected via bond wires to the anode, the two 50-pin d-sub connectors and the *Beetle* hybrid board electronics. *3)*: Back view of the hybrid board with the 140-pin spring loaded connector

a detailed description of the ORFEUS-SPAS missions is provided in Krämer et al. (1990). The CSA needs a sophisticated approach for the amplification and analysis of charge signals and is used in the current MCP detector.

The parts presented in the previous sections can then be installed, fixed and electrically contacted in the detector housing, a body consisting of ceramic and kovar rings (see Sect. 1.2.4).

Additionally a getter film as discussed in Sect. 1.2.5 could be installed inside of the detector to further increase its lifetime.

1.2.1 Detector window

The current version of the IAAT UV detector has a closed design (Sect. 2.2.1). The entrance window is needed as most components inside of the detector require a high vacuum or even an ultra-high vacuum (UHV) to be maintained inside of the detector. Furthermore a photocathode can be placed on the inner surface of the window (see Chap. 2.2.1).

Transmittance and imaging errors

The disadvantage of having a window is that each window material has a certain cut-off wavelength, hence light with a shorter wavelength cannot be detected. In Fig. 1.6 the temperature-dependent cut-off wavelengths of the

most commonly used UV window materials are shown. The cut-off wavelength of Hunter and Malo (1969) should be considered a lower limit, as they did not define a certain threshold for the cut-off wavelength, but set it to the wavelength at which transmittance could just be measured. For a quicker overview, Tab. 1.1 shows the material parameters and the cut-off at 300 K as read from Fig. 1.6.

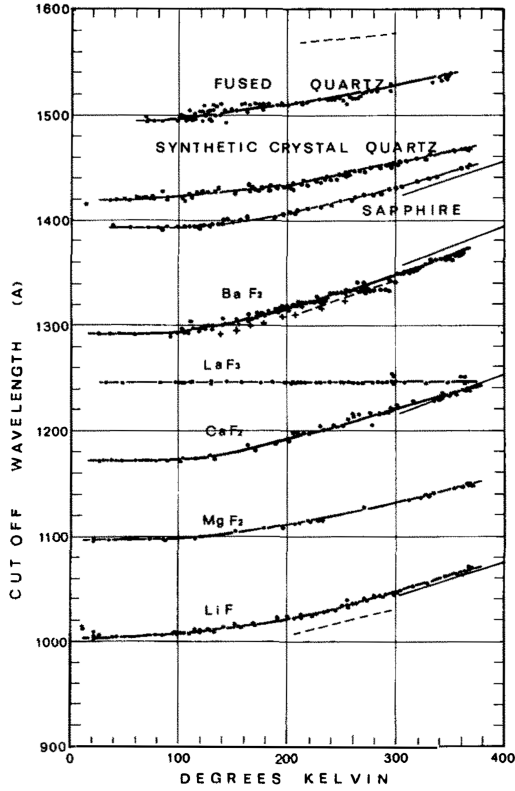


Fig. 1.6: Temperature dependent cut-off wavelength of UV window materials (Hunter and Malo, 1969)

Material	Cut-off wavelength	Thickness of sample
Syn. quartz	$\approx 1456 \text{ \AA}$	1.1 mm
Sapphire (Al_2O_3)	$\approx 1432 \text{ \AA}$	2.5 mm
CaF_2	$\approx 1221 \text{ \AA}$	1.0 mm
MgF_2	$\approx 1133 \text{ \AA}$	3.0 mm
LiF	$\approx 1047 \text{ \AA}$	3.0 mm

Tab. 1.1: Cut-off wavelengths at room temperature for UV window materials

The thickness of the window also affects its transmittance. For extinction coefficients κ_λ and thickness z , one can gain the transmittance T_λ for a given wavelength λ with help of the Beer-Lambert law $T_\lambda = \exp(-\kappa_\lambda z)$.

In Fig. 1.7, three transmittance curves for thin films of MgF_2 were plotted.

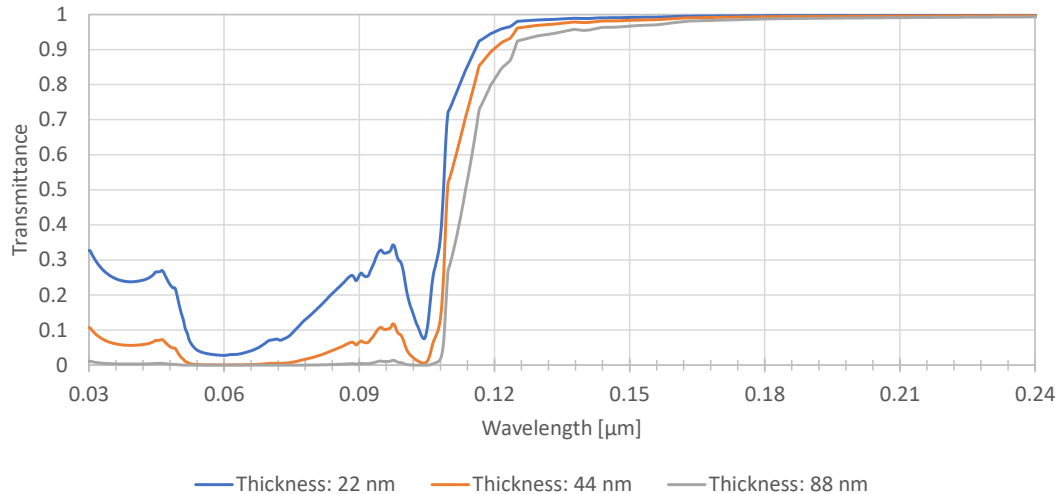


Fig. 1.7: Transmittance of a 44 nm MgF_2 thin-film with data points from (Rodríguez-de Marcos et al., 2017). The transmittance curves for 22 nm and 88 nm thin-films of MgF_2 are derived from the Beer-Lambert law

The orange line shows the measured transmittance from Rodríguez-de Marcos et al. (2017) with a measured thickness z of 44 nm. Two more curves were plotted with $z/2$ and $2z$ and the same extinction coefficients. As expected, the cut-off wavelength (transmittance below $\frac{1}{e} \approx 0.368$) does not change dramatically. It is at 109 nm for Rodríguez-de Marcos et al. (2017) measurements, 108 nm for half the thickness and 112 nm for twice the thickness.

Reflections, scattering on the surface and birefringence are further influencing factors of the entrance window for the incident light. They could lead to worse image quality or even imaging errors.

Photons that are reflected on the entrance window are lost. This is minimized to only a few percent by choosing a low-reflecting material or anti-reflection coatings like MgF_2 .

To avoid scattering, far more sophisticated measures are required. For particles which are smaller than about one tenth of the wavelength λ of the incident light, scattering is described by Rayleigh scattering. The amount of scattering is proportional to $1/\lambda^4$ and therefore strongly dependent on the wavelength. This results in high demands on the cleanliness and surface roughness for windows suitable for a sealed UV detector. To meet these requirements the entrance windows were therefore cleaned with high-performance liquid chromatography (HPLC) purified chemicals and stored in HPLC isopropanol before

installing the samples inside the UHV chamber in a clean room environment.

Birefringence is the dependency of the refractive index of a material on the direction of light propagating through a material, which can lead to imaging errors. It does occur in many UV-window materials like MgF_2 , sapphire or quartz. To minimize the influence of birefringence (001) MgF_2 windows are used, (001) defines the surface orientation with the Miller indices (see Kittel (2013, Chapt. 1)).

Important window parameters for photocathode growth

If a photocathode is placed on the entrance window, further material and sample properties of the window become important. The window has to be able to withstand the temperatures needed to grow the photocathode film onto it. In the case of GaN a higher temperature in the growth process leads to a higher mobility which results in a more homogeneous and uniform layer (Meyer et al., 2020a). Very dry MgF_2 is stable for temperatures up to 800°C , and therefore the samples should be stored in a vacuum chamber or a dry air environment. For the shipping of magnesium fluoride samples with an unactivated GaN layer, a suitable dry air environment packaging was used. The results in Sect. 3.3 will demonstrate that this packaging is already sufficient for test samples. For the storage of magnesium fluoride samples, these are placed in a vacuum system.

To achieve good results when growing photocathodes onto the window, such as a strong bond between photocathode and window, the properties of their surface again become important. The mismatch between the crystal lattices of the substrate and the photocathode crystal must be small. This is the case for cubic GaN, i.e. GaN with a zincblende structure on (001) MgF_2 . In Meyer et al. (2020a), a joint publication by the research group under the leadership of Schaadt at Clausthal University and our research group, we found that predominantly cubic GaN had grown on our samples as desired.

Regarding the influence of window surface roughness on GaN growth, good results can be obtained with laser polished samples. As described in the patent US5742026A (Dickinson Jr and Wheaton, 1998), this technique uses a preheated substrate to melt a small surface section with a UV laser. The most energy efficient configuration of the melt is realized when the surface tension is

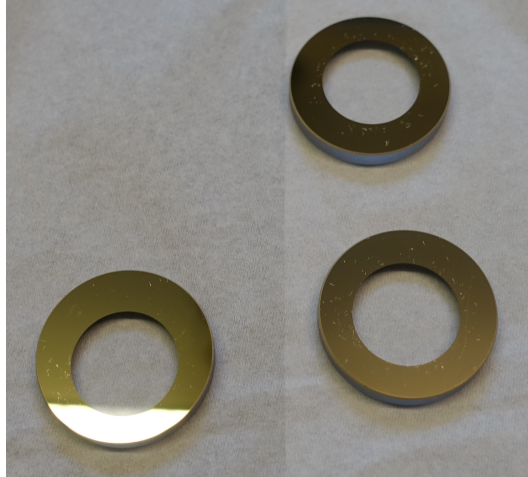


Fig. 1.8: Metallization of laser polished MgF_2 samples. Fine but loose dust is visible on the samples. Most of the dust can be blown away with dry nitrogen before continuing with the next process step

minimized, i.e., when a smooth surface is formed. A surface roughness in the range of nanometres (Vega et al., 1998) and a very short polishing time due to polishing rates of several cm^2/s (Hildebrand et al., 2011) can be met with this polishing method (on bigger samples).

Metallization

The test samples and detector windows need to have a metallization on the outer part of the samples as shown in Fig. 1.8. This metallization has two primary purposes: firstly, the conducting metal electrically connects the photocathode layer to the detector body. Sect. 1.3 describes the second purpose: for a successful sealing of the detector, the material must be wettable with the indium alloy used.

The metallization recipe used was derived from (Hermanutz, 2015, chapter 4.1.2) with slight modifications:

- Cleaning of quartz samples in an ultrasonic bath for 5 min each: dichloromethane³, isopropanol, acetone and HPLC isopropanol. MgF_2 is cleaned only in isopropanol and acetone⁴

³formerly used trichlorethylene was avoided due to stricter EU regulations

⁴Cleaning notes for MgF_2 substrates are often provided by the supplier, see for example <https://mpfpi.com/wp-content/uploads/2019/02/WS015.pdf> [18.03.2021]

- Blow off with dry nitrogen and mount into the evaporation chamber. Sample holders were employed in which four samples could be metallized at once⁵.
- Radiant heating with two tungsten boats for 20 minutes to remove water from the surface.
- Glow discharge argon plasma treatment (Hermanutz, 2011, chapter 2.5) to clean the surface. Fig. 1.9 shows the purple glowing argon plasma. Four fluorescent MgF₂ samples are attached to the sample holder with magnets.
- With the method of electron-beam physical vapour deposition pure nickel, followed by a nickel-chromium (NiCr) alloy (Ni/Cr 80/20) is evaporated. Due to the lower boiling point and as a result, a lower vapour pressure at a given temperature of nickel, Ni/Cr 50/50 is deposited on the samples. NiCr adheres very strongly to the samples and is used as a bonding agent. For the preparation of GaN photocathodes, a pure nickel film is first deposited, as this forms a good ohmic contact with GaN after an annealing step with oxygen.
- Applying of approx. 30 nm gold to this NiCr layer by thermal evaporation. How the chemically inert gold helps to optimize the sealing process is discussed in Chap. 1.3.

For samples with caesium telluride as a photocathode material, a full-surface metal layer 3–5 nm thick must be deposited beforehand. This process is very similar to the one described above but uses a different sample holder. A discussion of the poor conductivity semiconductors like Cs₂Te is found in Chap. 2.2.

The thickness must be chosen as an optimum of the resistance of the whole layer and its transmittance, as a thicker metal layer has a higher conductivity but lower transmittance.

For example, an estimate of the required sheet resistance can be obtained using the following simplified considerations: With a diode voltage of 200 V, the photocurrent can be in the order of up to 10⁻⁷ A. Thus, to allow the electrons to

⁵The sample holders were built in cooperation with the IAAT workshop



Fig. 1.9: MgF_2 samples are emitting yellow light while being cleaned with an argon plasma during the glow discharge

flow into the photocathode within one millisecond and avoid charging effects, the sheet resistance of the full-surface metal layer should not be higher than $10\text{ M}\Omega^6$.

Fig. 1.10 illustrates the strong dependence of the sheet resistance on the thickness of these thin metal layers. For example titanium has a sheet resistance in the order of $3.8 \times 10^5 \Omega$ for a film thickness of 4.5 nm and only one thousandth of that value for twice the thickness (Zhou et al., 2008, table 1). The difference in the specific resistivity of pure metals is mostly small, with gold and silver at about $2 \times 10^{-2} \Omega\text{mm}^2/\text{m}$, nickel and chrome at about four times that value and even a nickel-chrome compound with only about $1 \Omega\text{mm}^2/\text{m}$ being well in place for delivering the current needed. One can summarize that for the resistivity of a full-surface metal layer a sheet metal with a thickness of 5 nm is already sufficient. A slightly thinner layer could be used but with a standard electron-beam physical vapor deposition method, the homogeneity of the layer

⁶To avoid confusion, sheet resistance is not given in “ Ω per square”, all sheet resistances apply to sheets with an aspect ratio of 1:1.

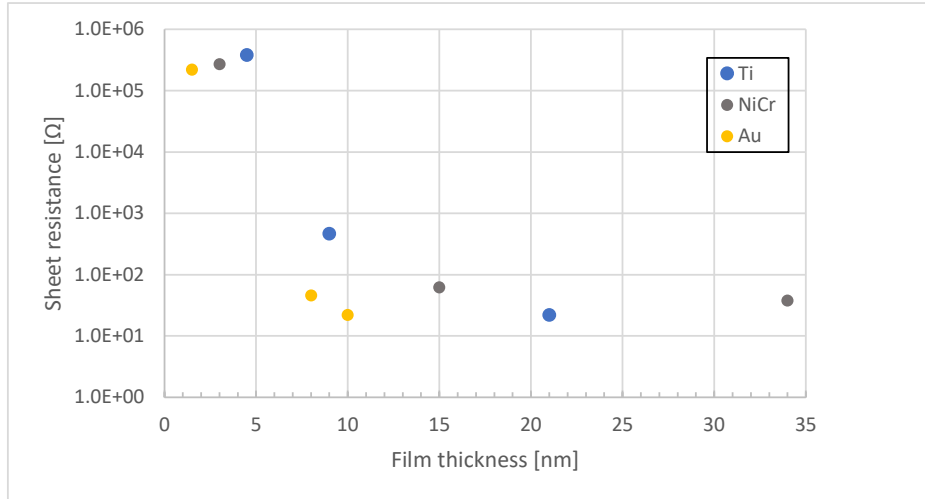


Fig. 1.10: Sheet resistance over the film thickness of titanium, nickel-chrome and gold measured with the four-probe method. Data points from Zhou et al. (2008, table 1)

would worsen rapidly due to cluster formation (Kim et al., 1994, chapt. 4.1) and some buffer should be included due to the strong thickness dependency mentioned.

The next step is to find materials that combine a high *transmittance* in the FUV with a low electrical resistivity. In the optical wavelength range indium tin oxide (ITO) is commonly used as transparent electrode material for e.g., diodes or solar cells (Fig. 1.11). Novel techniques focus on finding cheaper materials like indium free transparent oxides, often with single layer graphene as interlayers (Na et al., 2008), (Han et al., 2012). Some progress has also been made in finding transparent multi-layered electrodes in the NUV regime, primarily for NUV light emitting diodes (LEDs), also using single layer graphene, e.g. as shown in Lin et al. (2018). The latter article is also interesting for using thin nickel layers in their multilayer system.

The use of metals would normally be an obvious choice when highly conductive films are required, which is why the following paragraph takes a closer look at the transmittance through metal. The metals whose light-matter interaction is easiest to describe are alkali metals, as they only have one loosely bound valence electron. The first theoretical description which met the observations remarkably well was made by Zener (1933). Zener considered that in alkali metals the loosely bound valence electrons were acting as a free electron

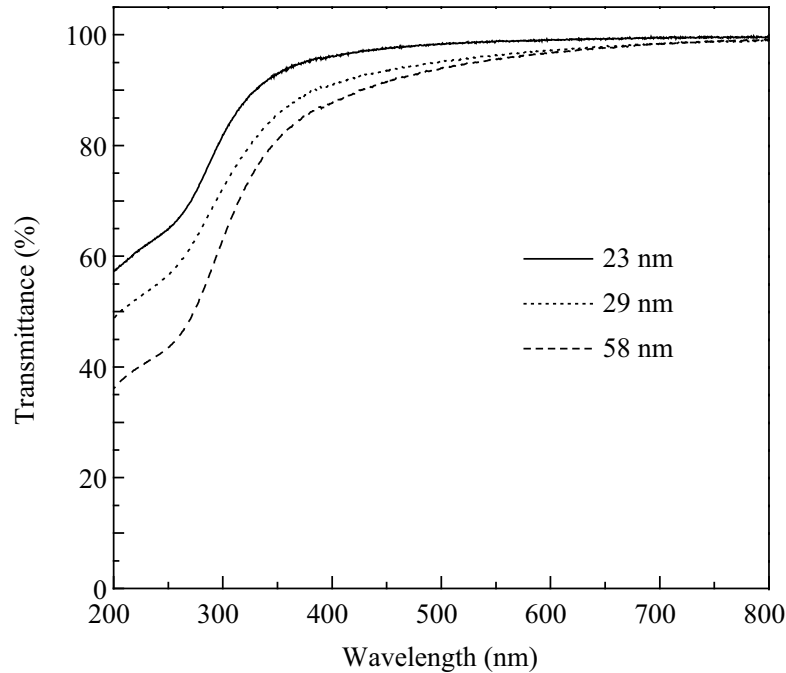


Fig. 1.11: Transmittance of ITO dropping dramatically in the UV (Jianjun et al., 2010)

gas. Incoming light will lead this electron gas to make longitudinal oscillations which are out of phase for very small wavelengths below a critical wavelength λ_c . Due to that reason metals will reflect light very effectively, leading to their shiny appearance. The only exception are alkali metals and similarly behaving metals for which light with smaller wavelength than λ_c can radiate through. A listing of such metals and their critical wavelengths can be found in Hunter (1964). The largest critical wavelength is found for magnesium at 1198 Å being almost at the cut-off wavelength of MgF_2 , making it not feasible for our detector.

The only possibility left to get transmittance through a conductive film over the whole FUV range is to use very thin layers of metal. As already mentioned, cluster formation is the main problem which must be avoided when depositing these films. It was found that gold needs to have a thickness of at least 18 nm until a uniform film is formed, for chrome this value is at only 2 nm (Kim et al., 1994). In addition, there are the requirements for the electrical conductivity of the metal layers, which theoretically (assuming a uniform layer) require a thickness of about 5 nm. Fig. 1.12 shows the resulting transmittance curves,

which are acceptable even in the critical range below 200 nm.

Combining all these results not many materials remain as good candidates. Gold and silver do have a high conductivity but will not form continuous films below 18 nm. Furthermore, silver and many other metals oxidise quickly in air, which makes them not suitable for our purposes. Ni and Cr remain as the only options and were used for the metallization of substrates for CsTe-photocathodes. To get the transmittance above 0.5 the layer thickness must be smaller than 5 nm.

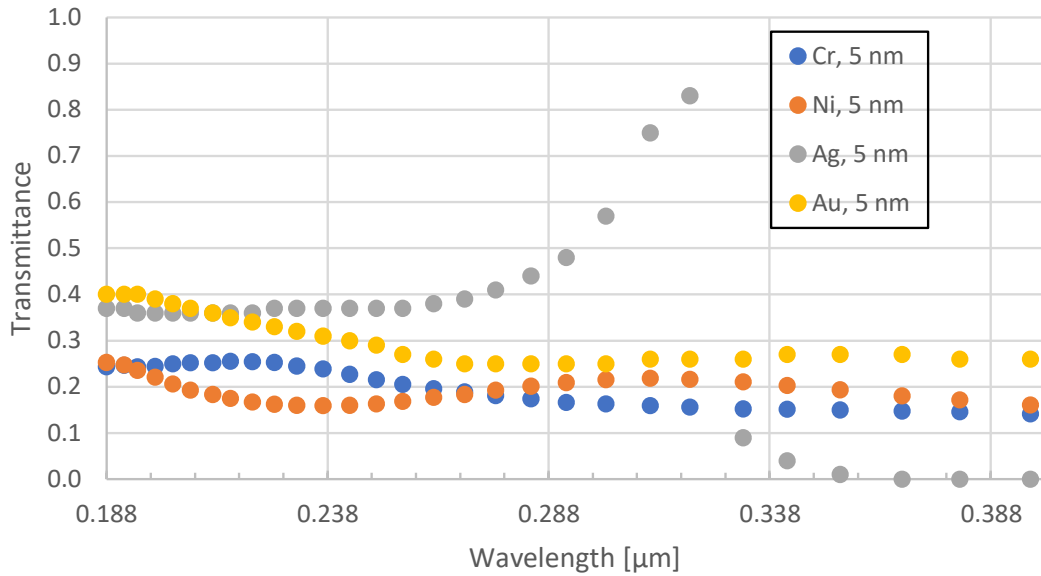


Fig. 1.12: Transmittance of a 5 nm thick layer of silver, gold, nickel and chrome at room temperature including reflections (normal incidence). Refractive index and extinction coefficients are taken from Johnson and Christy (1972) and Johnson and Christy (1974), calculations of the resulting transmittance were expedited using the optical transmittance calculator on `RefractiveIndex.info`. The Beer-Lambert law gives the transmittance at a given layer thickness, this value is then multiplied with the Fresnel reflection $1-R$ for incident light with $R_i(\lambda) = (1 - N_i(\lambda))^2 / (1 + N_i(\lambda))^2$, where $N_i(\lambda)$ is the wavelength dependent complex refractive index of the metal with $i = \{\text{Ni, Cr, Au, Ag}\}$

Using thin strips of metal as commonly used for solar cells is not an option for our imaging detector, as it would induce dark stripes. However, this could be considered an improvement for a future, larger MCP detector with multiple

photocathode materials or imaging areas.

Another possibility would be to apply metallic nanowires with a line width of less than 100 nm and a lattice constant that is much smaller than our pixel size. Such grids are commonly used as “plasmonic nanostructures” to enhance the absorption of thin organic films in the visible range (Gollmer et al., 2019). Photocathodes improved in this way can have a very high electron generation rate and can therefore be used as X-ray free electron lasers (Polyakov et al., 2013). This means that a photocathode with such nanowires has optimal electrical contact and can recharge very quickly. For single photon counting UV detectors, the combination of plasmonics and suitable photocathodes is addressed in the literature e.g. by Li et al. (2012) or Gogurla et al. (2014). The goal is to achieve high responsivities for their photocathodes. In order to pursue the goal of a higher quantum efficiency, the properties of the plasmonic nanostructures would have to be optimised according to the wavelength range of the current detector.

1.2.2 Micro channel plates

This section provides an overview of important parameters and properties of MCPs regarding our current detector. A more comprehensive presentation of the topic can be found in Fraser (1989, chapter 3).

An MCP is a thin plate with up to millions of pores (channels), each of which can act as an electron multiplier when a high voltage is applied between the top and bottom of the MCP (see Fig. 1.13). The average multiplication factor is called the gain and corresponds to the charge of the electron cloud measured in elementary charges leaving the MCP at its bottom. One of the main goals is to create an electron cloud that deposits enough charge on the anode to allow the charge amplifiers that read out this charge information to achieve a good signal-to-noise ratio (SNR). For our read-out electronics that means a gain factor in the order of 10^5 . In most cases it is beneficial to stack MCPs e.g. to achieve the required gain or reduce ion feedback, which is why the current detector uses an MCP stack with two MCPs in chevron configuration (Fraser, 1989, Chap. 3.3.2). To avoid moiré patterns⁷, the upper MCP should

⁷When two periodic patterns overlap and are slightly tilted against each other, such patterns are created, see https://en.wikipedia.org/wiki/Moir%C3%A9_pattern [20.07.2021]

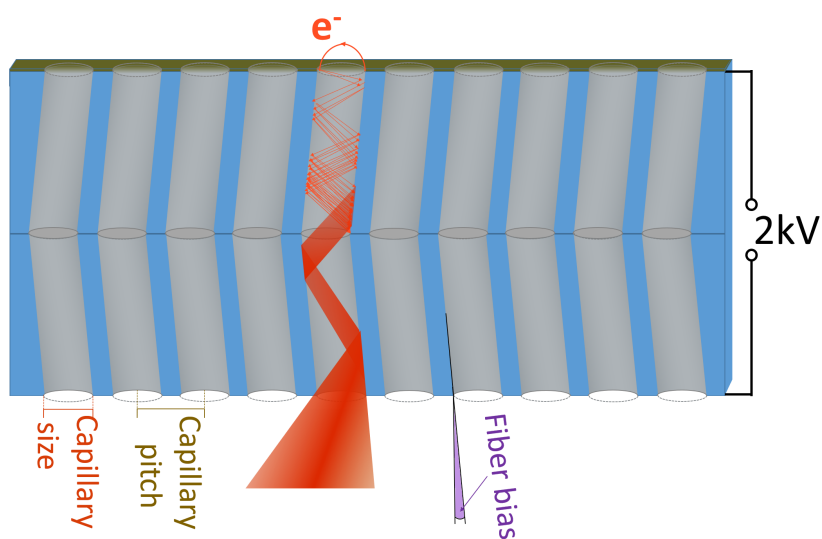


Fig. 1.13: Sketch of the multiplication of an electron into an electron cloud in a stack of two MCPs

be rotated by 30° .

When selecting suitable MCPs, there are many parameters to choose from. Tab. 1.2 shows which parameters are suitable or used in the current detector. Fig. 1.13 visualizes some of the product properties and how they are defined by the respective parameters.

Parameter	Our MCPs ⁸	Comments
Capillary size	10 μm	Must be smaller than the target pixel size of approx. 20 μm
Capillary pitch	12 μm	
Fiber bias	$(13 \pm 1)^\circ$	For bare MCPs a higher bias angle should result in a higher QE (Ertley et al., 2018)
Dimensions	50 mm diameter, 0.6 mm thickness	

Tab. 1.2: Parameters of currently used MCPs

⁸Refers to Incom ALD-MCPs that were delivered in August 2019

Conventional MCPs

The idea of a continuous dynode electron multiplier was already suggested in 1930 but it was not before the 1960s until several groups could realize the first conventional MCPs (Wiza, 1979). Fig. 1.14 outlines the manufacturing process. In short, a lead glass fibre bundle is drawn, cut, polished and etched. The wafer, which is obtained in this way, already has fine pores which now have to be made conductive. For conventional MCPs this is achieved by hydrogen annealing, whereby the lead glass is converted into lead and water, resulting in small grains of lead in the lead glass matrix. As a last step, the electrode material is evaporated onto the top and bottom of the substrate while it is rotated around its pore axis.

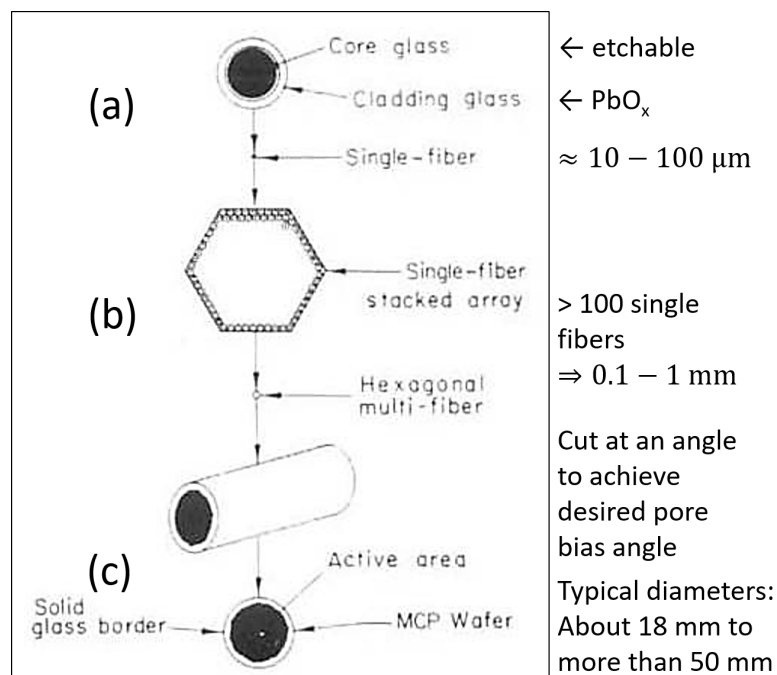


Fig. 1.14: Manufacturing steps: (a) drawing of glass fibres. Core glass is soluble in etchant, PbO_x matrix is not soluble; (b) packing of fibres to multifibre and fusing of multifibre to a boule; (c) slicing of the boule and finished MCP wafer (Wiza, 1979, Fig. 9)

The lead glass substrate, which forms the wall material of the channels of the MCP in a conventional MCP, must have both good secondary electron emission (SEE) properties and good resistance layer properties. Typically, the

resistance of the whole MCP is on the order of $100\text{ M}\Omega$ and should not be too small because the lead compounds have a negative temperature coefficient of resistance. This means that an MCP may heat up, leading to a lower resistance, resulting in a higher current, leading to a thermal runaway and failure of the MCP if no countermeasures are initiated (Wiza, 1979).

In the recent decades the product parameters of these conventional MCPs have continuously been improved: The gain modulations over the whole MCP and especially on the edges of the hexagonal multi-fibres are exceptionally low for lead glass substrate based MCPs. “Long-life MCPs” allow a higher extractable charge per area, but the “tremendously” improved lifetime atomic layer deposition (ALD) coated MCPs made them obsolete for many applications (Lehmann et al., 2017). The dark count rate has also been further reduced, but progress is limited by the fact that only the mixture of the lead substrate can be adjusted. The main driver of current improvements is the atomic layer deposition.

Atomic layer deposition

The atomic layer deposition (ALD) technology was developed for the production of display devices and for the semiconductor market to have full control of layers deposited, down to the atomic scale even for structures with high aspect ratios. Such remarkably precisely defined layers could already be produced in 1999, as one can see in Fig. 1.15, but were initially only used in the semiconductor area. An introduction to atomic layer deposition can be found in George (2010).

For MCPs the ALD process allows for choosing substrate materials other than lead glass and using material compositions for a separately tuneable resistive layer and emissive layer (see Fig. 1.16). For example it is possible to increase the temperature resistance of an MCP:

- Either by using borosilicate glass as the substrate, taking into account during annealing that the resistive layer is also stable up to the required temperature.
- Or by using more temperature resistant lead glass. Since the lead glass does not also need to have good SEE and resistance properties, the most

temperature resistant compound can be used.

Such MCPs allow the growth of a GaN photocathode on the first MCP or the activation of a getter inside the detector. Both applications require temperatures above 450°C. The following paragraphs will address the materials and layers as they are shown in the sectional view in Fig. 1.16, with regard to the properties that are important for a detector development.

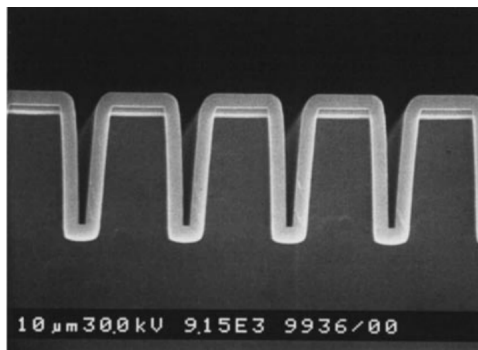


Fig. 1.15: “Perfectly conformal films” grown with ALD by Ritala et al. (1999)

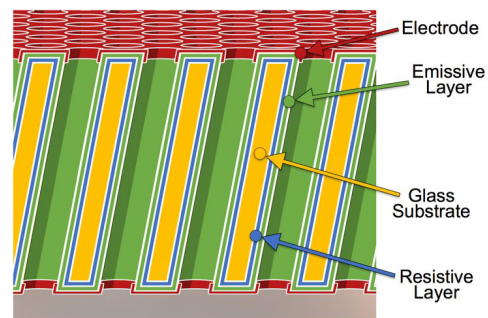


Fig. 1.16: Sectional view through an ALD-MCP (Schindhelm et al., 2017)

Substrate material

Any type of glass or material can be used as a substrate, as long as it can either be drawn into fine pores (glass capillary array, GCA) or into which fine pores can be etched.

In our ALD-GCA-MCPs borosilicate glass⁹ is used due to its material properties. These properties are a high glass transition temperature of 525°C, a maximum temperature of about 740°C until it deforms under its own weight due to reduced viscosity (Merz et al., 2003), its low coefficient of thermal expansion, and good mechanical properties that reliably withstand the vibrations during a rocket launch (Popecki et al., 2016). However, solid-border ALD-GCA-MCPs, which would be beneficial in photo-multiplier tubes (PMTs) are still in the prototype stage, and pore distortions on the boundaries of the multi-fibres (see Fig. 1.14) lead to gain modulations Cremer et al. (2020).

⁹Material specifications of C14: <https://incomusa.com/wp-content/uploads/Glass-Capillary-Array-Material-Data-Sheet.pdf> [18.03.2021]

The use of lead glass as a substrate (with ALD-coated channels) is therefore advantageous if gain modulations below 10 % are required or when the MCPs should have a solid border. The disadvantage of a higher dark count rate or smaller maximum MCP size, on the other hand, is often irrelevant for some applications.

Emissive layer

With ALD MCPs the properties of the emissive layer are independently tuneable from those of the resistive layer. The secondary electron yield (secondary electrons per primary electron) is primarily dependent on the material thickness and composition. With TiO₂ “doped” magnesium oxide the secondary electron yield can be as high as 6.9 in comparison to a factor of 3.5 for lead glass based MCPs (Jokela et al., 2012), (Popecki et al., 2016). Furthermore the properties of this layer will influence the potential lifetime of the MCP detector the most. The lifetime is characterised by the charge that can be extracted from the MCP before its gain decreases. This is because at each event, the generated SEEs cause a slight degradation of the emission layer in the channels that are involved. Consequently, the lifetime of each MCP channel depends on the total possible number of events at a given gain, i.e. number of SEEs and thus extracted charge. In an ongoing mission, the usual countermeasure to aged MCPs with a lower gain on their most illuminated sections is to increase the high voltage. Only small increments of the high voltage are necessary for a significantly increased gain as shown in Fig. 1.17 from a test report of two ordered ALD-MCPs. This countermeasure is limited because, for example, the less aged parts of the MCP will have a higher gain, which implies more problems for the detector electronics (Popecki et al., 2016).

Very detailed and long-term experiments on the lifetime of MCPs can be found in Lehmann et al. (2017) and their previous publications on that topic. For their experiment they required a significantly higher lifetime than achievable with conventional MCPs. Lead glass substrate based MCPs from PHOTONIS with “double ALD” deposited emission layers were found to have a “tremendously increased lifetime” by a factor of 50 (Lehmann et al., 2017) in comparison to uncoated MCPs.

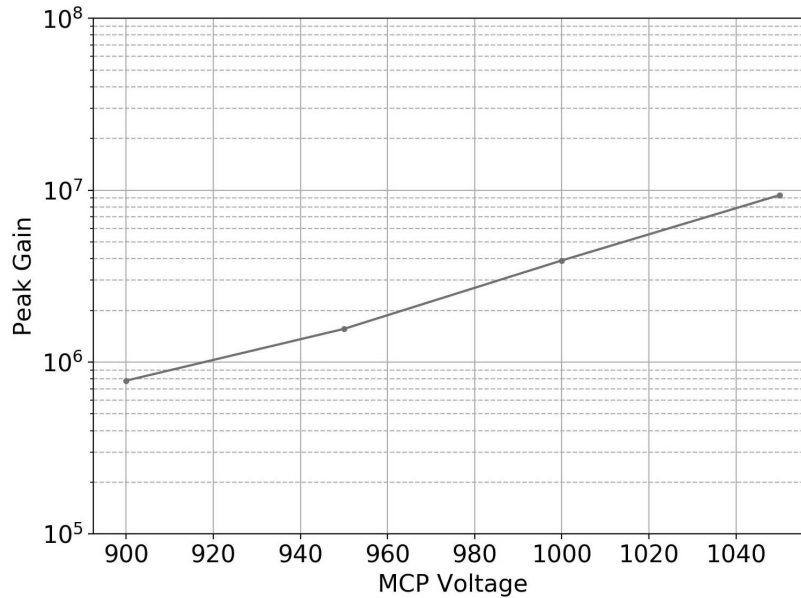


Fig. 1.17: MCP gain vs. voltage from a test report of a chevron pair of ordered Incom Inc. ALD-MCPs

Resistive layer

The resistive layer of an ALD MCP allows for a fine tuning of the currents that will recharge the channels after an event. The composition and thickness of this layer can be adjusted, so the remaining challenge is to find a recipe for which the ALD process works properly. Basically a resistive layer like aluminium oxide (Al_2O_3) and a metal layer consisting of tungsten or molybdenum is grown with alternating atomic layer deposition recipes (Elam et al., 2013). During these processes metallic nanoparticles form in a surrounding Al_2O_3 matrix, allowing for a low current flow (Mane and Elam, 2013). The temperature during this annealing process could limit the maximum temperature the MCP should be heated to, e.g. during photocathode growth or getter activation, as higher temperatures might reduce the resistivity of the resistive layer afterwards.

The MCP resistance over temperature can be described well in the form

$$R(T) = R_0 \times \exp(-\alpha(T - T_0))$$

R_0 being the resistance at a reference temperature T_0 and the temperature coefficient α defining the slope of such a curve as shown in Fig. 1.18 (Roth and Fraser, 2000). The sign and the size of the temperature coefficient α is relevant for operating an instrument mainly for two reasons.

First, it describes the power consumption of the MCPs, which changes proportionally to the inverse of the resistance $1/R$ at a constant high voltage. During a mission, it is advantageous if the temperature range in which the detector can remain in the operating mode is as large as possible, but the power consumption, which increases exponentially with the temperature, must then also be taken into account in the overall power budget.

Second, part of the energy consumed by the MCP is converted into heat, which can be dissipated at the contact points of the MCP or by emitting thermal radiation if the MCP is significantly hotter than its surroundings. An MCP with a higher power consumption will heat up accordingly until a thermal equilibrium is reached or until the high voltage limits the current flow.

The positive temperature coefficient α (i.e. negative slope of the curves in Fig. 1.18) mean, as already mentioned that a thermal runaway could occur. To prevent this, a higher total resistance of the MCP can be selected. As shown in Fraser (1989, chapter 3), however, this leads to a lower possible number of events per channel and per second, which is why a corresponding compromise must be found. In general, it could be possible to produce resistance layers with a small or even positive temperature coefficient, which would be advantageous for MCP detectors (Popecki et al., 2016).

Electrode

The electrode is a thin layer of metal, forming a full-surface contact on the top and the bottom of the MCP. For some applications the electrode can also be buried below the resistive and emissive layer, e.g., if an MgO layer is needed on top of the MCP. In combination with the resistive layer the electrode allows the channels to replenish after an event. The high voltage is applied between these two layers to operate the MCP. The properties of the electrode material become important for MCP detectors operated in opaque mode (see Sect. 2.2.1), where the upper electrode has the purpose to also electrically contact the photocathode and allow for a strong bonding between the photocathode material and electrode material. To achieve this strong bond, the mismatch in the lattice structure between the photocathode crystal and electrode material must be small.

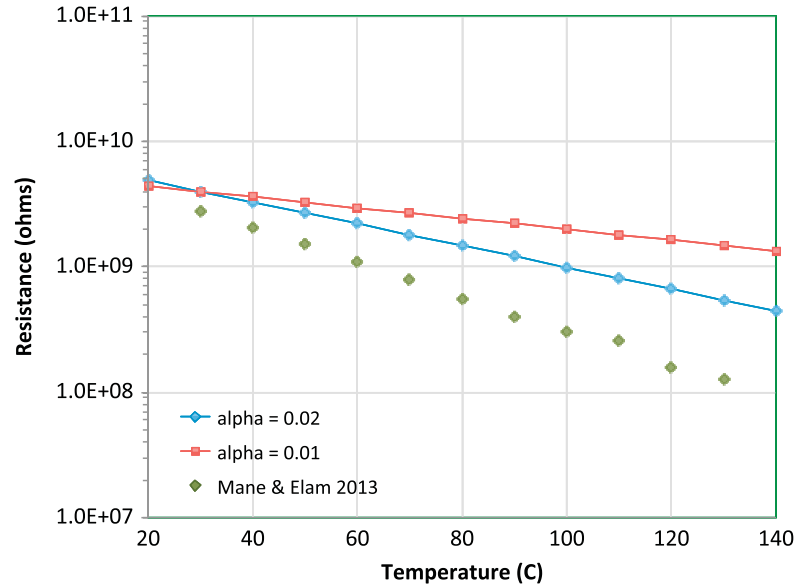


Fig. 1.18: Temperature dependent resistivity of three MCPs, green points from Mane and Elam (2013) of an ALD MCP, two uncoated lead glass MCPs with data points from Roth and Fraser (2000) (Popecki et al., 2016)

1.2.3 Anode

The electron cloud exiting the bottom side of the MCP stack has its centre of mass at the position c_m correlated to the position of the incident photon. To obtain a two-dimensional position signal encoding c_m , several anode types can be chosen from. Two types of anodes are presented in this chapter: the wedge and strip anode as it was used in the ORFEUS detector and the cross-strip anode (CSA) designs of the current MCP detector.

Wedge and strip anode

The wedge and strip anode (WSA) design only needs four (alternatively three are possible) signal paths and therefore four suitable low noise charge amplifiers to code an x and y position. The principle of the position coding is demonstrated in Fig. 1.19. The upper limit for the number of resolvable pixels is in the order of the electrons deposited on the electrode, if only the partition noise, i.e. the statistical fluctuations on the position of each electron in an electron cloud is taken into account (Martin et al., 1981). An electron cloud diameter smaller than about twice the width of a wedge and strip of the an-

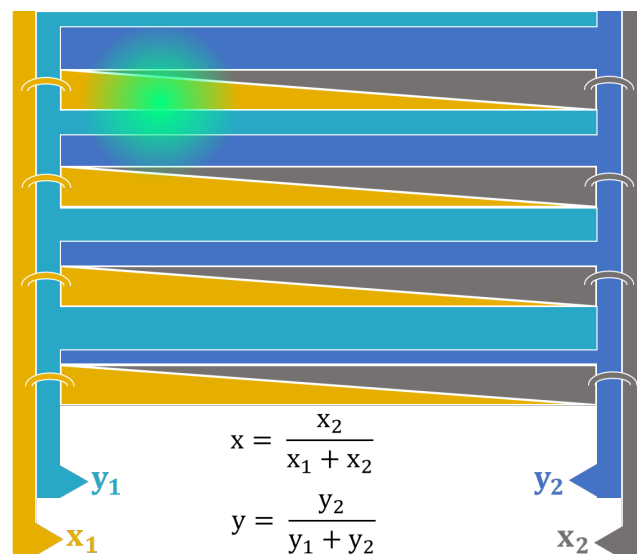


Fig. 1.19: Working principle of a WSA, not to scale or complete. White colour refers to insulating layers, a schematic electron cloud in green on the top left deposits charges on the four electrodes. From the charge values, the centre of mass is estimated by the given formula

ode leads to periodic distortions. The electron cloud size can be adjusted by varying the distance between the bottom MCP and the anode or by varying the anode potential. However, it should not be too large as the electron cloud diameter will determine the amount of distortions at the edge of the anode (Barnstedt, 2016). Improved anode designs or bigger anodes than the active area of the MCP will reduce these border distortions. Further limitations on the resolution from e.g., the equivalent noise charge of the detector electronics or a photocathode in semi-transparent mode with a certain distance to the first MCP do not depend on the anode type used.

The main disadvantage of this design is the high gain needed to achieve high resolutions, limiting the lifetime of the MCPs and thus the detector in general.

Cross-strip anode

To achieve the goal of a long lifetime of the MCPs with their limited extractable charge, most often the best solution for high count rate detectors is to lower the gain of the MCPs. In a corresponding experimental setup, Tremsin et al. (2004)

demonstrates the capabilities of the CSA design by achieving the resolution limit caused by the capillary pitch of the MCP with a gain *reduced* by a factor of 20 (compared to a WSA design). Fig. 1.20 shows how the strips are oriented and insulated against each other. The working principle of the cross-strip design is illustrated in Fig. 1.21. The strips collect charges, the charge information of parallel strips encodes the centre of charge in the x or the y direction respectively. For the current detector, we use a variation of this design in which the strips are buried inside insulating Low Temperature Cofired Ceramics (LTCC) in the x-direction and connected to charge collecting pads with vias. These vias are visible as small dots in the centre of each pad and at the end of strips as Fig. 1.22 illustrates. Since the pads are on the same plane as the strips in the y direction, this design is called a coplanar CSA. It has the advantage of being easier and more accurate to manufacture within the specifications. The area covered by the pads and the strips is equally large and is designed to cover about 61.7% of the total area of the anodes with 39 mm anode size.

Charge amplification

In our design, the charge information of each strip is measured individually with 64+64 discrete channels for the two directions. The charge evaluation has to be fast enough to account for the count rate of the detector, it needs to have a very low equivalent noise charge to achieve the resolution requirements, it must account for the strict power budget limitations of possible missions, and work under space conditions for years, i.e., needs to be radiation hardened. This makes the use of amplification chips necessary, in our case the *Beetle* chip meets our requirements and analyses the charge information for each of the 128 channels. The *Beetle* chip is radiation-resistant by design and has a very low power consumption of less than 6 mW per channel, making only radiative cooling of the chip necessary. It was developed by the Max Planck Institute for Nuclear Physics in Heidelberg, a detailed documentation of the chip is provided in Löchner (2006) and Löchner and Schmelling (2006). The *Beetle* chip has several parameters that can be set and optimised to adjust e.g. the amplification strength or pulse duration. The chip samples the charge value on each channel at a rate of 40 MHz and stores the information in a ring buffer.

In the corresponding time interval of 25 ns, the charge deposited on each of the 128 strips is thus evaluated by assigning a charge value to them. All 128 charge values in the same 25 ns time interval are called a sample. Only if a trigger event occurs, a predefined number of the stored samples is multiplexed to four outputs. Depending on the centroiding algorithm used, only three to five samples need to be evaluated by our read-out electronics to calculate the centre of mass of the electron cloud with sufficient precision. This means that the *Beetle* chip also reduces the amount of data that needs to be analysed and sent from the detector head to the ROE. As the current bottleneck of the detector limiting the count rate is caused by the analogue to digital converters, the reduced amount of data is crucial to achieve the goal of evaluating 300,000 events per second.

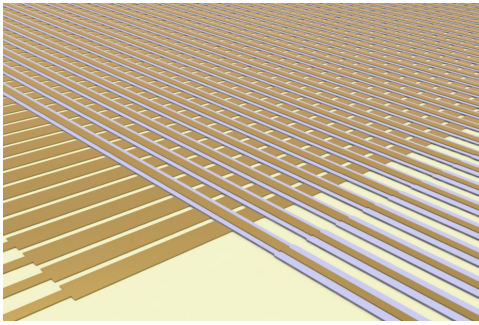


Fig. 1.20: Render of crossing strips (golden) with insulating layers (white) (Diebold et al., 2013)

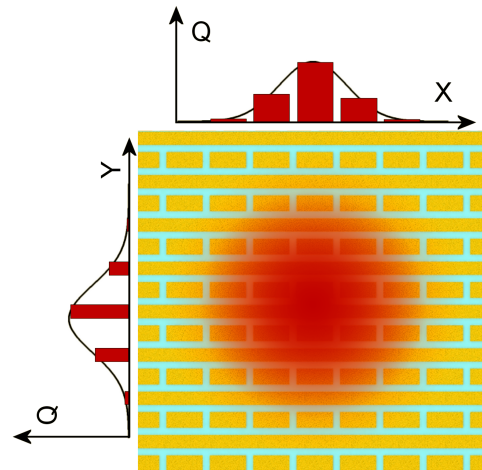


Fig. 1.21: Principle of the coplanar CSA

High temperature cofired ceramics (HTCC) could be used for a possible improvement of the coplanar CSA design. This would leave the performance of the anode unchanged, but the hard soldering process of the detector body would benefit from higher temperatures without outgassing (see Chap. 1.2.4).

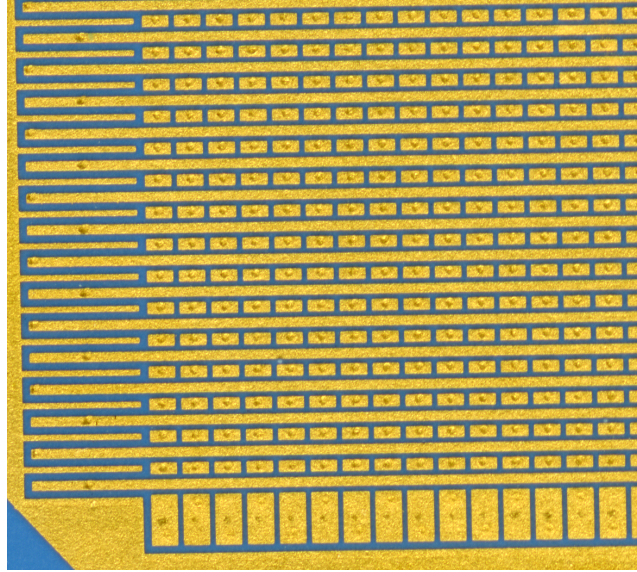


Fig. 1.22: Section of a high resolution image of an CSA. Blue coloured areas are the insulating LTCC, golden areas the contact pads. In such an image e.g. irregularities in the thickness of the insulation would be visible

1.2.4 Ceramics and Kovar body

The body of the detector consists of conducting Kovar rings¹⁰, ceramic rings and the anode on its bottom (see Fig. 1.23). The ceramic rings are needed as insulation layer between the Kovar electrodes that are themselves connected to the HV supply via connecting tabs.

Kovar is a metal alloy that mainly consists of iron, nickel and cobalt in a composition to match the thermal expansion coefficient of most ceramics ($\approx 6 \times 10^{-6}$ K). Combining materials with similar thermal expansion coefficient avoids mechanical stress that would otherwise occur when the temperature changes, first and foremost during the assembly, but also during a mission and ground testing.

These rings and the LTCC anode are joined via hard soldering, with a tolerance in height of only about $100 \mu\text{m}$ and tested if helium tight¹¹. The topmost ring contains a recess area into which an indium alloy ring can be

¹⁰The Kovar rings are produced in the IAAT workshop within the demanding specifications.

¹¹The external supplier is Hans Rudolf Elsener at the *Eidgenössische Materialprüfungs- und Forschungsanstalt* (Empa), Switzerland

placed during the detector sealing process (see Sect. 1.3). This ring is coated with thin adhesion layers, which ensure strong adhesion between the Kovar ring and the indium sealant. These measures made it possible to produce a helium tight sealed detector.



Fig. 1.23: *Left:* Render of the CAD model of the ceramics and Kovar body with the anode at the bottom. Three connecting tabs can be used to attach the corresponding power supply cable plugs. *Right:* Photograph of the assembled diode body. When compared to the render, it looks very similar as planned with the CAD model with only changes to the electrodes. Photograph kindly provided by Hans Rudolf Elsener, Empa.

1.2.5 Getter and getter activation

After the sealing of the detector body, a getter could reduce or at least maintain the partial pressure of mainly H_2 (Stout and Gibbons, 1955), extending the lifetime of the photocathode and the detector in general. More residual gas leads to increased ion feedback, e.g., positively charged ions are accelerated towards the photocathode, changing the material composition of the photocathode and even physically damaging it due to their potentially high momentum.

A potentially suitable getter type consists only of thin rectangular strips of getter material with side lengths of a few millimetres to centimetres. Thus, even several getter foils could fit into the detector body. A passivation layer on top of the getter prevents the absorption of gas before this is desired. For activation the getter must be heated to a temperature of about 450°C for several minutes. For example, in the case of SAES ST122¹² getters, lower activation

¹²SAES Getters S.p.A., ST122 SP Getter Brochure: <https://psec.uchicago.edu/getters/ST%20122%20Brochure.pdf> [18.03.2021]

temperatures can be compensated by a longer activation process. However, a reduction in temperature by only 100 K prolongs the activation from minutes to several hours and results in a lower total sorption mass of the getter. In order to be able to heat the detector to such high temperatures without damaging its MCPs, ALD-coated MCPs with temperature-resistant substrate and resistive layer can be used (see Chap. 1.2.2).

1.3 Tube sealing

For the closed design of the detector, it must be sealed and an ultra-high vacuum must be maintained inside under all conditions. This includes conditions that may occur during the assembly, integration, verification, and especially during scientific operation. To seal the detector, the hot (above approx. 150°C) detector window is placed onto the similarly hot detector body. A molten eutectic bismuth-indium alloy wets the sealing surfaces (see Sect. 1.3.1) and acts as a sealant after the cooling of the detector body with window. In the following section, the wetting of surfaces in general and the measures taken in collaboration with our cooperation partners at Empa are discussed. The successful sealing tests and measurements with the sealed diode bodies are presented in Chap. 3.2.

1.3.1 Wetting of materials

In this section the procedures taking place during the sealing process are described. A more general overview on the wetting of surfaces can be found in Yuan and Lee (2013). The test setup is as follows: An indium alloy (Bi-In) ring is placed inside of the diode bodies sealing ring. The sealing surface must be horizontal so that the gravitational force is perpendicular to the sealing surface. There are three different interfaces between the liquid Bi-In alloy, the sealing area and the vacuum of the detector UHV chamber, the most important interface being the Bi-In to the sealing area. Young's equation (see (Young, 1805, Section VII)) describes how the interface tensions γ_{lv} between liquid and vacuum, γ_{sv} between surface and vacuum and γ_{sl} between surface and liquid

will lead to droplets as shown in Fig. 1.24 with a contact angle θ

$$\cos \theta = \frac{\gamma_{sv} - \gamma_{sl}}{\gamma_{lv}} \quad (1.1)$$

which is the optimal energetic configuration of this droplet for these interfaces.

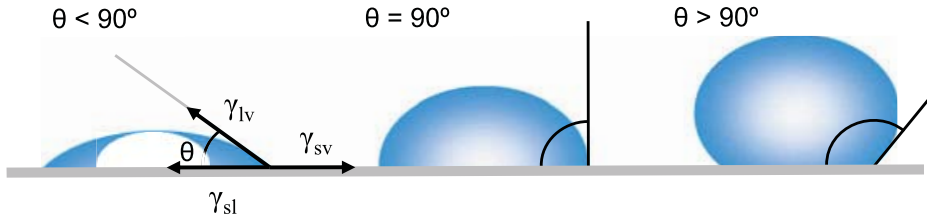


Fig. 1.24: Definition of the contact angle between a solid surface and a droplet. A small angle θ refers to a good wetting of the surface due to a low surface tension (Yuan and Lee, 2013, Fig. 1.1)

Young's equation is a good first order approximation but will only describe static processes with homogeneous surfaces well, i.e., if the amount of liquid changes, the liquid moves along the area, or for surfaces with high surface roughness the contact angle might deviate largely from θ . In our case for a slowly advancing liquid which would ideally wet more and more of the sealing area, Young's equation is a good enough approximation for finding suitable material combinations. The surface roughness of the sealing area should be as small as possible for comparable results (Yuan and Lee, 2013).

To find suitable material combinations with very small contact angles, a drop shape analyser (DSA) can be used. Inside of the DSA a homogeneous metal layer and a small cylinder of our sealing material is placed and heated under controlled atmospheric conditions (e.g., high vacuum). A camera system will record the silhouette of the droplet. To achieve high consistency a software solution for determining the contact angle over time and temperature should be used.

Fig. 1.25 makes clear that the indium alloy used for the sealing process will not wet a Kovar surface. A contact angle of less than 90° , the smaller the better, is mandatory to achieve a full surface wetting, but a contact angle of 140° was measured for Bi-In on Kovar by our project partners at Empa.

In contrast to that Fig. 1.26 shows that for Ag_{28}Cu and gold a good wetting is expected. As a result our diode bodies are coated with the silver-copper alloy,

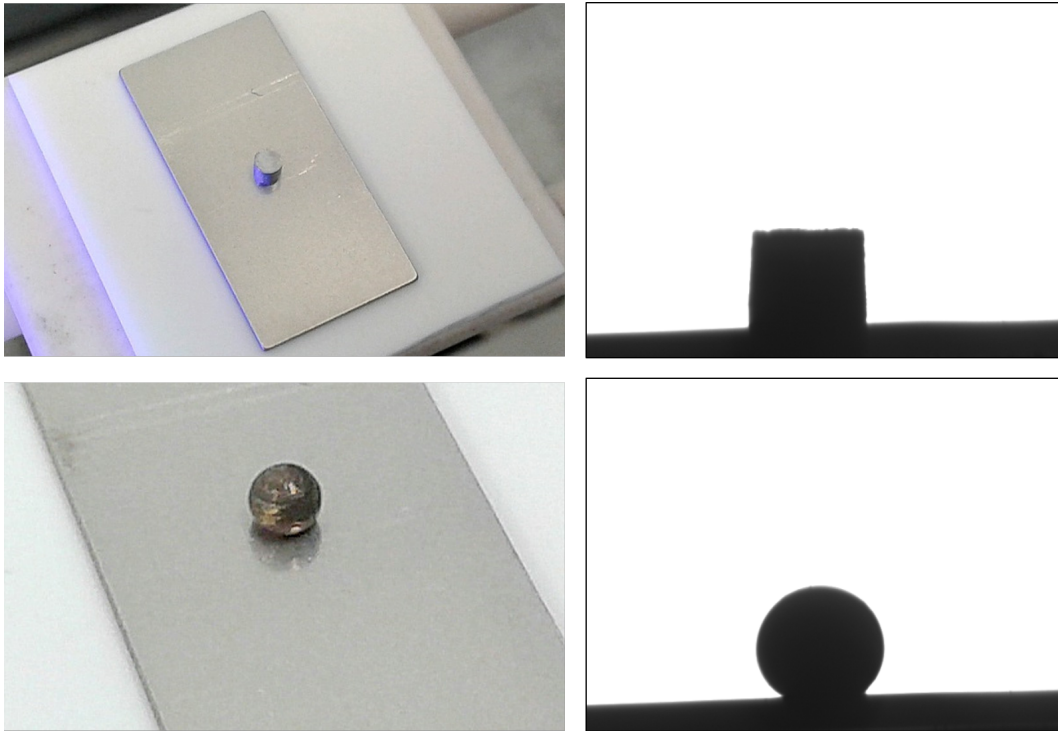


Fig. 1.25: *Top left:* Solid In-Bi cylinder on a Kovar plate at the start of the experiment. *Top right:* Picture captured with the DSA camera system showing the silhouette of the solid In-Bi cylinder. *Bottom left:* Picture of a molten In-Bi droplet on Kovar. *Bottom right:* Picture of the DSA camera system of the molten droplet. The contact angle between molten In-Bi and Kovar is very large with about 140° .

Measurements by Dr. Elsener, Empa, used with kind permission

the metallization of the detector window and test samples uses NiCr as bonding layer between the topmost gold layer and the quartz or MgF_2 samples.

In Chap. 3.2 the experimental results of the wetting and the sealing process are shown.

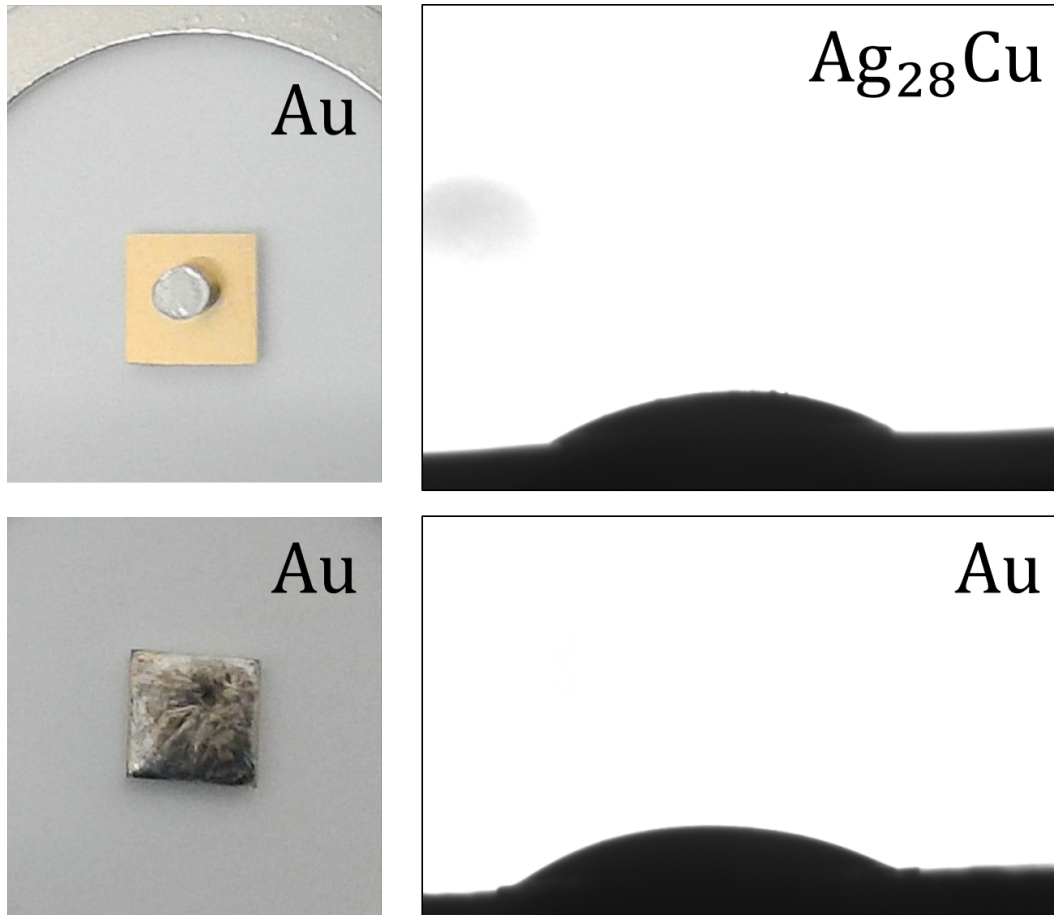


Fig. 1.26: *Top left:* In-Bi cylinder on a quadratic gold layer (5 mm side length, 2 μ m thickness, subjacent NiCr and TiW layers as bonding agent and diffusion barrier) at the start of the experiment. *Top right:* silhouette of molten In-Bi alloy on a Ag₂₈Cu field, contact angle about 45°. *Bottom left:* molten In-Bi alloy covers whole gold surface. *Bottom right:* DSA camera image of molten In-Bi on gold, contact angle about 40°. *Measurements by Dr. Elsener, Empa, used with kind permission*

Chapter 2

Photocathodes

The following chapter introduces the most important parameters of photocathode crystals, with the goal to understand processes in photocathodes with negative electron affinity (NEA). Introducing the band structure of crystals in Sect. 2.1.1 will help to understand how solar blindness without the need for filters is achieved in photocathodes (see Sect. 2.1.2). The band structure of a given crystal can be influenced to achieve the NEA e.g. by p-doping the crystal and surface activation with Cs.

To describe the process of photoemission, the three-step model by Spicer (1958) is presented in detail in Sect. 2.1.3. In short, the three steps are:

1. The absorption of photons and excitation of electrons to the conduction band.
2. These electrons move in the conduction band of the photocathode crystal and reach the surface region.
3. With a certain possibility they can tunnel into the vacuum and lead to the emission of these electrons.

The optimization of the QE of the photocathode can therefore be achieved by optimizing the corresponding parameters of each individual of these processes. Often a compromise must be found, e.g. p-doping of the photocathode crystal lowers the effective electron affinity and therefore escape probability but introduces scattering centres, such that the diffusion length for electrons in the conduction band gets worse. An optimal parameter set must also take into account which mode the photocathode is operated in. In the semi-transparent

mode the photocathode is grown on the UV window of the detector, incident light is absorbed by the thin photocathode layer to a certain degree and photoelectrons leave the photocathode into the sealed detector. In the opaque mode the photocathode is grown onto the first MCP, which allows for thicker photocathodes and therefore potentially higher absorption (for details see Sect. 2.2.1).

The QE of a photocathode is dependent on the energy of the incident photons. The low energy cut-off of photocathodes can be influenced by using slightly different material compositions. In the case of GaN, the cut-off can be fine-tuned to higher energies by including aluminium or to lower energies by including a certain amount of indium. In opaque mode, photocathodes can have a drop in QE at high energies due to surface recombination, this is discussed in more detail in Sect. 2.2.2.

If optimizing for the absolute QE of the photocathode its reflectivity is important. This property is often not included when obtaining an internal QE of the photocathode and is less popular in literature as it is difficult to influence the reflectivity for a given material transition. But by growing nano-rods of photocathode materials, the effective reflectivity of the vacuum-photocathode transition is greatly reduced for all incident angles (see Sect. 2.2.3).

Another way to enhance the performance of the photocathode is to include internal and external electric fields. Gradient or exponential doping will lead to internal electric fields that accelerate electrons towards the surface of the photocathode. Faster electrons have a higher probability to tunnel through small surface barriers into the vacuum, therefore the QE of such a device would be improved. An external electric field has this effect as well and can be achieved by applying a voltage between the photocathode and the electrode of the first MCP. Such fields will also have an influence on the resolution of the whole detector and its dark current (see Sect. 2.2.4).

The low dark current and excellent noise characteristics are one of the main advantages of NEA photocathodes, as it makes them ideal for the detection of low light level signals without the need of actively cooling the detector.

For space applications the longevity of the photocathode is another important parameter. In the case of GaN in sealed tubes, excellent stability could be measured (see Sect. 2.2.5). The influence of radiation is relatively low on

GaN as it has a high binding energy and for these thin photocathode layers the cross section is relatively small, potentially allowing for a lifetime in the order of at least years.

The corresponding experimental results and their discussion are provided in Chap. 3.

2.1 Photocathode theory

The goal of this section is to acquire the theoretical background needed to describe certain properties of the photocathode material, focussing on the properties that are important for the performance of the detector. The first step is to derive a model that describes allowed energy states of electrons in a crystal and their properties in such a structure, the so called band structure. A complete view on this topic is presented in Kittel (2013, chap. 7). This will allow us to understand the absorption of photons in photocathodes and how they are able to leave the photocathode material.

2.1.1 Band structure of crystals

When growing photocathodes, the conditions during growth e.g. temperature or partial pressures, allow the atoms of the photocathode material to assemble into an ordered structure: a crystal. Such a crystal and its corresponding crystal lattice can be described using only a minimal ordered group of atoms, the so called primitive cell and a certain translation symmetry. The properties of a crystal, like its structure, crystal planes or the distance between atoms, can be obtained by X-ray scattering (Friedrich et al., 1913), (Bragg and Bragg, 1913). In order to describe the scattering on the crystal structure, the Fourier transform of the crystal lattice, with the lattice constant \vec{a} , becomes important. The Fourier transformed lattice is again a lattice, but has a “reciprocal” lattice vector of $\vec{G} = 2\pi/\vec{a}$.

It is common to describe the crystal lattices, e.g., the cleavage surface of a crystal, also in reciprocal space with the Miller indices (see Fig. 2.1).

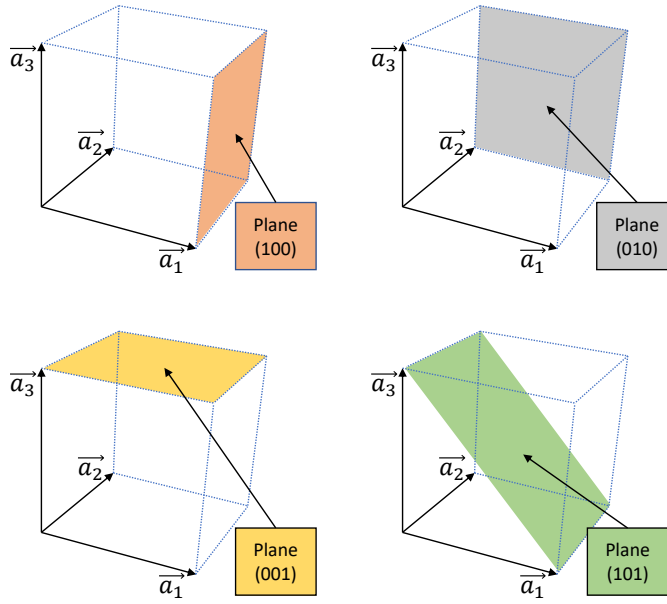


Fig. 2.1: Examples for planes described by the Miller indices. For the construction of the Miller indices (h, k, l) with h, k and l being integers see Kittel (2013, chap. 1). If a plane defined by Miller indices has no intersection with an axis, the corresponding Miller index is zero

Next we want to understand why a band structure with “allowed” energy levels at a given wave vector \vec{k} of the electrons and a certain band gap are found in crystals. For this purpose we have to calculate a wave function of the electrons, as the probability of measuring them with a certain wave vector \vec{k} at a certain position \vec{r} is given by the squared modulus of the wave function $|\Psi_{\vec{k}}(\vec{r})|^2$ (Born, 1926).

The periodically overlapping energy levels of the atoms in a crystal influence each other. The solutions of Schrödinger’s equation for a potential with the periodicities \vec{R} are called Bloch waves, i.e. $V(\vec{r}) = V(\vec{r} + \vec{R})$, with \vec{r} a position and \vec{R} a vector in one of the directions of the crystal’s symmetry (Bloch, 1929). Bloch proved that in this case the probability amplitude of the solution will also have the same periodicity, i.e. $\Psi_{\vec{k}}(\vec{r}) = v'(\vec{r}) \exp(i\vec{k}\vec{r})$ with $v'(\vec{r}) = v'(\vec{r} + \vec{R})$. Furthermore each solution defines a certain energy eigenstate $E(\vec{k})$.

The secondary boundary condition for electrons in such a crystal is given by Bragg’s law, which describes the scattering in the crystal (Bragg and Bragg, 1913). For electrons with wave vectors $|\vec{k}| \approx |\vec{G}|/2$, scattering becomes important as their wavelength is $\lambda \approx 2\pi/|\vec{k}|$ and constructive interference occurs. These points where the constructive interference is strongest are on the edges of the Brillouin-zones (see Fig. 2.3). With these boundary conditions, two solutions can be found for the wave functions describing the electrons in the potential of the crystal (Kittel, 2013, chap. 7):

1. A solution $\Psi(+)$ with electrons being likely to be found at the core

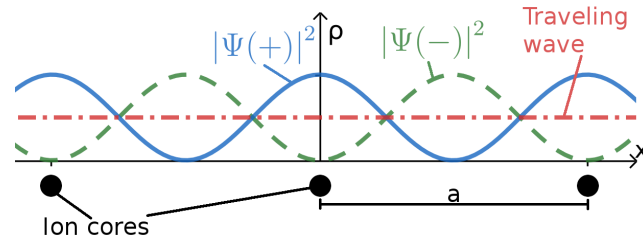


Fig. 2.2: Probability densities of electrons in a crystal

potentials (see Fig. 2.2). This means that these electrons are near the attractive core potential, are bound and their potential energy is lower compared to the case of evenly distributed electrons without a potential.

2. A wave function $\Psi(-)$ as solution for electrons that are more likely to be found between the core potentials. The probability function for this solution is plotted as the green dotted line in Fig. 2.2. The average potential energy of the electrons is higher compared to the first case.

These two solutions define two energy levels of the electrons in the crystal with a “forbidden zone” between them where the probability density of both solutions $|\Psi(+/-)|^2 \approx 0$. The difference in the average potential energy of the electrons of these energy levels is the so called *band gap*. For metals it is about zero, which leads to electrons that can move through the metal and can be described as a free-electron gas. When an external voltage is applied, they are accelerated and acquire an average drift velocity opposing the direction of the corresponding electric field vector. For this reason, electrons with these energy levels referred to as being in the *conduction band*. Electrons that are described by the $\Psi(+)$ solution are bound to a core potential and cannot move through the crystal, the highest “allowed” energy state of this solution is called the *valence band*.

In contrast, semiconductors have a small band gap. At temperatures above absolute zero, there is a small probability for each electron to be excited into the conduction band. E.g. undoped silicon has a band gap of about 1.1 eV and a small specific electrical conductivity at room temperature of about $5 \times 10^{-4} \text{ 1}/\Omega$.

If an electron only has to absorb a photon to get excited into the conduction band, this is called a direct band gap. Indirect band gaps are transitions where

also the (quasi-)momentum $\hbar\vec{k}$ of the electron has to change. As always, transitions can only occur if the new state is “allowed”, i.e. is an energy eigenstate $E(\vec{k})$ of a solution. The Brillouin zones provide possible k-values in each of the crystals directions. For clarification see the abscissa of Fig. 2.3.

The band structure of a crystal can be obtained experimentally or can be computed. Experimentally, for example, the absorption length of photons with different energies could be measured. In Fig. 2.3 observations and computations were combined to obtain the band structure: the energy eigenstates of a wave function with a relatively easy to compute pseudo potential was used and compared with the observations. If the numerically obtained solutions match the observation points well enough, the pseudo potential was a good approximation for describing the crystal structure. Moreover, for a given material composition, there may be several possible crystal structures that differ only in the arrangement of the atoms. For example, in GaN, the gallium and nitrogen atoms can arrange in two different crystallographic structures. The hexagonal wurtzite crystal structure is called α -GaN, if the atoms order in a cubic zincblende structure it is called β -GaN. Each configuration has its own band structure and corresponding band gap (Meyer et al., 2020b). As discussed in the following sections, the mismatch between atoms of the substrate and the photocathode crystal should be as small as possible. This is achieved for (001) MgF_2 substrates with a mismatch of only a few percent to cubic β -GaN.

2.1.2 Band gap, solar-blindness and conductivity

An optimal UV photocathode should be solar-blind but also have a certain conductivity. To achieve the solar-blindness the detector should not be sensitive for wavelengths longer than $\lambda_{limit} \approx 300$ nm. The energy of an absorbed photon $E = \frac{h \times c}{\lambda_{limit}}$, with h the Planck constant and c the speed of light, can only be used to excite an electron, if it is larger than the band gap of the semiconductor. Thus, to achieve solar-blindness, the band gap should be larger than 4.1 eV for a lower cut-off at 300 nm, or at least 3.1 eV to get a cut-off at about 400 nm.

On the other hand a large band gap will lead to a low conductivity of the semiconductor at room temperature. When operating the detector, photoelectrons leave the photocathode material. If the conductivity of the photocathode is too low to replenish, it charges up positively. This, in turn, lowers the internal

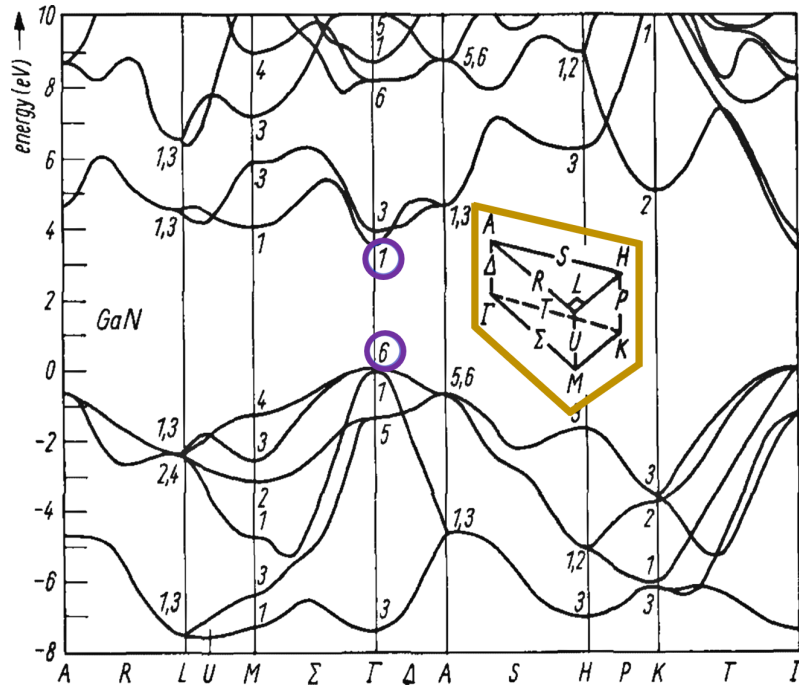


Fig. 2.3: Band structure of hexagonal GaN. The illustration in the yellow box shows the points and distances of the first Brillouin zone. Therefore, the corresponding values on the abscissa represent possible k distances of electrons. The value Γ in about the centre refers to $\vec{k} = 0$. Note the two points Γ_6 and Γ_1 , encircled in purple, define the direct band gap with $\Gamma_1 - \Gamma_6 = 3.6$ eV (Bloom et al., 1974)

or external electric fields required for the electrons to leave the photocathode with high likelihood. There are two potential countermeasures: conductive metal layers (see Chap. 1.2.1) or manipulating the band structure of the semiconductor to increase its intrinsic conductivity.

2.1.3 Manipulating the band structure and three-step model

With the band structure the absorption of UV photons and excitation to the conduction band can be explained. In the conduction band the excited electrons can move freely and are able to get near the surface of the photocathode. To make the photocathode work as intended, these electrons must now be able to leave the photocathode material. They should not depend on further

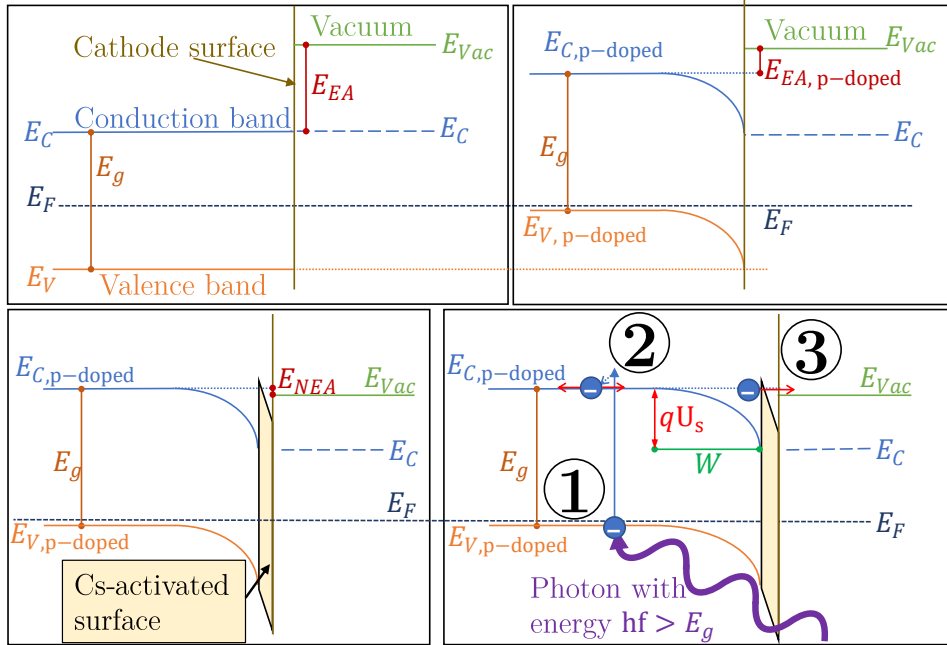


Fig. 2.4: *Top left:* Schematics of an undoped and unactivated semi-conductive photocathode. The Fermi level is located at the centre of the band gap $E_g = E_C - E_V$. The electron affinity E_{EA} is very high. *Top right:* Band structure of a p-doped photocathode. Too high doping can shorten the diffusion length of electrons in the conduction band, optimally the Fermi level is just above the valence band edge. Near the cathode surface is the band bending region (BBR) with width W and depth $q \times U_s$, U_s is the surface potential with respect to the bulk (Ng, 2002, Chap. 64.3). *Bottom left:* Cs-activated surface leads to another bent band, electrons from the conduction band in the bulk of the photocathode, effectively experience a negative electron affinity (NEA). *Bottom right:* The three-step model of photoexcitation in the case of a NEA photocathode by Spicer (1958): **1.**: A photon with an energy bigger than the band-gap of the photocathode excites an electron to the conduction band. **2.**: The electron diffuses through the photocathode crystal in the conduction band. In NEA photocathodes, electric fields accelerate the electrons towards the surface. **3.**: Due to bent bands, electrons experience further acceleration in the vicinity of the activation layer and vacuum. If their energy is high enough, electrons have a high tunnel probability through thin areas with band energies above the conduction band. The electron leaves the NEA photocathode

photoexcitation, since it is very unlikely that a photon will hit them, because there are many more electrons in the valence band than excited electrons in the conduction band.

There are a few different ways to increase the probability of releasing electrons from the photocathode into the vacuum. High temperatures (thermal electron emission, Nobel prize 1928 for O.W. Richardson) are not feasible for photocathodes in space applications for photon detection as the dark current and power consumption of such a device would be too high. The effect of high electron energies due to strong electric fields or photon energies much higher than the band gap of the photocathode material are discussed in 2.2.4, both lead to a small amount of dark current/noise. To achieve the goal of as little noise as possible in combination with high escape probabilities for the electrons and therefore high QE, the most effective way is to achieve a very low or (effectively) negative electron affinity (NEA) E_{EA} . It is defined by the difference in energy between the vacuum energy E_{vac} and the bottom of the conduction band E_C . For illustration see Fig. 2.4. Note that for each material transition the electron affinity is positive, only because of the BBR it is in sum negative.

Such band bending is achieved by doping semiconductors, requiring p-doping to lift the valence and conduction bands up relative to the Fermi energy. A detailed analysis of band bending can be found in Wu and Kahn (1999). The depth qU_s and the width W of the bent conduction (and valence) band are the most important properties, both quantities are defined in Fig. 2.4. The BBR helps to achieve the effective NEA, as electrons are accelerated towards the potential minimum. These accelerated electrons have in turn a higher probability to tunnel through remaining surface barriers (see the bottom right of Fig. 2.4). Increased doping leads to stronger bent bands, i.e. larger depletion depth W . The resulting higher internal electric fields lead to a higher escape probability, but the diffusion length is shortened and thus electron transport losses increase. Furthermore if qU_s and W are too large, the accelerated electrons could become “hot” and have a much smaller free path than the already shortened diffusion length L , i.e. they lose their gained momentum due to scattering and are “trapped” in the BBR (see also Sect. 2.2.2). This means that doping concentrations have to be chosen very carefully (Escher, 1981).

Pure GaN has an electron affinity of about +3.3 eV. The depth of the BBR

near the surface of the photocathode bulk due to p-doping e.g. with Mg is typically about -1.2 eV for GaN. The activation layer will have a slightly bigger effect, lowering the effective electron affinity by almost 2.8 eV in GaN, therefore an effective NEA is achieved (Wu and Kahn, 1999).

2.2 Optimization of NEA photocathodes

In the previous chapter important parameters for NEA photocathodes were motivated and defined. On this basis, the following sections will discuss how to influence and increase the performance and quantum efficiency (QE) of NEA photocathodes.

The absolute QE of the photocathode is the ratio of photons in the desired spectral range arriving at the detector to photoelectrons leaving the photocathode. Often in the literature the fraction of reflected photons or transmittance through an UV window is not considered in QE measurements, this quantity is called the “internal QE” of the photocathode.

To achieve the goal of the highest possible absolute QE, the efficiency of each process involved must be optimised, i.e., the absorption of UV photons, the movement of electrons in the conduction band, and the emission of photoelectrons.

Further parameters of the photocathode are also important, it should be e.g. solar blind to avoid the need of filters and have a high longevity. In the following section also the main advantages of MCP detectors with photocathodes in comparison to CCD based detectors are discussed, for example their high lifetime, single photon counting abilities without the need for cooling and excellent noise characteristics.

2.2.1 Semi-transparent and opaque mode

The previous section pointed out that with an NEA photocathode, the electrons in the BBR gain momentum and thus have a higher escape probability, as they can tunnel through the thin remaining potential barrier of the activation layer. The activation layer must therefore lower the vacuum energy level relative to the conduction band edge. In the case of GaN photocathodes, this

can be achieved with a caesium layer or (several) Cs/O layers. Unfortunately, the high difference in electronegativity of caesium to oxygen (and many other chemical compounds) leads to high chemical reactivity. Therefore, the partial pressures of the residual gases to which the photocathode is exposed must always be well controlled. In Chap. 3.1.2 measurements of the partial pressure of residual gases are presented and upper limits for the most relevant elements are defined. For example, even during the formation of the oxygen layer (during Cs/O activation), the partial pressure of oxygen is only raised to the upper UHV for a maximum of minutes. Suitable detectors carrying such a photocathode must therefore ensure that these partial pressure requirements are maintained throughout their lifetime.

Consequently, there are two modes MCP detectors can be operated in, dependent on the position of the photocathode:

1. In *semi-transparent mode*, the photocathode is grown on a UV-transparent window. This window is also the main part for sealing the consequently encapsulated detector. This detector variant has the potential to be relatively lightweight and small.
2. If the photocathode is grown on the first MCP, the photocathode is operated in the *opaque mode*. In this case, the detector typically has a valve that can be opened once it is in the vacuum of space. Such a detector variant – the open detector – would be the only option to make measurements at wavelengths shorter than the corresponding cutoff wavelength of UV windows, in particular below 105 nm (LiF cutoff, see Tab. 1.1 for details). A “door” that is as simple and lightweight as possible and can be opened when the telescope finally is in space can be used for smaller missions with CubeSat-sized instruments.

In the following two sections the performance of NEA photocathodes in the semi-transparent mode and opaque mode are discussed and compared.

Semi-transparent mode

To give an expression for the number of photoelectrons per incident photon, i.e. the absolute QE, some material parameters must be defined. These should be relatively simple phenomenological functions for a given photocathode, which

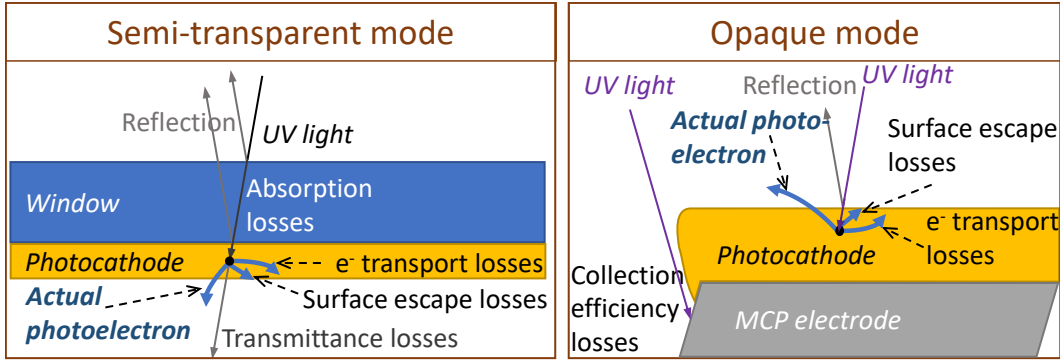


Fig. 2.5: The two modes in which a photocathode can be operated and respective loss mechanisms. In semi-transparent mode, reflection and transmittance losses occur on the window in addition to the losses found in opaque mode. In the latter mode, the absolute QE is reduced by the losses in collection efficiency, which roughly correspond to the open area ratio (OAR) of the MCP (Orlov et al., 2019). The OAR is a parameter of an MCP defined by the ratio of the total area of the pores of the MCP to the area of the electrode on which the photocathode can be grown (see also Chap. 1.2.2). On the other hand, with some photocathodes, the holes in the photocathode material can be advantageous because the photocathode surface is enlarged, as angular measurements by Siegmund et al. (2008) show

are only dependent on the Energy $E_{ph} = hf$ of the incident light with the frequency f . The reflectivity $R(E_{ph})$ of a material will also depend on the angle of incident light relative to a planar surface between two materials with different refractive indices $n(E_{ph})$. A detailed discussion about the reflectivity of photocathodes is given in Sect. 2.2.3.

If the incident photon is not reflected, it is absorbed in the bulk of the photocathode if it excites an electron to the conduction band. The absorption coefficient $\alpha(E_{ph}) = 1/l_\alpha(E_{ph})$ is the reciprocal of the absorption length. This in turn is the length at which about 63% of the incident photons are absorbed. The thickness of photocathodes with built in electric fields can be in the order of micrometres (Feng et al., 2015), but are typically in the order of 100 nm.

The excited electrons on the conduction-band edge have a certain scattering length $L(E_{ph})$, which optimally is in the range of micrometres. The scattering length depends on many parameters. For example, it becomes si-

gnificantly shorter for higher electron energies, high p-doping, due to lattice displacements or high temperature. In semi-transparent mode the thickness of the photocathode is always a compromise between the scattering length L and the absorption length l_α .

Electrons near the surface have a certain probability $P(E_{ph})$ to leave the photocathode material. P itself can be influenced by several factors, the most relevant ones for the case of NEA photocathodes with low noise characteristics are discussed in the following sections in detail. A more general overview is provided in Escher (1981) with seven factors which have an influence on $P(E_{ph})$. We already discussed the influence of surface activation (1) with caesium/Cs+O, p-doping (2) of the photocathode and the influence of the band structure (3) and orientation of the crystal. In the following sections we will further investigate the influence of the electric field (4) and temperature (5) of the material. The remaining two factors are:

- Obtaining a clean surface (6) prior to the surface activation: in the case of semi-transparent NEA photocathodes proper cleaning must take the chemical properties of the substrate into account. For example, MgF_2 is soluble in water and does not withstand some acids very well. The last cleaning process must be an in-situ process in the activation chamber, to get rid of contaminations from the cleaning solutions and the atmosphere (Machuca et al., 2002), (Smith et al., 1996).
- Strain (7): Strain can occur between the substrate and photocathode layers. It can occur with temperature changes (see Sect. 2.2.4), due to doping, chemical reactions or due to external pressure. If the strain is not properly controlled, the QE may decrease or cracks may appear in the photocathode layer. On the other hand “strain engineering” has the potential to improve, for example, the stability of a photocathode, the size of its band gap, or the escape probability (Xia et al., 2016).

The last parameter needed for the description of the absolute QE is $\alpha_{PE}(E_{ph})$. It represents the fraction of the absorption where the electrons are excited above the vacuum level. Simplified, this is already the case for NEA photocathodes when these electrons are in the conduction band. So, in the optimal

case, $\alpha_{PE}(E_{ph})$ is a step function with a value of about zero for photon energies below the band gap and a value of one for photon energies above the band gap. The fraction α_{PE}/α then describes the fraction of excited electrons per UV photon within the absorption length of the photocathode. Hence, it is a measure for the transmittance losses indicated on the bottom left of Fig. 2.5. Another useful fraction is l_α/L , i.e. the ratio of the optimally short absorption length of the photocathode and the optimally long scattering/diffusion length, each dependent on the frequency of the incoming light (Spicer and Herrera-Gomez, 1993). The correspondent quantity in Fig. 2.5 is the electron transport losses.

In summary this means the absolute QE in the semi-transparent mode is given by (Spicer and Herrera-Gomez, 1993):

$$QE(E_{ph}) = (1 - R) \frac{P \times \frac{\alpha_{PE}}{\alpha}}{1 + \frac{l_\alpha}{L}}$$

The internal QE of the photocathode is larger as it does not include reflection by the factor $1/(1 - R)$.

In the following sections a further discussion on the QE optimization and some parameters important for the photocathode performance is given. In Sect. 2.2.4 the influence of the electric field on semi-transparent photocathodes is detailed, also showing that the maximum resolution of the photocathode is dependent on the distance to the first MCP and the internal or external electric fields.

A discussion regarding the longevity of the photocathode can be found in Sect. 2.2.5. In the semi-transparent mode the damage due to bombardment with positively charged ions which are accelerated by the MCP voltage is obviously larger than in the opaque mode. In turn a window would keep the partial pressure of Cs high in a sealed detector, probably leading to a slower Cs loss rate, especially if smaller temperature peaks occur.

Semi-transparent mode may also require metallization of the windows with a sufficiently low sheet resistance to prevent charging of the photocathode. Details are presented in Chap. 1.2.1. Also the influence of the lattice mismatch and surface roughness are presented there. If high growth temperatures are required, the mobility of the window material atoms can get high and they diffuse into the photocathode material. The effect was measured by Meyer et al.

(2020b) for MgF_2 temperatures above 650°C . At even higher temperatures this could be one effect that leads to a detachment of the photocathode from the window.

Opaque mode

If an open detector is required, e.g. to register spectra of stars below the cut-off wavelength of typical UV windows, the photocathode has to be grown on the top surface of the first MCP. This requires the MCP to withstand the high temperatures during the photocathode growth. In the worst case a peeling of the NiCr layer from the MCP surface could occur. Passivation layers could be used to avoid poisoning of the MCP channels. Further details are discussed in Chap. 1.2.2.

The absolute QE of photocathodes in opaque mode differs from that in semi-transparent mode only in a few details. In Fig. 2.5 it can be seen that in the semi-transparent mode the incident light is reflected on the transition layer between the vacuum and the window, a second transition layer is between the window and the photocathode. In opaque mode there is only a single material transition between the vacuum and the photocathode layer. Also measures to reduce the reflectivity of the photocathode, discussed in Sect. 2.2.3, often require the photocathode to be in opaque mode. Therefore, the reflectivity R_O is often smaller than the reflectivity R in the semi-transparent mode.

Furthermore there are less transmittance losses in opaque mode. The photocathode thickness should be in the order of a few diffusion lengths, so that nearly all incident light is absorbed.

2.2.2 Low-energy cutoff and high-energy drop

Low-energy cutoff

As the detector should be solar blind, we want only UV photons with a certain threshold energy of above 3.1 to 4.1 eV to be absorbed in the photocathode material and eventually lead to a photoelectron leaving the photocathode. The lowest possible energy a photon can have while still able to excite an electron in a crystal, is given by the band gap E_g .

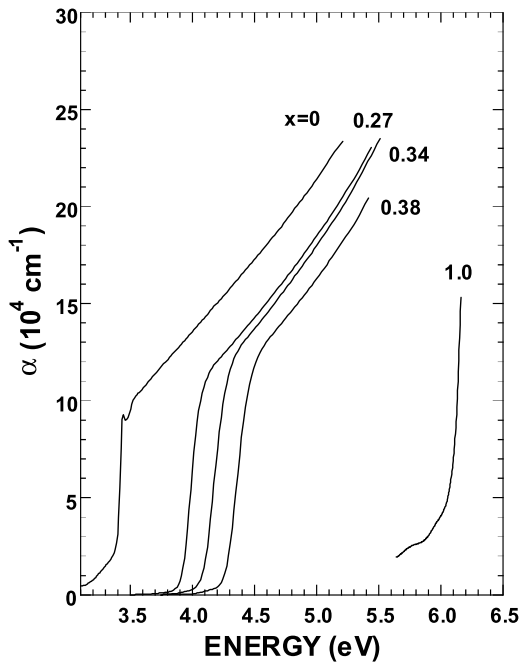


Fig. 2.6: Absorption coefficient of $\text{Al}_x\text{Ga}_{1-x}\text{N}$. For each material composition there is a sharp rise in the absorption just before the band gap of the material (Muth et al., 1999)

The band gap of many photocathode materials can be “tailored” to the respective needs of a certain mission or detector, e.g. in the case of $\text{Al}_x\text{Ga}_{1-x}\text{N}$ ($x \in [0, 1]$) with a higher amount of aluminium, the band gap gets bigger, as can be seen in Fig. 2.6. Likewise, it is possible to include the visible range by using a certain amount of $\text{In}_{1-x}\text{Ga}_x\text{N}$, with the band gap of InN being at just 0.8 eV. How these changes in the material composition can also be used to induce internal electric fields is explained in Chap. 2.2.4.

High-energy drop of NEA photocathodes

Depending on the photocathode design it is possible that there is also a region with a high-energy drop or even cut-off. For the closed design (see Chap. 2.2.1)

the cut-off of the window material or a metallization will limit the observable spectral range, as detailed in Tab. 1.1 and Chap. 1.2.1.

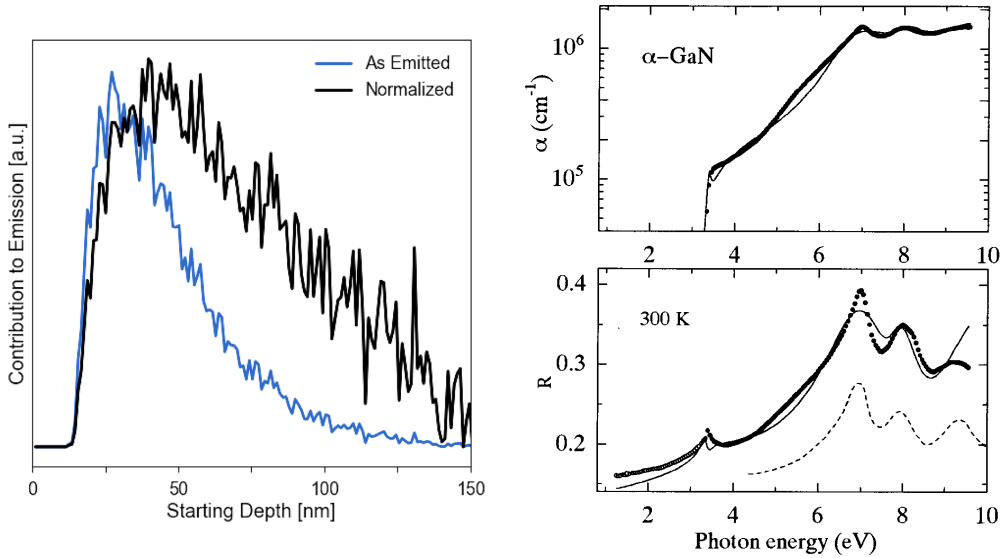


Fig. 2.7: Left: Monte Carlo simulations of photoexcitation in a p-doped but unactivated GaN photocathode by Marini et al. (2018a). The starting depth is the distance between the surface of the photocathode and the depth the photoexcitation took place. Each pixel on the abscissa is therefore associated with a certain depth slice of the simulated photocathode. After the simulation, the fraction of electrons from each depth slice was evaluated and plotted as the blue curve (“as emitted”). To visualize that the cut-off at small starting depths cannot be explained by a smaller number of total excitations per depth slice, an additional “normalized” curve was plotted. For this curve the number of photoexcitations per depth slice was held constant. The escape probability of electrons must therefore have been lower within the depletion region.

Right: Absorption coefficient and reflectivity of hexagonal GaN from Kawashima et al. (1997). Solid lines are calculated values, dots are measurements. After linearly rising, the absorption coefficient is nearly constant at photon energies above $7 \text{ eV} \hat{=} 177 \text{ nm}$ wavelength. The reflectivity shown is for light perpendicular to the photocathode layer. The reflectivity can be very high, with a maximum of about 40% at 7 eV (177 nm)

In the opaque mode (see 2.2.1) the properties of the photocathode material have to be observed. There are several effects that will mutually influence each other:

1. The wavelength dependent absorption coefficient of the photocathode becomes larger with shorter wavelength, as more interband transitions from one of the valence into one of the conduction bands become possible for higher electron energies (Kawashima et al., 1997). The effect can lead to an increasing number of electrons that are excited within the depletion width W of the photocathode.
2. Via simulations by Marini et al. (2018a) the left image of Fig. 2.7 was obtained. It illustrates the cut-off for electrons originating from the depletion layer as their escape probability is very low. The reason is that after the excitation, the electrons with starting depths smaller than the depletion width W (see Fig. 2.4) are excited into the bent conduction-band region and due to their low energy level compared to the vacuum level, their escape probability drops sharply. However in the simulations by Marini et al. (2018a), the maximum photon energies were at 6 eV, only about 1.6 times higher than the band gap of GaN.
3. At a photon energy of about twice the band gap energy, even at a starting depth smaller than W , the escape probability can rise again. This is because electrons can be excited to conduction bands that are closer to the vacuum level or have a high velocity after excitation. The latter are so called “hot” electrons. They can not necessarily leave the photocathode material directly. There is no preferred direction for these “hot” electrons and it is therefore equally likely for them to move further into the photocathode material as it is to move closer to the surface. Moreover, these “hot” electrons do not move in the conduction band and therefore have a very short *scattering length*. In Spicer and Herrera-Gomez (1993, chap. 4) it is shown that the mean free path of the “hot” electrons will drop exponentially with increasing electron excess energy and could be only 1 nm or less for excess energies above the conduction-band level of only some electron volts. It is therefore very likely for such a “hot” electron to have many nearly elastic electron-phonon scattering events or that electron-electron scattering occurs. They will be able to exit the photocathode if their energy stays above the vacuum energy level. In the case of p-doped NEA photocathodes they could reach the conduction band in

the bulk of the photocathode as “cold” electrons. These “cold” electrons move slowly in the conduction band and their *diffusion length* is in the order of micrometres. To summarize, due to the small scattering length not all excited electrons can leave the photocathode and the QE drops for the corresponding spectral range.

4. If the incident photon energy is above several E_g , the QE will rise again. It can even exceed values of one¹, i.e. due to electron-electron scattering, high energetic electrons will “lift” valence band electrons into the conduction band. These “lifted” electrons can then leave the photocathode (Aslam et al., 2005b).

Also the effect of electrons that cannot leave the depletion layer/BBR becomes less relevant above certain electron energies, as the bands are only bent with about 1–2 eV in the depletion region (for details see Spicer and Herrera-Gomez (1993)).

These effects can lead to a drop of the QE for higher energies in the case of NEA p-doped photocathodes. The curve shape of Fig. 2.8 showing the QE of a GaN photodiode between 5 and 500 nm can be understood as a result of these “competing” effects.

2.2.3 Reflectivity of photocathodes

An incoming photon has a certain chance to be reflected or absorbed by the detector window in case of a closed detector design, i.e. the transmittance T of the window should be as high as possible, accordingly its reflectivity R as low as possible (see Chap. 1.2.1 and 2.2.1).

The reflectivity of a material in vacuum for incident unpolarized light is given by

¹When designing the detector electronics, it would be beneficial to enable them interpret such events correctly if they occur relatively often in comparison to single photo-electron events. Charge amplification chips are often optimised with a set of trigger parameters to detect charge clouds triggered by a single photo-electron. Consequently, they would ignore such events if the shape or size of the charge cloud is not within the trigger range and the photon data would be lost.

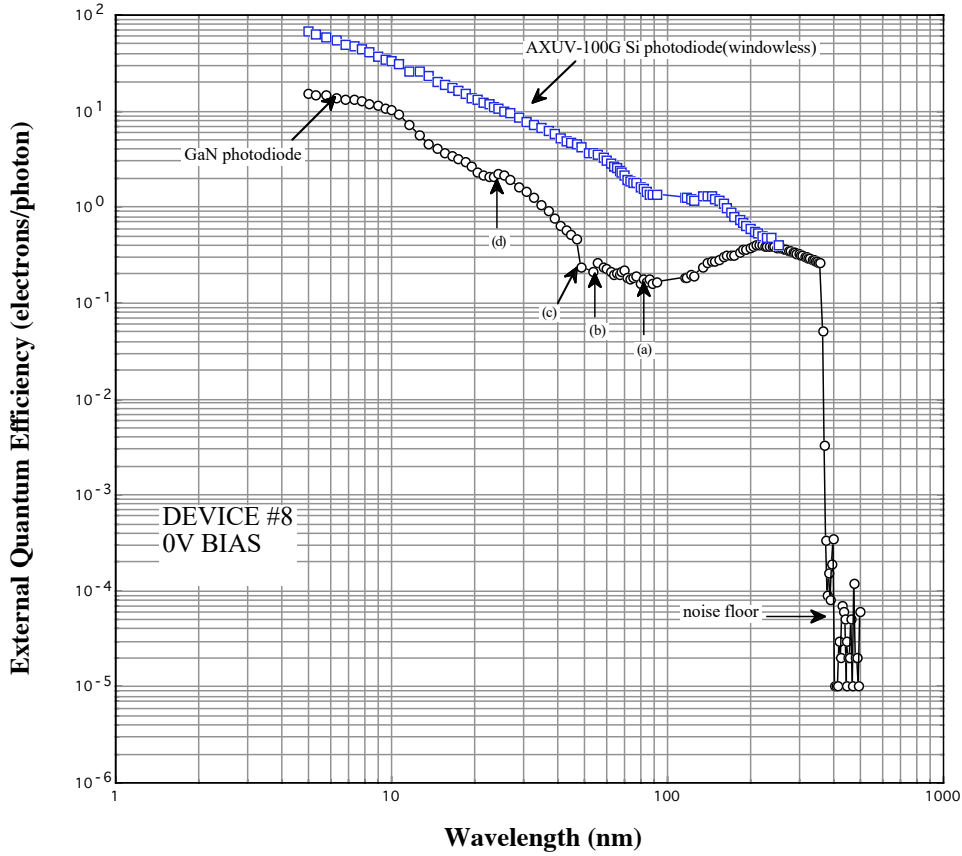


Fig. 2.8: Relative QE (only absorbed photons) of a GaN Schottky photodiode from Aslam et al. (2005a). A photocathode could show similar results if corrected for reflectivity. At 213 nm a first maximum is reached, with a relative QE of 40 %. Point (a) refers to a minimum QE of about 16 %. The measurements were taken at three different facilities at NIST to cover the whole spectral range, at some points the curve is not as smooth as expected. For example point (c) is at the border of the measuring range of two experimental setups which seem to have slightly different calibrations (Aslam et al., 2005a)

$$R(\lambda, \phi) = \frac{R_s(\lambda, \phi) + R_p(\lambda, \phi)}{2} \quad (2.1)$$

with R_s and R_p being the reflectivity for s-polarized and p-polarized light respectively and ϕ the incident angle of the light, with an angle of 0° for light beams perpendicular with respect to a flat photocathode surface. In the case

of a photocathode in vacuum these quantities are given by

$$R_s = \left| \frac{\cos(\phi) - n(\lambda) \times \sqrt{1 - \left(\frac{\sin(\phi)}{n(\lambda)}\right)^2}}{\cos(\phi) + n(\lambda) \times \sqrt{1 - \left(\frac{\sin(\phi)}{n(\lambda)}\right)^2}} \right|^2 \quad (2.2)$$

$$R_p = \left| \frac{\sqrt{1 - \left(\frac{\sin(\phi)}{n(\lambda)}\right)^2} - n(\lambda) \cos(\phi)}{\sqrt{1 - \left(\frac{\sin(\phi)}{n(\lambda)}\right)^2} + n(\lambda) \cos(\phi)} \right|^2, \quad (2.3)$$

where $n(\lambda)$ is the wavelength dependent refractive index of the photocathode (Fresnel, 1868). In Eq. 2.2 and Eq. 2.3 it can be seen that the reflectivity is dependent on only a few quantities: the polarisation and wavelength of the incident light, the angle it falls onto a surface and the refractive indices of the two materials that form the boundary layer the light interacts with. These sizes are mostly determined by the optical path in the astronomical instrument in which the detector will be installed. If the optical path cannot be changed, an optimization of the reflectivity is hardly possible. When planning the optical path of light in an instrument, the angle at which the light falls on the image plane could be taken into consideration by using a lookup table as shown in Fig. 2.9. In the case of high numerical apertures, the absolute QE will decrease sharply for incident angles above 60–70°, as more light is reflected.

There are only few options to optimize for the reflectivity. Either by minimizing the angle of incidence of light or by choosing window materials with their $n(\lambda)$ as similar to the refractive index of the photocathode as feasible if operating the photocathode in the semi-transparent mode.

Another more advanced possibility is to choose different surface geometries. By nanoprocessing the surface of pure silicon samples, Yang et al. (2014) demonstrated that the reflectivity of this surface was drastically decreased. The nanostructures on the surface of such a sample reflect the incident light like classically expected, but the tailored structure, so called nanowires, are “trapping” the reflected light, increasing the overall absorption. For photocathode materials such as GaN the diameter, length and spacing between nanowires can be controlled (Hersee et al., 2006). In Xia et al. (2017) it is shown that via simulations an optimal set of parameters can be found for the specific use-case of the photocathode. They optimised for a wide set of parameters including

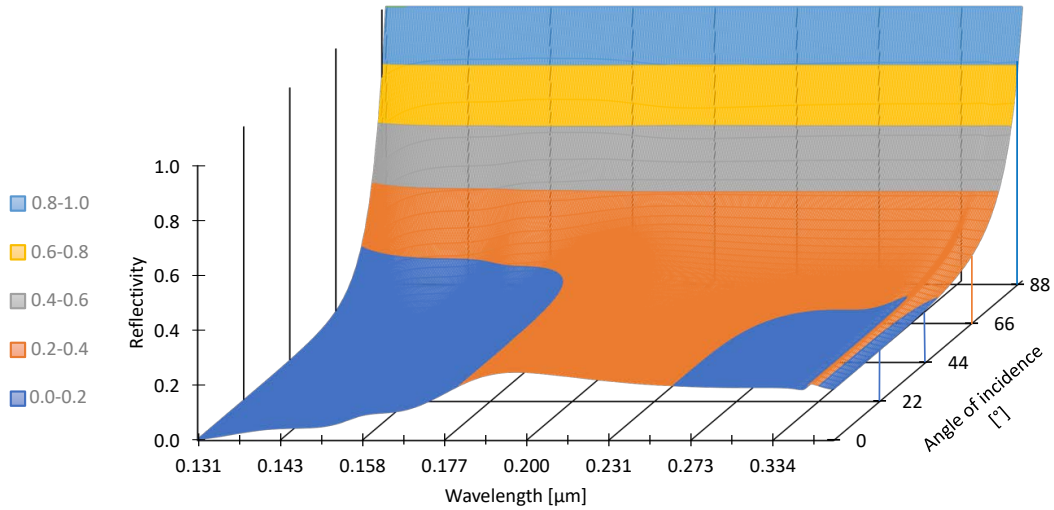


Fig. 2.9: Reflectivity $R(\lambda, \phi)$ of GaN for incident light in vacuum. Colours refer to the reflectivity ranges defined on the left. For small wavelengths the refractive index is not much bigger than one and the reflectivity is therefore very low for small angles. At about $0.2 \mu\text{m}$, the refractive index of GaN has a value of about three, leading to a relatively high reflectivity of above 20% even for small angles of incidence. For incident angles greater than about 70° , the reflectivity starts to become very high for all wavelengths. Values for $n(\lambda)$ were taken from Kawashima et al. (1997), and inserted in Eq. 2.1, using Eq. 2.3, 2.2 and angles between 0° and 90°

the height of the nanowires (NWs), the angle of incident light, and a p-doping concentration gradient. The latter means that the top of the NWs could have a different doping concentration than the bottom of the NWs.

However, during the transfer and transportation of a photocathode between different vacuum vessels, the surface could be contaminated, especially as the nanostructure leads to a greatly increased surface. After surface activation with caesium the photocathode must remain in an UHV environment, making such transportation a complex task. Whether nanowires would survive the vibrations during a rocket launch is yet an open question. Nevertheless, it should be considered to use appropriate nanostructures, as this often allows a further increase in quantum efficiencies that would otherwise not be possible.

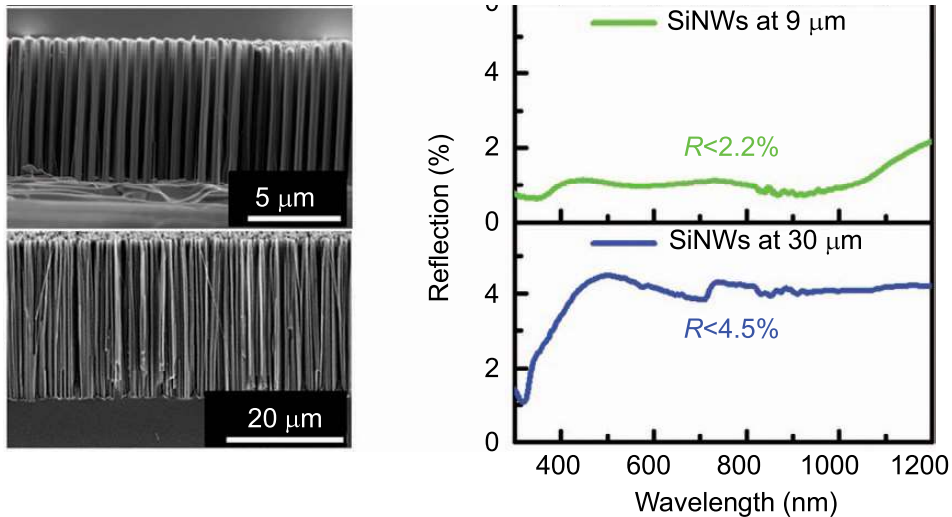


Fig. 2.10: SEM images of silicon nanowires (SiNWs) and their reflectivity. An untreated flat silicon surface would have a reflectivity of 30 to 50 %. Images were taken and modified from Yang et al. (2014)

2.2.4 Electric field and temperature

Electric field

An electric field can accelerate electrons in the conduction band of a photocathode, giving them a higher escape probability. There are two possible ways how an electric field in the photocathode crystal can be achieved. Either a voltage is applied between the photocathode and the surface to which the photoelectrons are to be accelerated, or an effective electric field is achieved by a graded p-doping of the photocathode, as shown in Fig. 2.11.

As discussed in Barnstedt (1985), if an MCP detector is operated in the semi-transparent mode, the distance L between the photocathode and first MCP should be very small, and a voltage U should be applied between these two components. Assuming that electrons leave the photocathode with a cosine emission energy distribution, the resolution R in line pairs per mm with a contrast of 3% per line pair is given by $R = 0.4 \frac{1}{L} \left(\frac{eU}{\epsilon} \right)^{0.5}$ (Csorba, 1977). ϵ is the most probable electron energy for that distribution and e the elementary charge. The voltage U can be up to 100 V², while the distance L can be in the

²If such a high voltage is applied, the requirements for the maximum variation of L are also very high. In the worst case, field emission or even a short circuit may otherwise occur.

order of 0.1 mm. This corresponds to an electric field of nearly 10^4 V/cm.

Such an electric field can accelerate electrons in the conduction band to the surface of the photocathode, reducing the work function per elementary charge e by an amount of $\sqrt{\frac{eE}{4\pi\epsilon_0}}$, with E the electric field and ϵ_0 the vacuum permittivity (Escher, 1981, chap. 3.10). With the electric potential and distances necessary to increase the resolution of the detector, the electrons in the conduction band would gain energy in the order of 20–40 meV. A detailed discussion about the corresponding increase in escape probability, which is greatly influenced by doping concentrations and surface activation levels is presented in Howorth et al. (1973). In short, the scattering length of electrons in the conduction band is strongly dependent on their kinetic energy and the doping concentration of the photocathode crystal. Electrons in the conduction band (“cold” electrons) have diffusion lengths in the order of micrometres, high doping concentrations can shorten the diffusion length. If these electrons are accelerated, they could become “hot” and have scattering lengths in the order of only a few nanometres. These scattering events can make electrons lose the gained momentum, leading to only slightly higher escape probabilities for higher electric fields. In general for NEA photocathodes in semi-transparent mode, the escape probability and therefore QE of a photocathode can be raised by a factor of about 1.5 with suitable electric fields (Escher, 1981). On the downside, also the secondary emission of electrons and the dark current of a photocathode will rise by approximately the same factor. An increased number of scattering events can spread also the energy distribution of the photoelectrons, decreasing the resolution.

As mentioned at the beginning of this section, another method to achieve a drift of electrons to the surface is, by tailoring the band structure to generate an internal electric field. This method is called “exponential” or “graded” doping, meaning that the p-doping concentration is lowered constantly during the growth of the photocathode, or individual layers with decreasing p-doping concentrations are produced. Such doping results in a band diagram as illustrated in Fig. 2.11. A certain difference in the doping concentration N will lead to a difference in the potential energy of electrons in the conduction band of $k_0T \ln \frac{N_1}{N_2}$ (Fu et al., 2011). The expression k_0T is a measure of the average kinetic energy of particles at a given temperature and is about 26 meV at 300 K.

If the doping concentration is reduced by a factor of $e \approx 2.7$, the band energy would thus decrease by 26 meV. To translate into an increased QE of the photocathode, again the relevant question is, whether the escape probability for electrons being accelerated due to these potential differences is increased. On the right of Fig. 2.11 the results of Fu et al. (2011) show that an increase in the QE of a photocathode by a factor of about 1.5 to 1.7 is possible.

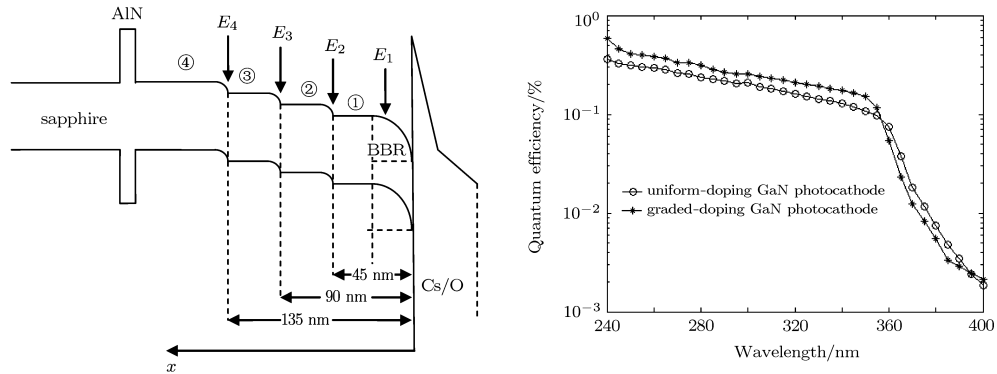


Fig. 2.11: *Left:* Schematic energy band diagram of grade doped GaN on a sapphire substrate with the layers 1 to 4, each with a thickness of 45 nm. Such a band structure leads to a drift of conduction-band electrons to the surface of the photocathode, in this case with a Cs/O activation layer. The BBR leads to further acceleration of the electrons, increasing the tunnelling probability through the thin energy band of the Cs/O activation layer above the vacuum level (Fu et al., 2011).

Right: Quantum efficiency of uniformly p-doped GaN and graded-doped GaN. At 240 nm Fu et al. (2011) reached a QE of about 35 % for a uniformly doped GaN photocathode, the QE of their grade-doped GaN photocathode is higher by a factor of about 1.7 at the same wavelength

It is possible to change the material composition of the photocathode gradually. In the case of GaN there are two alloys, $\text{In}_{1-x}\text{Ga}_x\text{N}$ and $\text{Al}_{1-x}\text{Ga}_x$ which are miscible with each other. As mentioned in 2.2.2 these alloys can be used to adjust the low energy cut-off of the photocathode more into the visible range or VUV respectively. With graded doping, an internal electric field can be generated so that electrons drift to the surface (Machuca and Liu, 2008). Such miscible photocathodes can have layers where the absorption of light is favoured. For example, the surface recombination that leads to a drop in QE of p-doped GaN photocathodes in the range of about 50–100 nm (see. Fig. 2.8)

could be avoided by having top layers with a mixing ratio that makes them more transparent to light of this wavelength.

Temperature

Varying the temperature of the photocathode has several impacts on the photocathode production and on the performance of the photocathode during operation.

For the production of the photocathode the temperature is one of the most important growth parameters. E.g. for achieving a lower mismatch between the atoms on the surface of a (001) MgF_2 substrate and the atoms of the GaN crystal, the growth of cubic β -GaN is favourable. Such a growth is achieved at a relatively low temperature of about 450°C , at higher temperatures more hexagonal GaN with higher mismatch to the substrate will form. Lowering the temperature will also reduce the mobility of atoms during growth which is needed during crystal production, as they have to migrate randomly through the forming crystal structure until they stay in a potential minimum at one of the crystal lattice points. This mobility depends on the substrate temperature during growth, but also on the chemical element, so there can be different mobilities for the respective reactants during the growth of a photocathode alloy. In the case of GaN, the lower mobility of gallium compared to nitrogen can be compensated by forming a Ga-reservoir before starting the nitrogen flow. This reservoir is maintained throughout the growth process by a high Ga flux and can be “depleted” at the end (Meyer et al., 2020a).

During the activation with caesium of a photocathode material to achieve the NEA, a high mobility of caesium can also be favourable. In the case of Cs_2Te the caesium atoms have to diffuse into a several nanometre thick layer of tellurium. At the same time the desorption of caesium will start at relatively low temperatures of above 50°C , until a certain partial pressure of caesium is reached. On a sealed detector such a partial Cs pressure can stop further evaporation of Cs. At temperatures above 200°C the desorption of Cs will be independent from the partial Cs pressure (Escher, 1981). The desorption of caesium thus limits the maximum temperature the detector may be exposed to for further processes (e.g. getter activation), as well as the storage temperature

and operating temperature³.

In the case of GaN, the binding energy between Ga and N atoms is in the order of 10 eV/atom, making the material very stable against even higher temperatures, chemical etching, degradation and radiation. For such stable crystals a clean surface can be obtained relatively easy by removing excess Ga and surface contaminations by etching, and heating to high temperatures. During the activation phase, Cs can bind directly to the GaN crystal with a high binding energy as well. As a result, even at temperatures of above 200°C, at least one layer of Cs would remain on GaN as long as no surface contamination was present at the start of Cs-activation (Machuca and Liu, 2008).

The QE of NEA photocathodes is temperature dependent. In the case of thermal electron emission (see Sect. 2.1.3), a wolfram filament is heated to high temperatures. During scattering events, the average exchange in energy due to the temperature of the photocathode material is k_0T with a Maxwell-Boltzmann distribution describing the probability to find particles within a certain momentum range. Some electrons will have a high momentum and are lifted above the relatively high vacuum level compared to the conduction-band level in a metal. Consequently, they can leave the photocathode. A more complete review on this topic can be found in Escher (1981, chap. 3.10.) or Hermanutz (2015). The temperature range ΔT_{Det} that a sealed MCP detector can be operated in, is quite narrow, typically $\Delta T_{Det} \approx 240$ K to 350 K (Escher, 1981). Therefore, only a slightly higher exit probability is to be expected. On the other side the diffusion length of the electrons gets shorter for higher temperatures, hence the influence on the absolute QE depends on the full set of parameters of the photocathode.

The temperature dependence of the size of the band gap is described by Varshni (1967). For GaN and most NEA photocathode materials the band gap will get bigger at lower temperatures, meaning that the low energy cut-off goes to higher energies and electrons that have reached the conduction band have more potential energy in comparison to the vacuum, i.e. the NEA and therefore escape probability is higher.

³For the sealed detector variant, the melting temperature of the sealing solder is probably the most restrictive factor.

As second to the last point the electric resistance of materials is influenced by temperature, see also the discussion of this topic on the electrical resistivity of MCPs in Chap. 1.2.2. For a given film thickness and doping concentration, due to the small ΔT_{Det} , no large change in resistivity is expected. A significantly higher resistivity would lead to charging effects in the photocathode and therefore lower the QE, if the photocathode is not electrically contacted on its whole surface by a metal film. For p-doped silicon with a moderate doping concentration one can calculate⁴ that the resistivity would increase by a factor of about two for the temperature range ΔT_{Det} .

Each material has its own coefficient of thermal expansion. During photocathode growth, the substrate is initially hot, and then cools to room temperature. A large difference in thermal expansion coefficients can therefore result in a mismatch between substrate and photocathode layers and corresponding strain (see Sect. 2.2.1). Such strain can lead to lower QE, and in extreme cases, entire layers can become detached. Strain can be reduced by using more suitable material compositions with lower thermal expansion mismatch or buffer layers as used in Ishigami et al. (2012).

2.2.5 Longevity of the photocathode

For a specific mission, the longevity of each part of the detector must be designed to survive the missions duration. The most critical parts of the detector with regard to its longevity are the MCPs (see Chap. 1.2.2) and the photocathode. Residual gas and ion feedback from the MCP will lead to a bombardment of the photocathode with particles. Also the adhesion of the photocathode layer to the substrate it was grown onto has to be very strong, as the detector is required to survive the vibrations and corresponding forces that occur during a rocket launch.

Stability

A sealed tube photo detector with a caesiated photocathode has a certain “shelf life” meaning the time scale a detector maintains its performance within the

⁴PV Lighthouse: Resistivity calculator, <https://www.pvlighthouse.com.au> [18.03.2021]

required level. The shelf life is one of the main factors determining detector longevity, but does not consider external factors like ion feedback or radiation hardness. The decay of the QE of photocathodes in a vacuum chamber is shown in Fig. 2.12 on the left. In a Cs/O activation layer the decay can be fully explained by the role of oxygen in the vacuum system and the layer itself (Machuca et al., 2003). In sealed tubes with small volumes, a high partial pressure of caesium will help to maintain the QE for caesiated GaN photocathodes. No degradation was measured by Siegmund et al. (2003) for sealed tube samples even after several years.

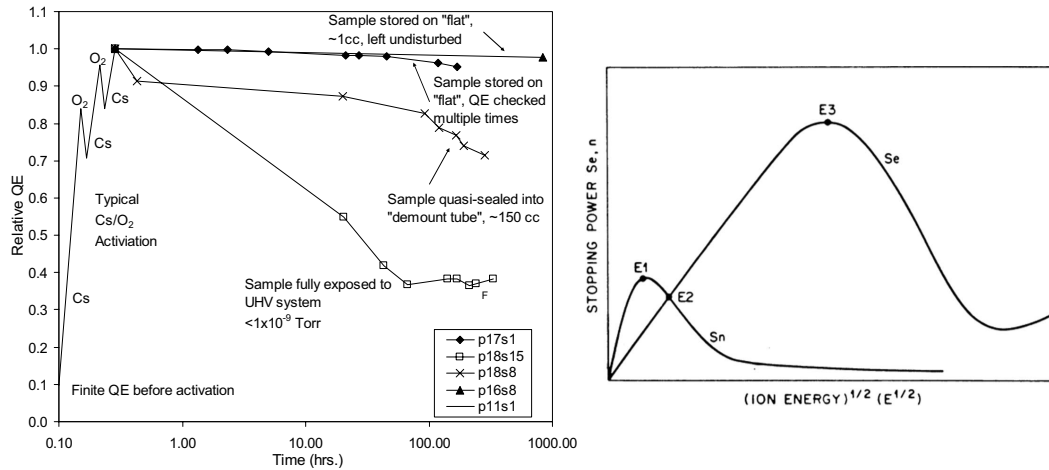


Fig. 2.12: Left: Relative quantum efficiencies of GaN samples at 254 nm during activation and stability tests. After the activation all samples start at a rel. QE of one per definition. Sample “p18s15” was placed in the vacuum system with one side facing the whole vacuum system with a relatively high partial pressure of oxygen and water, leading to a slow decay of the QE over time. Sample “p18s8” was left inside the activation system (“demount” tube) with a smaller volume below and a slower decay of the QE. Samples “p17s1” and “16s8” were placed directly on a slightly caesiated surface with nearly no QE losses. Even high partial pressures ($\approx 10^{-8}$ Torr of nitrogen and hydrogen) did not lead to QE losses (Stock et al., 2005).

Right: The stopping power of electronic processes (Se) and interactions with atomic cores (Sn) plotted vs. the square root of the energy (\propto velocity) of ionizing particles. The stopping power is proportional to the cross section of atoms, which is in turn proportional to the expected value of the energy loss of the ionizing particles per unit length. The points E1, E2 and E3 are at energies of 20 keV, 40 keV and 8 MeV, respectively, in the case of GaN (Pearton et al., 2015)

Influence of ionizing radiation on photocathodes

To measure the light of astronomical UV sources, the UV instrument including the detector has to be deployed at least at stratospheric balloon altitudes (about 38 km or higher) or in space. But avoiding the absorption and scattering mechanisms of earth’s atmosphere leads the detector to be exposed to the high radiation level of space. Every component of the detector, including the on-

board electronics and the photocathode must therefore be sufficiently radiation hard. Furthermore, the photocathode is target of positively charged ions that are accelerated towards the photocathode due to the high voltage applied to the MCP stack. A full review of the interaction of radiation with GaN devices and damage that can be caused by this radiation is given in Pearton et al. (2015).

In short, damage applied is dependent on the kind of irradiation and its energy. Possible irradiation particles could be protons, electrons, gamma rays, neutrons and ions. Their interaction with an atomic core of the photocathode material is likely to lead to displacement damage, this means due to a collision an atomic core could have more kinetic energy than the lattice-displacement energy and leave its previously well-defined position in the crystal. Such displacements in a crystal would lead to a shorter diffusion length for electrons in the conduction band, lowering the internal QE of the photocathode. The cross section for GaN atom cores has its maximum at ion energies of about 20 keV.

If the collision occurs between the ionizing radiation and electrons of the substrate, this electron is lifted far above the conduction-band edge. Additional energy of the electron can be sufficient to excite another electron to the conduction band or is converted into heat. This means the radiation will lead to a certain radiation background measured by the UV detector, but will not damage the photocathode.

The high lattice-displacement energy of GaN, its low cross section for damaging radiation due to core processes, and relatively thin layers (about 100 nm) that are required for photocathodes add up and lead to a high resilience of GaN photocathodes to radiation (Pearton et al., 2015), especially if compared to CCDs.

Chapter 3

Measurements and results

The following sections will present measurements and achievements on the photocathode production and the sealing of detector bodies. For that purpose a test setup was used with an UHV system as the central component. An in-depth description of that system is given in Hermanutz (2015) and its user manual. Therefore, in this chapter a short description of the whole laboratory setup is given, but the focus is on the properties of the parts of the UHV setup which are important to understand the measurements.

3.1 Laboratory setup

3.1.1 UHV system

Throughout the Chapters 1 and 2 it became very clear that for the production of photocathodes and sealed detectors very high requirements have to be met. Especially during and after the caesiation of GaN and CsTe photocathodes the total pressure needs to be in the order of 10^{-9} mbar, with higher requirements for some partial pressures (see Sect. 3.1.2).

For this reason the photocathodes are produced in a UHV chamber which will be referred to as the “Cathode Vessel”, see Fig. 3.1 on the left for an image of the vessel from the outside. Up to six substrate holders can be installed in the UHV vessel. For the measurements presented in Sect. 3.3 and following, one batch of samples consists of five “test samples” with a diameter of 2.50 cm. The sixth sample holder is not installed, the resulting opening allows the position of

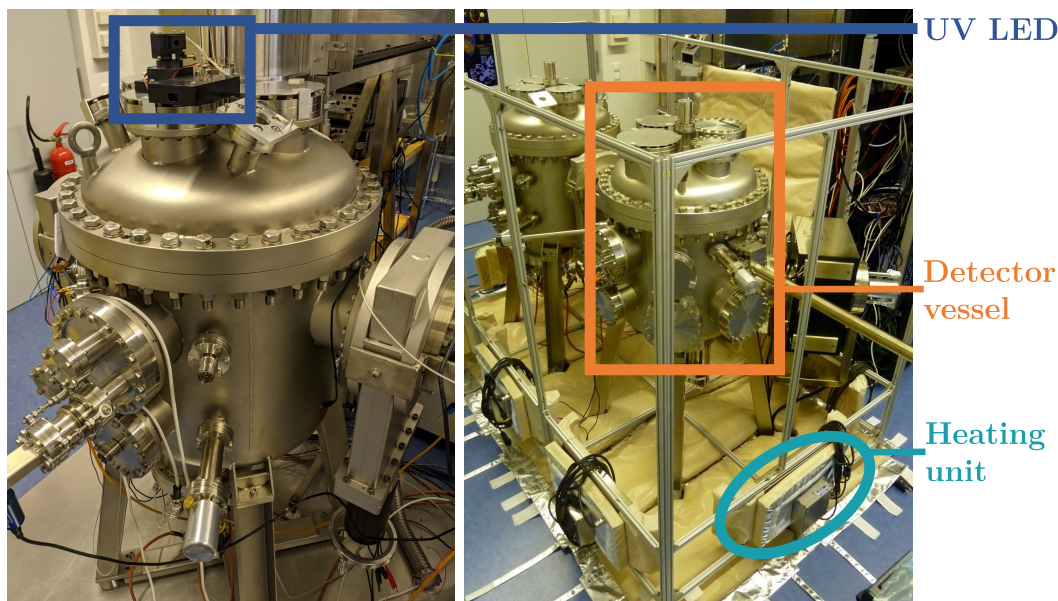


Fig. 3.1: *Left:* Cathode Vessel with mounted UV LED lamp on top. *Right:* Detector Vessel during the assembly of the heating tent

components below the sample turntable to be checked. After reconfiguration in February 2021, three detector windows (see Chap. 1.2.1) and three “test samples” can be installed. Regardless of the configuration, the substrates can then each be moved to three different positions where they are further processed:

- The “photocathode processing position” to clean, produce or activate photocathodes. On the left of Fig. 3.2 a cross sectional view is shown with a part of the tube and half of the Cathode Vessel blanked out. This allows the parts otherwise hidden inside the vessel and tube to be seen, which are required for the process steps carried out at this position.
- The “QE measurement position” to determine an absolute value for the minimal quantum efficiency of the photocathode.
- The “transfer position” where substrates can be picked up to be transferred into the Detector Vessel or vice versa.

Photocathode processing position

On the photocathode processing position, which is shown in Fig. 3.2, all process steps from the sample cleaning to the activation of photocathodes can be

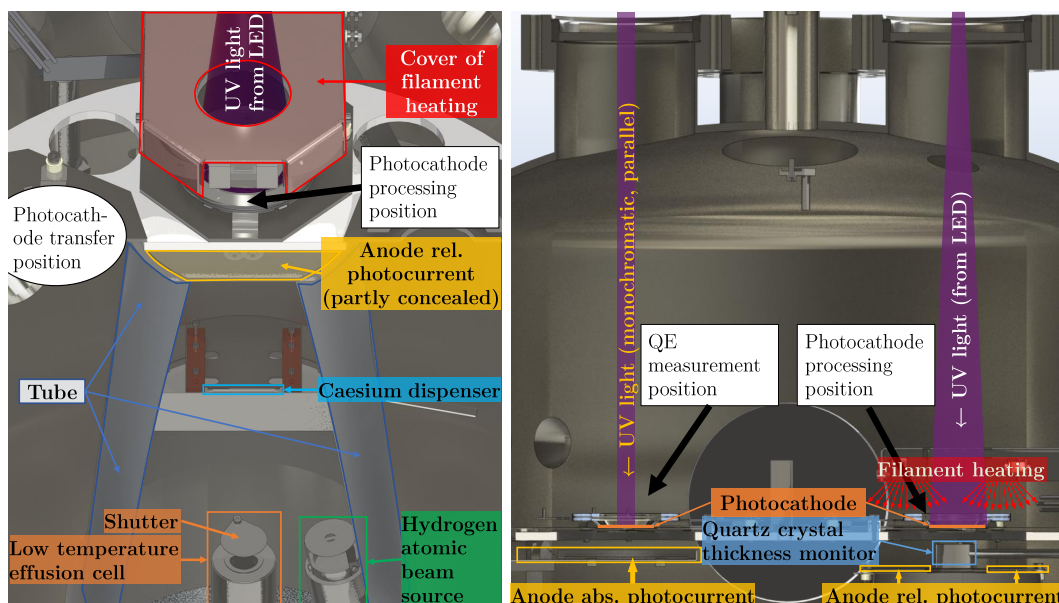


Fig. 3.2: Cross sectional views of the Cathode Vessel. *Left:* Half of the vessel and parts of the tube are hidden to allow a look on the components needed for photocathode production. Leftmost is the position where photocathodes are positioned before the cathode transfer. *Right:* View inside of the vessel with the focus on the two measurement positions

performed. The first step after a new batch of samples is placed in the vessel and the pressure inside of the vessel is in the high vacuum regime, is to bake each sample out for 24 hours with the filament heating. The goal is to remove contaminants such as water condensation on the samples. Based on the sample type a temperature of 150°C to 250°C is chosen. If the pressure is well below 10^{-5} mbar, a Hydrogen Atomic Beam Source (HABS¹) can be used to produce an ion-free atomic hydrogen gas beam to further clean the sample. After each activation step, the HABS can be used for further optimization of the photocathode, as described by Norton et al. (2003).

When the total pressure is at or below 10^{-9} mbar, the requirements for photocathode activation are met (a more precise definition is given in Sect. 3.1.2). For caesium telluride photocathodes, the exact parameters for tellurium and caesium layer thickness, respective evaporation rates and temperatures could be slightly varied, but the following steps are the same in each case:

¹Data sheet: <https://www.mbe-komponenten.de/products/pdf/data-sheet-habs.pdf>, [18.03.2021]

The substrate is heated slowly and uniformly for one hour by the filament heating. The low temperature effusion cell is heated to increase the vapour pressure of the solid tellurium to the desired amount while the shutter remains closed. Before opening the shutter, the temperature of the effusion cell and filament heating is lowered by a few Kelvin to minimize evaporation of surface water. The layer thickness and growth rate are measured with a quartz crystal thickness monitor (see Fig. 3.2, bottom right).

During activation, a caesium dispenser is heated very carefully because the heating current required to result in a given caesium rate depends on the amount of caesium in the dispenser. To measure a photocurrent that is proportional to the quantum efficiency of the photocathode, two conditions are met in the experimental setup: First, the photocathode is illuminated with focused UV light of constant luminous intensity, this is generated by a UV LED. Second, as described in Chap. 2.2, the resulting photoelectrons must be accelerated towards an anode with a given voltage. Thus, at any given time, a given number of electrons per second, given by the QE, leave the photocathode and are collected by the anode, so there is a certain current flowing between photocathode and anode. An ammeter simultaneously supplies and measures the current that keeps the photocathode neutral with respect to ground. It is of the order of 0.1 pA for non-activated photocathodes and of the order of 1 nA or higher for activated photocathodes. The exact proportionality factor between photocurrent and quantum efficiency varies slightly in each measurement because the position of the photocathode is only determined to within about 1 mm, the luminous flux of the UV LED can vary slightly, and the irradiance on the photocathode is only optimised to its maximum to achieve a good SNR.

QE measurement position

To actually determine the QE of the photocathode, its sensitivity must be compared with a calibrated photodiode at different wavelengths.

The light source for the QE measurements is a deuterium lamp². It has a continuous spectrum between 160 nm to 400 nm, with a maximum (plateau) between 200 nm to 230 nm. The light output of the lamp is very stable after

²Data sheets: <https://qd-europe.com/de/en/product/deuterium-light-sources>, [18.03.2021]

reaching its constant operating temperature. To shorten this time and prevent overheating in the closed nitrogen box in which the lamp is positioned, a fan is mounted on the lamp housing. Due to this fan and a defined nitrogen atmosphere and thus less ozone formation, the warm-up time is reduced from approx. 120 min (see Hermanutz (2015)) to only 30 min. The measurement error is then less than 1 % (see Fig. 3.3). The next step is to project the arc of this lamp onto the entrance slit of a monochromator. Since mostly nitrogen is present in the nitrogen box, but also residual oxygen and ozone, the biggest effect is that the SNR is higher at the oxygen-cut off at 186 nm compared to measurements without nitrogen.

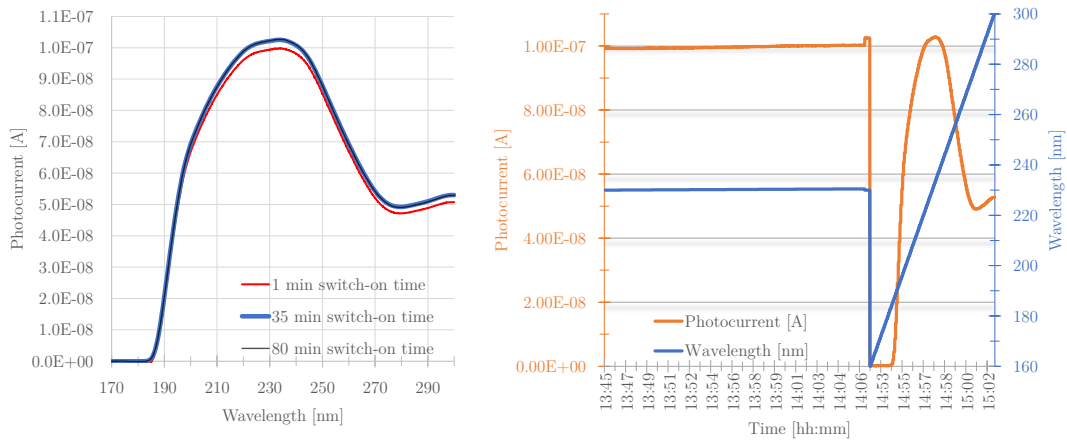


Fig. 3.3: *Left:* Three consecutive measurements of the lamp spectrum between 170 nm to 300 nm. During the warm-up time (30 min) the intensity of the lamp is slightly lower (red line). The measurements after the lamp has warmed-up for 35 min and 80 min are the same within the measurement tolerances. *Right:* Photocurrent over time (orange line) during deuterium lamp warm-up from 13:45 to 14:52 (4020 s) followed by a calibration measurement. The blue line is the wavelength of the light (at each time point) with which the Si-photodiode is exposed at any given time. During the measurement, it is kept constant at 230 nm to make only the deviations due to lamp fluctuations visible. Due to the cooling fan and less ozone formation as a result of the nitrogen atmosphere in the lamp, it is almost constant after only a few minutes, with a slope of less than +3 % per hour in the first hour. Since the calibration and photocathode measurements are only 20 min apart, the error after a warm up time of 30 min is less than 1 %.

The monochromator – assuming appropriate calibration – selects a specific wavelength from the continuous lamp spectrum (between the oxygen cut-off at 186 nm to 400 nm) and outputs a parallel parallel beam of monochromatic light using another lens. Further details on the calibration of the setup can be found in Hermanutz (2015). For the measurement of sealed diode bodies, instead of the focussing lens a sample holder with the sealed diode body and a calibrated photodiode is mounted behind the exit slit of the monochromator.

The photodiodes used were calibrated Si photodiodes originally calibrated by NIST in January 2011 from 51.9 nm to 253.7 nm. This yielded two problems. On the one hand, the magnitude of change in sensitivity is measured by NIST to be less than 3 % per year, within about eight years this means the variations due to impurities and changes in the properties of the Si photodiode material can be as high as 20 %. On the other hand, for GaN photocathodes, the uncalibrated wavelength range between 250 to 400 nm is also very interesting. Therefore, the Si-photodiodes were recalibrated by the “Physikalisch-Technische Bundesanstalt” (PTB) in the wavelength range between 100 nm to 400 nm. When comparing the results (see Fig. 3.4), almost no deviations occurred in the most interesting wavelength range between 150 nm to 250 nm. Interestingly, before the PTB calibration, only the lower limit of the QE between 254 to 300 nm could be extrapolated, with deviations from the later determined value of up to 50 %. Since the extrapolation underestimated the QE of the Si photodiode, it also underestimated the QE of the photocathode in this wavelength range for measurements before December 2019.

From a measurement of the photocurrent through the Si-photodiode due to its irradiation with monochromatic light of a certain wavelength, the number of photons per second reaching the Si-photodiode can be determined based on the calibration data. Wavelengths the monochromator can choose but were not measured by PTB were derived with a interpolation (see Fig. A.1). The light beam quantified in this way is directed into the Cathode Vessel to the QE measurement position (see Fig. 3.2). Transmittance losses on the quartz entrance window and substrate are considered, and can be accurately measured, but other loss mechanisms are defined to be negligible. The absolute QE measurements are therefore (slightly) lower limits.

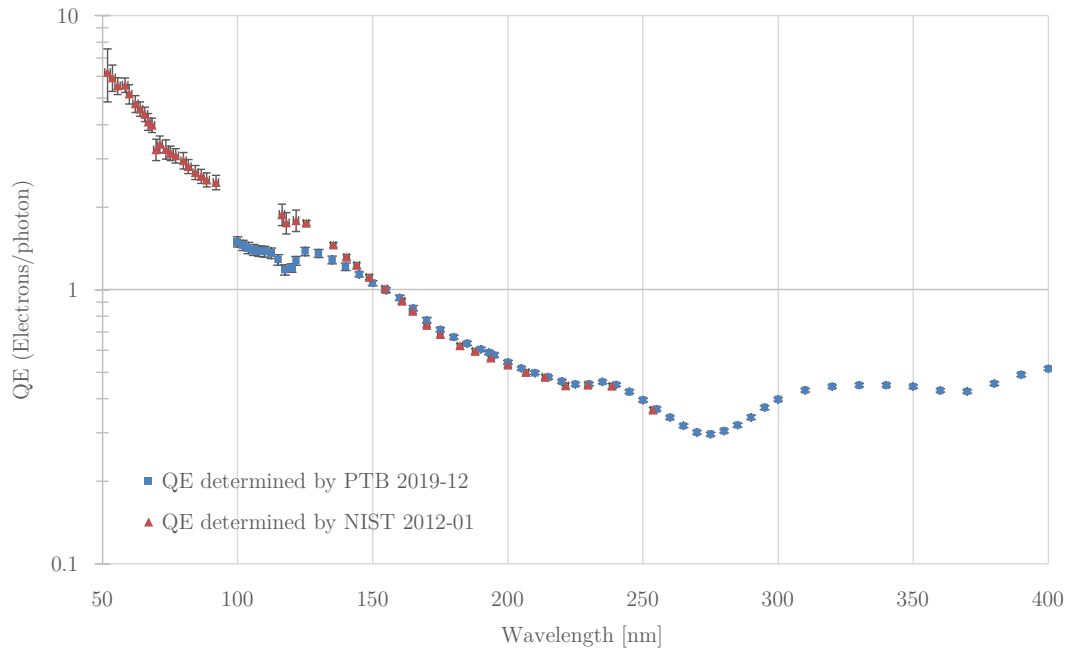


Fig. 3.4: NIST calibration compared to PTB calibration of Si-photodiode AXUV-100G, 09-911. Error bars as given in the calibration data, in the wavelength range below 150 nm the errors are very small

Transfer position and sealing position

After preparation and characterization of a batch of samples, the most promising ones can be used for sealing tests or eventually as window with photocathode for a sealed detector. In the “transfer position”, the substrate can be picked up with a specially designed transportation device, the “transfer fork” (see Fig. 3.5).

As shown in Fig. 3.5, after the cathode transfer, the detector window is positioned near the sealing position for further processing. On the sealing position a holder for detector bodies is installed. It has several features:

- To contact the detector body electrically, and e.g. apply a voltage between cathode and anode, or to measure the photocurrent.
- A heating has a variety of purposes. Primarily for melting the indium alloy in the sealing ring (see also Chap. 1.3), for heating the detector window sealing areas during the sealing process, for activating a getter in the detector body or for outgassing MCPs.

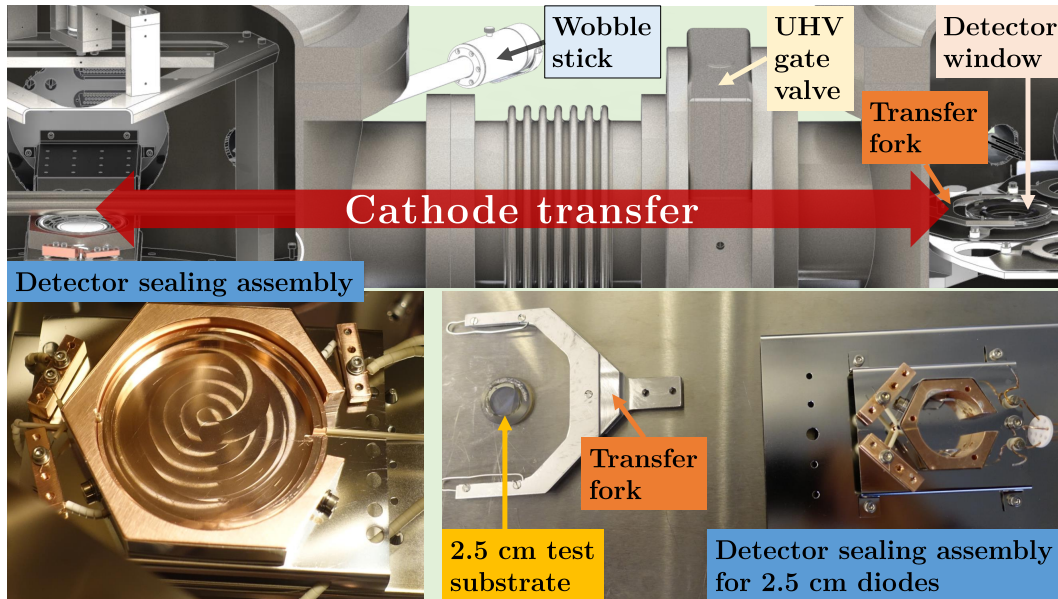


Fig. 3.5: *Top:* To transfer substrates with photocathodes from the Cathode Vessel to the Detector Vessel, the UHV valve between the two vessels must first be opened. The transfer fork is then used to lift the window from the photocathode transfer position. *Bottom left:* Detector sealing assembly in the Detector Vessel. *Bottom right:* Transfer fork for the detector window. A 2.5 cm sample is placed in its centre for size comparison. The detector sealing assembly for the 2.5 cm diodes is fully functional and can be reinstalled in the Detector Vessel if necessary

- The sealing fork and the entire sealing position can be varied in height, e.g. to place the detector window on the detector body.
- A wobble stick with interchangeable tip can be used for precise manipulations inside the Detector Vessel.
- The detector chamber is equipped with the same feedthroughs as the test stand which is used to obtain photon data and optimize the programmable detector electronics (see Hanke (2018)). This is particularly useful for an open detector, since the detector can be characterized while still in the detector chamber and the decrease in its performance (if any) can be determined due to the necessary handling in an inert gas atmosphere for further assembly steps.

3.1.2 Residual gas measurements

In Chap. 2.2.5, the degradation and longevity of caesium-activated photocathodes is discussed. It is found to depend mainly on the partial pressures of oxygen ($p[\text{O}_2]$), water ($p[\text{H}_2\text{O}]$) and caesium ($p[\text{Cs}]$) in the vacuum system in which the photocathode is processed. When activating GaN photocathodes, $p[\text{Te}]$ should also be very low. The total pressure in both UHV vessels is continuously monitored, but is only a rough indication of the partial pressures of interest. To analyse the partial pressures of the residual gases in the vessel, both vessels are equipped with a *Metek Dycor LC-D Residual Gas Analyser*³. A comprehensive description of this topic with its many possible applications can be found in (Dawson, 1976). In short, particles (atoms and molecules) are ionized (electron impact ionization) in a measurement chamber with an opening to the vacuum chamber and accelerated in an electric field. A quadrupole mass filter selects from all charged particles only those that have a certain ratio of total mass (atomic mass unit, AMU) to ionisation level (charge). For the measurement of the ion current of the particles with a specific AMU per charge (channel) two types of detectors can be used in our setup:

- A Faraday Cup for partial pressures between 10^{-4} mbar and 10^{-11} mbar. For pressures below 10^{-11} mbar a long dwell time (duration of each measurement) would be needed to achieve a sufficiently good SNR.
- For lower pressure measurements an electron multiplier, two MCPs in chevron configuration, can be used as detector. At high pressure they oversaturate and lose gain quickly (see Sect. 1.2.2). Therefore they are applicable for pressures of up to a few 10^{-9} mbar, for higher pressures the Faraday Cup achieves a good SNR in a reasonable dwell time anyway. The lower detection limit is as low as 5×10^{-14} mbar. As can be seen in Fig. 3.7, in our setup already at a few 10^{-12} mbar the error bars get bigger, presumably due to pressure fluctuations in the vacuum vessel over time.

Calibration and interpretation of the data is required to determine the partial pressures from the measured ion currents. In general, the interpretation is

³User Manual with detailed information available under <https://www.ametekpi.com/products/brands/dycor/lc-d-series-rga> [18.03.2021]

not trivial because, for example, molecules can fragment into smaller molecules during the electron impact ionization, and the number of doubly charged ions must be examined for each experimental setup and channel. In our case, it is only necessary to determine the photocathode growth requirements; for this purpose only upper limits for individual channels need to be defined.

The fraction of doubly ionized molecules can be estimated with the measurement for channel eight. For other channels, this fraction may vary slightly. For channel eight, a partial pressure of 2.93×10^{-13} mbar is obtained after calibration (see Tab. A.1 in the appendix), the calibration method is presented in the Appendix A. The following molecules contribute to the measured ion current: singly charged $^4\text{He}_2$, doubly charged oxygen and doubly charged water. The latter must also have been fragmented, and lost at least one hydrogen atom to be measured in channel eight. Interestingly, $p[^{16}\text{O}]$ is at 5.77×10^{-11} mbar, hence doubly charged oxygen contributes at most 0.5% to the measured ion current. The real fraction must be even smaller, since $p[\text{OH}]$ is measured to be 1.02×10^{-10} mbar and also helium contributes to this channel. This means the fraction of doubly charged ions must be less than about 1%, making their contribution negligible.

Fragmentation effects are slightly higher, as indicated by the measurement of $p[^1\text{H}_1]$. In the ion current measurements, the main source of atomic hydrogen should be fragmented water and molecular hydrogen molecules. The ratio of $p[^1\text{H}_1]$ to the sum of $p[\text{H}_2]$ and $p[\text{H}_2\text{O}]$ is about 0.05, i.e. the actual partial pressure of water in the vessel is a few percent higher than the partial pressure of channel 18 as determined by the mass spectrometer. Consequently, in our case, it is best to define the partial pressures required for photocathode growth in our vessels only by the calibrated measurements of the corresponding channel of the mass spectrometer. This allows for one less calibration step, which would only be necessary anyway if an accurate comparison with other vacuum systems is required.

With the partial pressures presented in Fig. 3.7, good results were obtained for the preparation of caesium telluride photocathodes, as discussed in Sect. 3.4. They are therefore defined as the corresponding upper limit for the partial pressure and can be achieved without baking out the vacuum system under the heating tent.

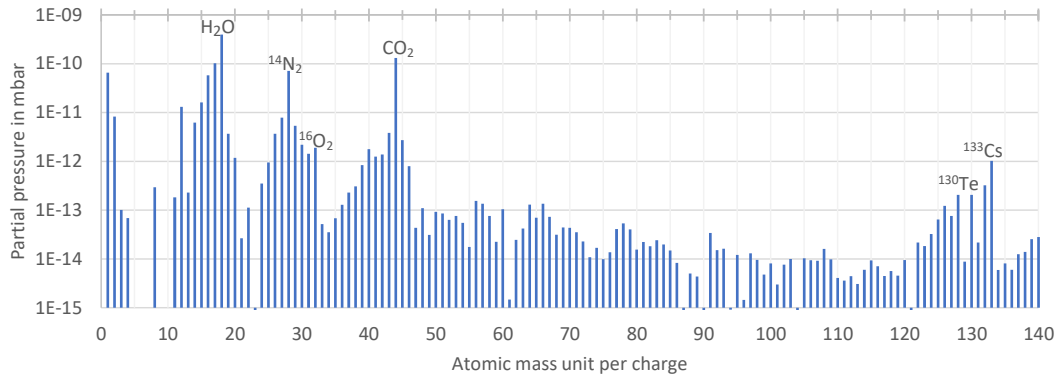


Fig. 3.6: Partial pressure in mbar (calibration with the total pressure of 9.17×10^{-10} mbar measured by the ion pump) over the AMU per charge. Some interesting molecules are labelled, a table with all values is presented in Tab. A.1. Heating out the vessels to about 150°C could significantly lower $p[\text{H}_2\text{O}]$, but is avoided because $p[\text{Te}]$ would also increase during this process, leading to the contamination of the GaN samples

The activation of GaN needs further improvements, and the next step is to minimize the influence of tellurium and its compounds in the Cathode Vessel. The total pressure is probably low enough, because Norton et al. (2003) achieved high QE in a vacuum chamber with a pressure of less than 10^{-9} Torr (1.3×10^{-9} mbar). In order to achieve a presumably much lower $p[\text{Te}]$ in our vacuum system, all tellurium-contaminated parts will be replaced during the next maintenance of the Cathode Vessel and the entire vacuum system will be baked out before inserting the GaN samples.

Besides the partial pressure measurements, the mass spectrometer is also

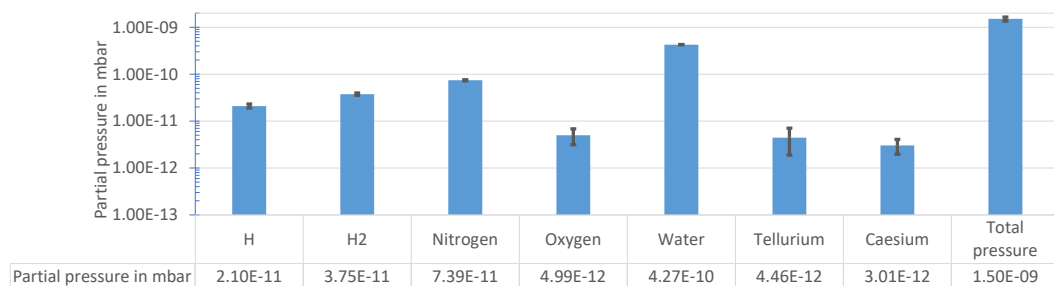


Fig. 3.7: Partial pressures of molecules that have the greatest effect on the growth or activation of the photocathode. For details on the calibration of the data see Appendix A, Tab. A.1

used for helium leak tests after opening a flange of the vacuum vessels. If the partial pressure of helium in the vacuum chamber increases after helium has been blown onto the sealing ring of a flange from the outside, this indicates a leak.

3.1.3 Nitrogen box

The nitrogen box is a light- and air-tight housing for the components used in the absolute quantum efficiency measurements described in Sect. 3.1.1. A previous version of the nitrogen box is detailed in Hermanutz (2015). The light density is needed for the calibration measurements because the Si photodiode is not solar-blind and the dark current would change during a measurement if the amount of light in the laboratory is not constant.

Since a powerful UV lamp is required for these measurements, a large amount of ozone is formed when operated in air within the warm-up time of the lamp and the measurements. The ozone is exhausted from the laboratory with a strong vent, to prevent a noxious amount of ozone from being present in the laboratory. Nevertheless, the ozone concentration in the UV lamp and in the monochromator increases during operation in air and affects the measurement because the absorption coefficient of ozone differs from that of air. It is therefore advantageous to flood the areas of the beam path exposed to air (and especially oxygen) with nitrogen. For that reason, five minutes before the start of the lamp warm-up time, the box is filled with nitrogen. The measurements shown in Fig. 3.3 demonstrate the capabilities of the well defined atmosphere in the box and the reproducible results that can be obtained. Another advantage is that the ozone concentration in the laboratory is also drastically reduced to the point where it is imperceptible.

For further optimizations of the box, an oxygen sensor will be installed in the box. If necessary, the box must first be sealed even better. This would allow the box to maintain a nearly complete nitrogen atmosphere for weeks, reducing the amount of nitrogen needed for each measurement.

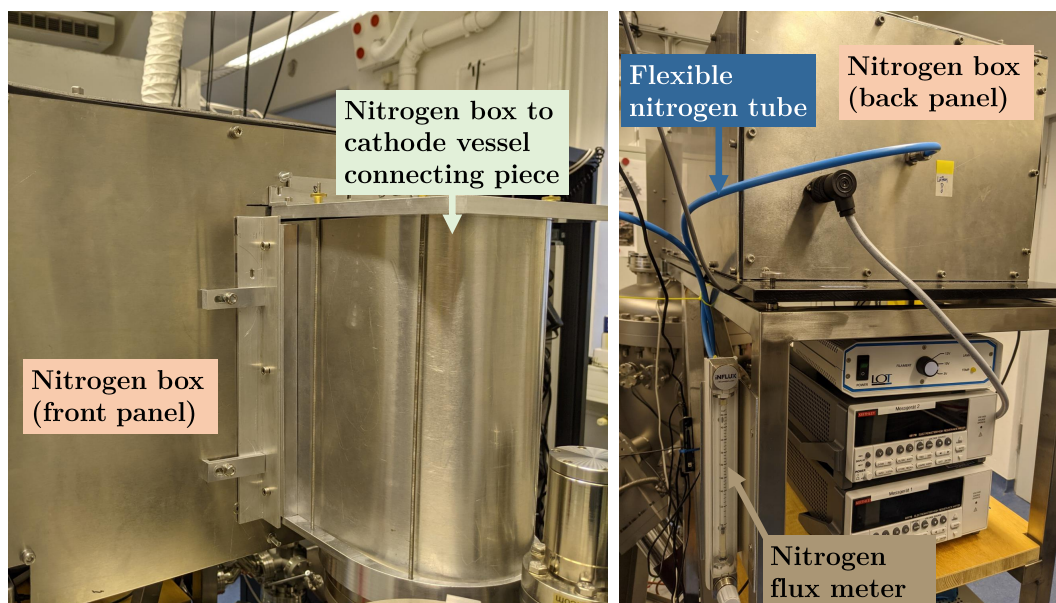


Fig. 3.8: The most important parts to obtain a defined atmosphere in the current version of the nitrogen box. The connecting piece between nitrogen box and Cathode Vessel is very easy to attach and detach. A flux meter is used to adjust the nitrogen flux. During measurements, a flux of one liter of nitrogen per minute inserted directly into the deuterium lamp housing prevents most of the ozone formation

3.2 Sealed diode bodies

In Chap. 1.3 it is shown that low surface tensions between the sealing areas and a liquid sealant are required for good wetting and thus a strong bond between the detector window and detector body. Also shown were the experiments with a drop shape analyser conducted in collaboration with a cooperating partner to determine such combinations of materials. The sealing experiments with the appropriately coated diode bodies and the measurement of the stability of two successfully sealed diode bodies are presented in the following section.

3.2.1 Sealing process

The sealing process is performed at the sealing position described in Sect. 3.1.1.

A eutectic⁴ indium-bismuth alloy is used as the sealing solder. The alloy

⁴An alloy is called eutectic if the mass fraction of the individual elements of this alloy is selected such that the alloy has the lowest possible melting point.

is prepared⁵ and placed in the sealing ring of the sealing area. The detector or diode body is then mounted in the sealing position, see Fig. 3.5, and the whole chamber is evacuated to a pressure below 10^{-9} mbar. The diode body is heated, causing the ring of alloy material to melt and slowly spread over the entire sealing area due to the small surface tensions, see Fig. 3.9.

The photocurrent of a transferred substrate (see Fig. 3.5) can be measured in the sealing setup before the sealing process, after the sealing process and during venting of the Detector Vessel. If a photocurrent is measured after the detector chamber is completely vented, this indicates that the diode is airtight. It is then taken out of the UHV system and installed behind the exit slit of the monochromator to check for its long-term stability (see Sect. 3.1.1 or Hermanutz (2015)).

3.2.2 Change in photocathode properties due to sealing

The sealing area near the caesium containing photocathode is heated to temperatures of up to 370°C. One problem to be solved is whether and to what extent caesium is evaporated or sublimated throughout the process. Caesium telluride is relatively stable at these temperatures, and there is no clearly visible decrease in photocurrent during sealing. The chemical bonding of the Cs_2Te crystal is therefore in principle high enough to withstand the sealing temperatures. Details on the temperature stability of different caesium telluride compounds are presented in Hermanutz (2015).

However, as long as the photocathode surface is exposed to a UHV, its QE will decrease significantly within hours to weeks, as already discussed in Chap. 2.2.5. This will continue until, after sealing, $p[\text{Cs}]$ in the diode body is high enough to reach an equilibrium between caesium loss and gain, or only strongly bound caesium atoms remain on or in the photocathode. For example, in Fig. 3.10, the time between the activation of the photocathode and sealing of the diode body is relatively long, leading to a reduction in the QE. However, the reduced QE was irrelevant for this test, since the main purpose of the test is to optimize the sealing of a diode body, regardless of how long individual process steps initially take. Thus, a higher QE would only have the advantage

⁵Details how to etch indium and remove surface oxidation can be found in literature, e.g. <http://indiumblog.com/entry.php?id=1048&lang=DE> [18.03.2021]

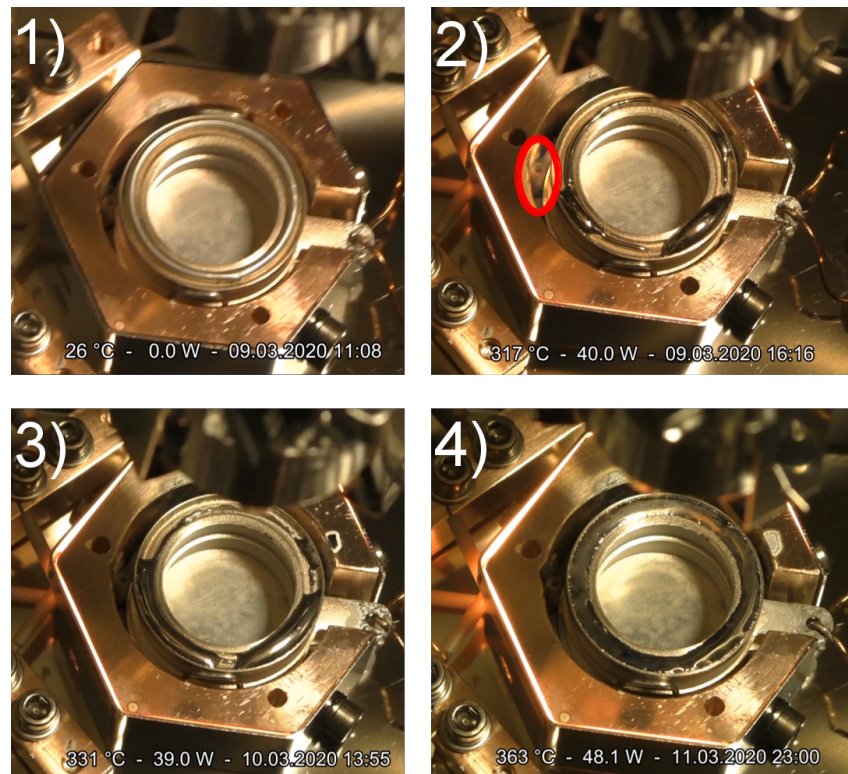


Fig. 3.9: Diode body for sealing tests of 2.50 cm diameter samples in vacuum with molten indium alloy. Measurements of a temperature sensor next to the diode body are used for calibration. **1)**: Diode body shortly before the heater is switched on. **2)**: The diode body with indium ring is slowly heated, the temperature sensor at the position marked in red measures 317°C, the actual temperature of the sealing surface is lower because the materials have a low heat conduction coefficient. The molten alloy is slightly shinier than in the solid state, which makes the phase change easily visible. Since the diode body is not horizontal (level) enough, a large indium droplet initially forms on one side. **3)**: After slight levelling, the alloy begins to spread over the sealing surface. **4)**: With a further increase in temperature and several hours later (see time stamp), the indium spreads evenly

of a better SNR in measurements, but also the contamination of the Detector Vessel with caesium from the Cathode Vessel would have been higher. In the case of detectors used for imaging, the stability of the photocathode should be high and the time period it is exposed to UHV should be kept low.

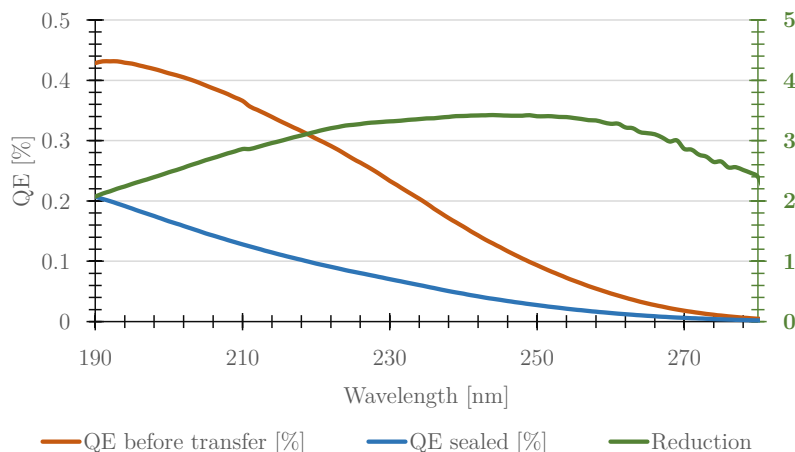


Fig. 3.10: QE of photocathode CsTe-C2 before and after sealing. The reduction factor plotted in green has a value of about 2 at 190 nm and increases to a value of about 3.4 between 240 to 260 nm. This indicates a loss of Cs. Caesium telluride can form different compounds that differ in the abundance of Cs compared to Te. For example Cs_5Te_2 has its maximum QE at lower energies compared to Cs_2Te and has a higher vapour pressure at the sealing temperatures. As the QE went to higher energies, this means, there was a loss in Cs

In the case of caesium-activated GaN photocathodes, the caesium is not bound in the bulk of the photocathode, but is a thin layer on its surface. Thus, desorption of caesium or chemical reactions, e.g. with residual oxygen in the UHV vessel, can occur with this layer at room temperature. It is an expected behaviour reported by Stock et al. (2005), for an illustration see the activation measurements in Sect. 3.3.2.

Qualitative measurements just before and after sealing show that there is no significant change in the behaviour of the GaN photocathode at the given temperature and duration of the sealing process in the UHV system. Quantitative tests comparing QE at the measurement position in the cathode container and at the monochromator, as shown in Fig. 3.10 for a CsTe photocathode,

would also require a sealed diode body with GaN photocathode. This has not been achieved so far, presumably because the wetting properties of the sealing surfaces were altered during the Ga-rich GaN growth. A revised manufacturing and metallisation process addresses this problem for future samples.

3.2.3 Change in photocathode properties after sealing

After the sealing process, the sealing assembly is allowed to cool down to room temperature, the Detector Vessel is vented and the photodiode is tested for a response when illuminated with UV light. If a clear response is measured, the diode body is placed in a holder with an integrated calibrated NIST photodiode and attached to the monochromator. The measurements are similar to those at the QE measurement position and to a large extent use the same and similar test equipment. Also the measurements are expected to be very reproducible, since the same measures are taken as in the measurements depicted in Fig. 3.3.

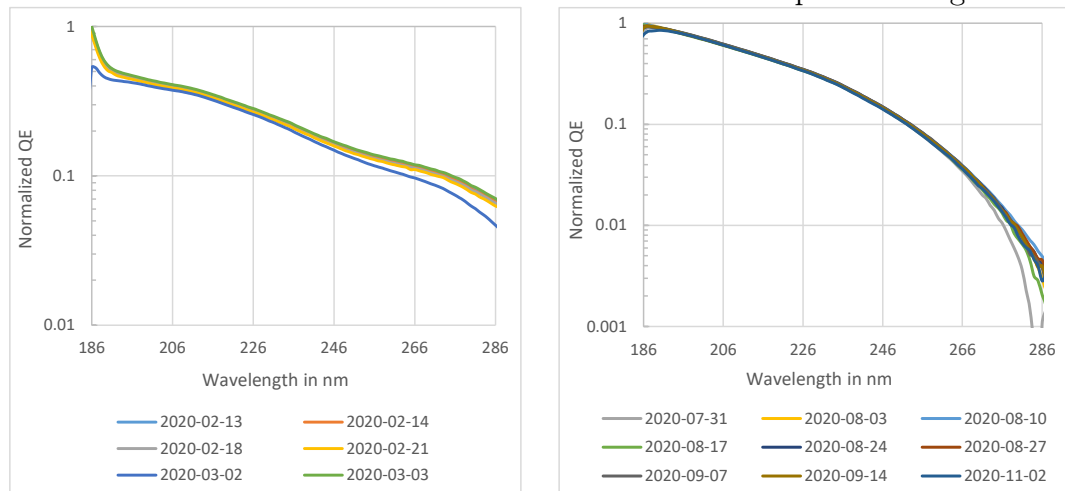


Fig. 3.11: QE measurements versus the wavelength on two sealed diode bodies with caesium telluride photocathode over a period of two weeks (left) and several months (right). The outlier on 2020-03-02 is measured after some tests in a climate chamber without significant deviation when measured again on the following day. The axis is normalized to emphasize that the test is only about the stability of the photocathode, not the absolute value of the QE

Figure 3.11 (also presented in Conti et al. (2020)) shows that the quantum efficiency of two sealed diode bodies with caesium telluride photocathode did not change at all within weeks and even months, with the only visible deviations due to a poorer SNR near the cut-offs at 186 nm and of the photocathode.

This behaviour was to be expected; Siegmund et al. (2003) also reported that there is no decrease in QE after sealing.

3.3 GaN photocathodes – measurements

3.3.1 Preparation of suitable (0 0 1) magnesium fluoride substrates for GaN growth

In Chap. 1.2.1, it is pointed out that (001) MgF_2 is a very promising substrate for GaN in semi-transparent mode due to its small cut-off wavelength and low crystal lattice mismatch to cubic GaN. Despite the 30 nm lower cut-off, sapphire substrates are most commonly used in the literature for GaN growth because good results are obtained more easily compared to MgF_2 . In the following, the variety of optimizations and measures taken to find optimal parameter sets for GaN on MgF_2 are presented.

Substrate types

The substrates chosen for the parameter tests are laser polished (see Chap. 1.2.1) with cleavage surface (see Fig. 2.1) (001) and (110). AFM measurements⁶ of these samples showed polishing scratches down to a depth of 20 nm. Gallium accumulates in these scratches, slightly worsening GaN growth. Nevertheless, for the initial tests, these laser polished samples are well suited because the influence of GaN growth conditions (Ga wetting, growth temperature) have a much larger impact on the properties of the resulting GaN layer. If no further sample parameters are mentioned, those were used as “standard substrate”. For finer optimizations, epi-ready substrates with a surface roughness in the order of a few angstroms and generally better surface quality are chosen.

Cleaning

The role of substrate cleanliness, which must be as high as possible to achieve good results with GaN, cannot be overstated. A comprehensive study of GaN

⁶Atomic force microscope (AFM) measurements were performed by K. Meyer from the research group of Prof. Dr. Daniel M. Schaadt at the TU Clausthal

cleaning can be found in Machuca et al. (2002), and the substrate cleaning methods possible with our laboratory setup are presented in Chap. 1.2.1. For some MgF_2 substrates, cleaning could make them dirtier, for example, if they were properly cleaned by the manufacturer, shipped in a sealed bag, and did not have a long storage time. In this case, only dust is blown off the samples with a nitrogen gun before each process step. All other samples were properly cleaned.

Metallisation

The next preparation step for the “standard samples” is the metallisation of the substrates with 30 nm of NiCr^7 and Au respectively. In order to investigate the influence of the metallization layer on photocathode growth, samples were prepared on which corresponding test strips were vapour-deposited. Two of these samples are shown in Fig. 3.12.

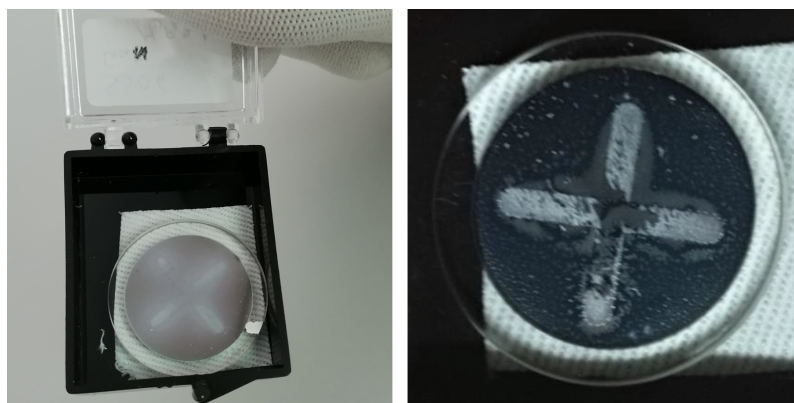


Fig. 3.12: Metallization layer in cross form on two substrates with overlying GaN layer. On the right side, the Ga-flow was too high and large gallium droplets formed. *Credit GaN growth: Kevin Meyer, TU Clausthal*

GaN growth

The GaN films were grown and analysed by K. Meyer in a cooperation with the research group of Prof. Dr. D. M. Schaadt at the TU Clausthal. Details on the growth of GaN films on MgF_2 samples and the laboratory setup at the TU

⁷NiCr was chosen because it bonds very well to the substrates, but pure Ni should be used if the samples need to be annealed.

Clausthal can be found in Conti et al. (2020), Meyer et al. (2020a) and Meyer et al. (2020b). In short, plasma assisted molecular beam epitaxy (PA-MBE) with a pressure as low as 2.8×10^{-11} mbar is used to grow predominantly cubic GaN under Ga-rich conditions in the most promising temperature range (450°C to 700°C). The high substrate temperature during the growth of GaN films is needed to increase the mobility of Ga atoms. A heater irradiates the sample with infrared light. Since this light is absorbed more efficiently by the metallization layer, it reaches higher temperatures compared to the substrate and causes the gallium to preferentially move to these hotter areas. To address this, two countermeasures are implemented. First, the GaN growth is performed less Ga-rich. Second, in the preparation of sealed diodes (not “standard samples”), the metallisation is performed after the GaN growth to prevent Ga droplets on the sealing area from deteriorating its sealing properties. In this case it is also possible to anneal the sample, i.e. as described by Qiao et al. (2000), the sample is heated in an oxygen atmosphere or air, which allows a Au/Ni film (thickness 20 nm each) to form a good ohmic contact with p-doped GaN. However, for “standard samples”, the metallization was not done after GaN growth because during the metallization process, the metal vapour could contaminate the GaN film and it is also exposed to contaminating air (and dust) for at least another hour.

Loading in UHV vessel and bake-out

The samples are then placed in the Cathode Vessel. The final cleaning step is an in-situ bake-out of the samples. Temperatures as low as 250°C are sufficient to remove most of the surface water. For thermal desorption of last monolayers of e.g. carbon and oxygen, very high temperatures of 700°C would be optimal. However, the GaN growth temperature is 450°C to 700°C and the bake-out temperature should be lower than the growth temperature to avoid changing the properties of the GaN layer. Therefore, only the surface water can be removed by bake-out of the samples in vacuum at about 250°C for 24 hours⁸. This also reduces the chance of breaking the MgF₂ samples, which would not only result in loss of the sample, but could even damage components.

⁸This substrate temperature is also about the limit of the current filament heating in the Cathode Vessel.

3.3.2 Activation and QE measurements of undoped GaN films

The next process step with the substrates now as clean as possible is the surface activation. The physics behind the activation process is described in detail in Chap. 2.1 et seq.

In our publication by Meyer et al. (2020a), it is shown that GaN films on MgF₂ can vary strongly in homogeneity, grain size or surface roughness depending on the growth parameters. From this variety of GaN films, the task is to determine which of these films are actually best suited to achieve high QE over the entire image area and good adhesion of the film to MgF₂ even under temperature fluctuations. Tab. 3.1 provides an overview on the undoped GaN samples. All samples have a GaN film thickness of 100 nm.

Sample	Growth temp.	Substrate	Comment
S008	450°C	(0 0 1) MgF ₂	0.2 % QE
S009	450°C	(1 1 0) MgF ₂	0.4 % QE
S010	525°C	(0 0 1) MgF ₂	No electric contact
S011	600°C	(0 0 1) MgF ₂	Highest QE, 0.6 %
S012	650°C	(0 0 1) MgF ₂	0.2 % QE
S013	700°C	(0 0 1) MgF ₂	0.3 % QE

Tab. 3.1: Growth parameters of samples S008–S013

Influence of the crystal orientation of the substrate

For samples S008 and S009, the influence of crystal orientation is investigated. Both samples were grown at a growth temperature⁹ of only 450°C (see Tab. 3.1). All other GaN-growth parameters were also the same.

Both samples yielded relatively good first results upon activation. When irradiated with light from a UV LED, relative photocurrents (uncalibrated, $\pm 20\%$) of 1.2×10^{-9} A for S008 and 2.5×10^{-9} A for S009 were measured (see Fig. 3.14 and Fig. 3.15). As intended, the dark current is constantly about

⁹Growth temperature refers to the heater temperature during growth. The substrate temperature is slightly less (10–20 K)

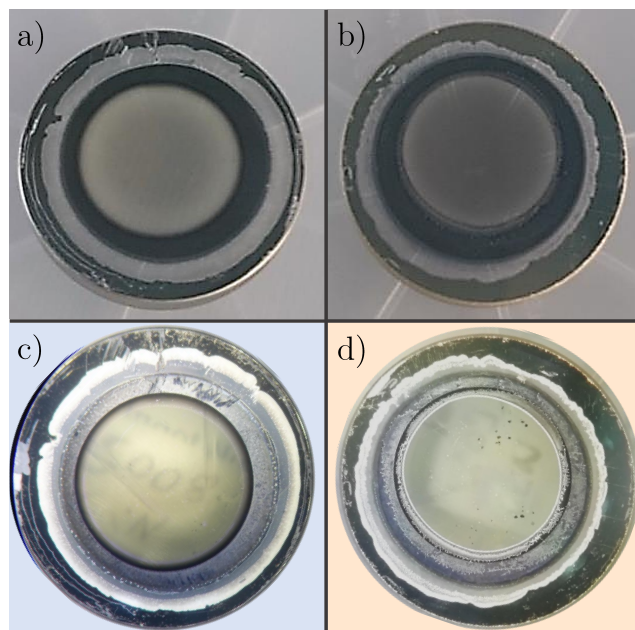


Fig. 3.13: **a)** Sample S008 after GaN growth but before activation. The substrate is (0 0 1) MgF₂. **b)** Sample S009 before activation. The substrate is (1 1 0) MgF₂. All other growth parameters are the same as for sample S008. **c)** and **d)**: S008 and S009 after activation

zero (10^{-12} A) throughout the measurements, indicating good grounding. The photocurrent of the initially unactivated photocathode is only slightly higher than the dark current. During activation, Cs is deposited at a relatively low rate, such that $0.1 \text{ \AA}/\text{s}$ are measured with an oscillating quartz crystal monitor. The film thickness of caesium on the crystal quartz is also much higher than on the sample because the substrate is hotter and has a greater distance to the dispenser. The Cs flow is stopped as soon as a plateau is reached by reducing the dispenser's heating current sufficiently within a few minutes. A still faster reduction could damage the Cs dispenser.

The shutter duration was chosen to be relatively long, such that the photocathode is illuminated for only ten seconds at a time, then the UV light is blocked ten seconds (1:1 ratio). Accurate dark current measurements would have been possible with fewer closing times, the 1:1 ratio was chosen to avoid charging the activated GaN film. If the electrical contact between the GaN photocathode and the metallisation ring is limiting, it will charge when irradiated with UV light once it exceeds a certain QE. Put simply, more electrons

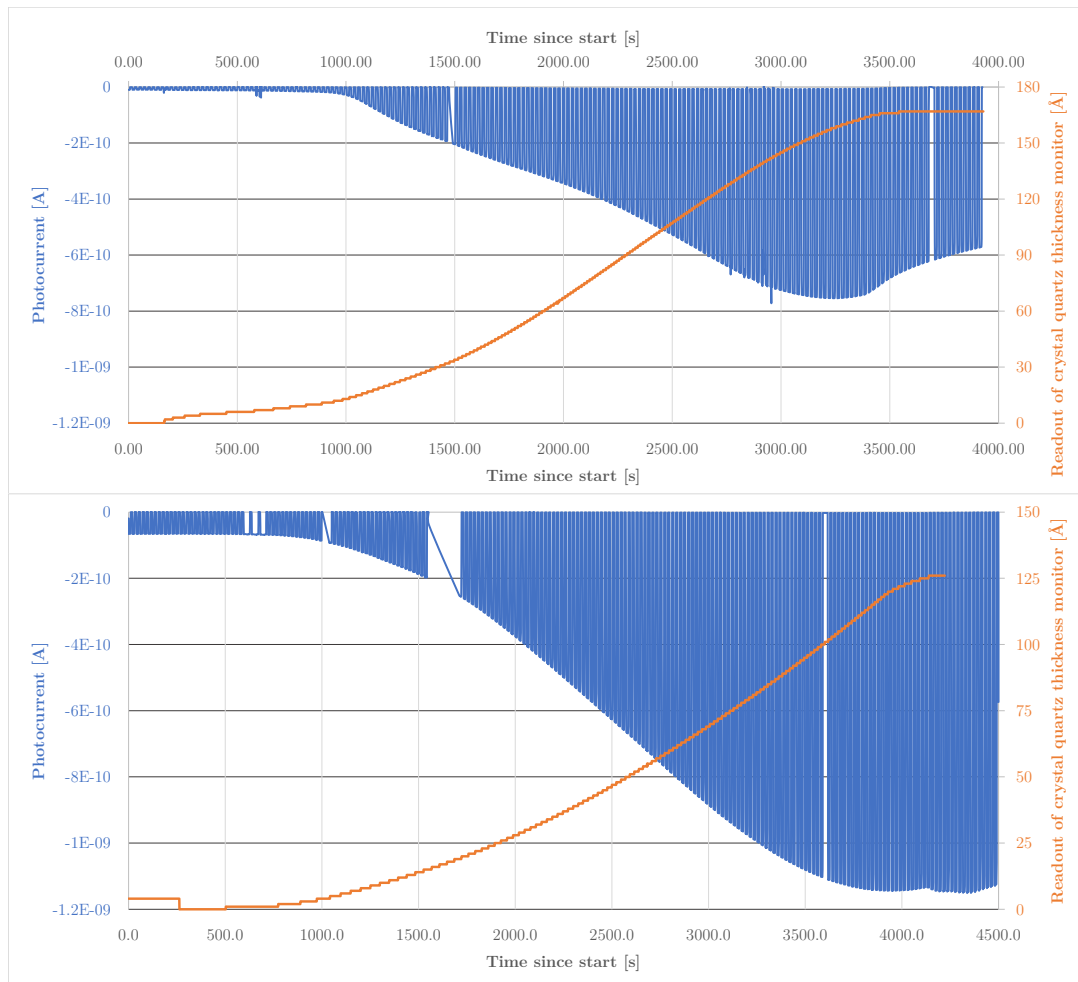


Fig. 3.14: *Top:* First activation of S008. *Bottom:* After the activation layer is exposed to UHV (about 1×10^{-9} mbar) and residual oxygen in the chamber for five days, the photocurrent drops to 6.5×10^{-11} A. When reactivated, about twice the photocurrent is achieved compared to the first activation (1.2×10^{-9} A), as expected for a Cs/O/Cs activation layer

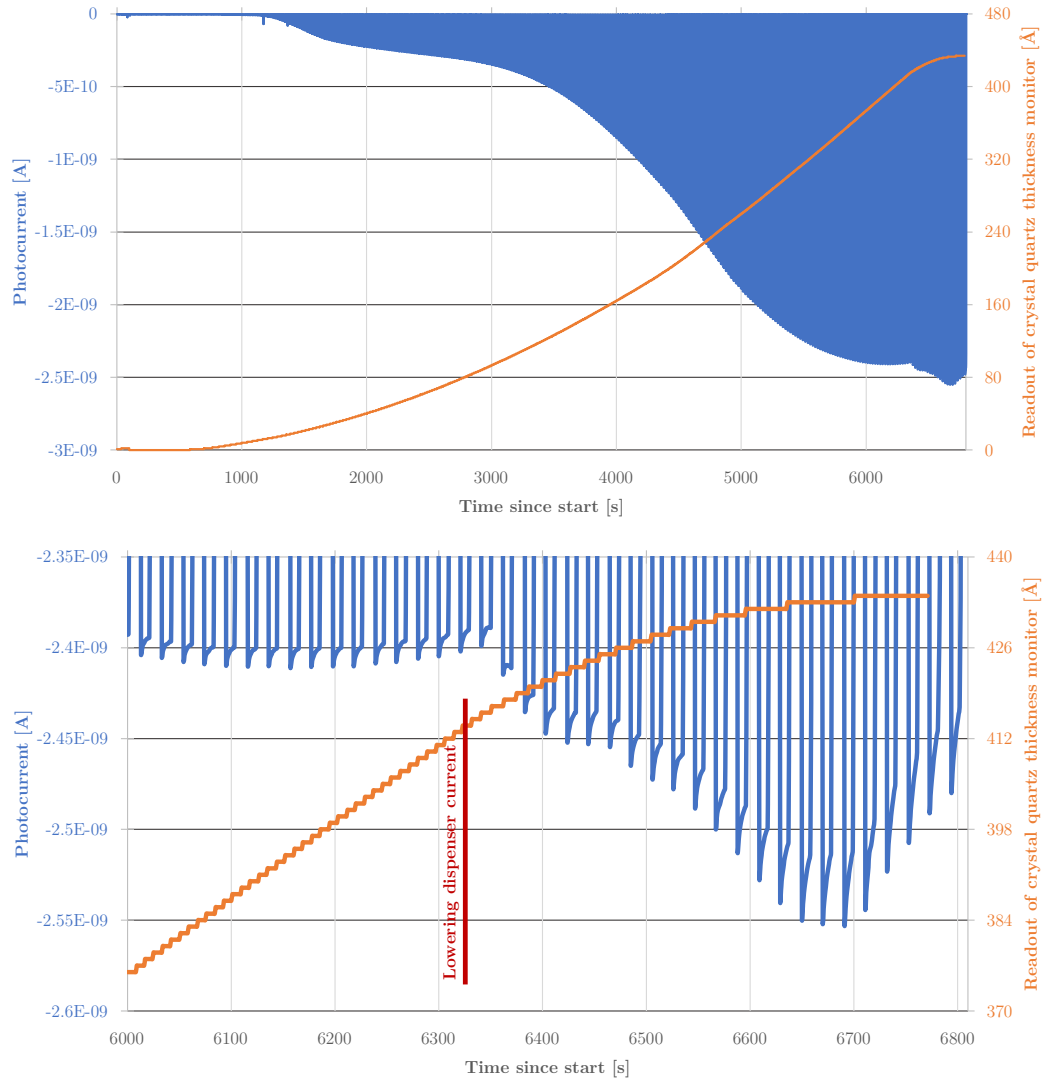


Fig. 3.15: *Top:* First activation of S009. *Bottom:* Only the last minutes of the activation measurement of S009. The comparatively high photocurrent and poor contact or conductivity of GaN leads to charging effects on the sample. The photocurrent is negative, with the shutter closed the sample is not illuminated and a dark current of approximately zero is measured

leave the photocathode than can be delivered through the contact. In this case, the photocathode becomes charged, resulting in an ever-increasing opposing electric field until the QE is again low enough to reach equilibrium. On the other hand, as long as the shutter is closed, the sample can discharge itself. If the shutter time is long enough, the internal QE of the photocathode can still be measured even if the QE drops as described above due to charging effects. The effect can be seen in the lower part of Fig. 3.15, showing that the photocurrent is highest at the first measurement point after the shutter is opened and then drops exponentially during illumination. For caesium telluride photocathodes, these charging effects occur when a compound of low conductivity caesium telluride is formed and increase again when a compound of higher conductivity forms. The case of GaN photocathodes differs because the properties of the GaN layer itself have already been defined during growth and only an activation layer is deposited on the top of the photocathode. Therefore, charging effects must be avoided primarily by growing GaN layers with low internal resistance and good ohmic contact to the metallisation layer.

For metallization, circular metallization layers are deposited on the sample edge, and the GaN layer is deposited on the inside of this circular ring (see Fig. 3.13). Gold is used to ensure a good contact with the contact pads of the vacuum system. However, much better contact can be achieved with Ni/Au contacts and annealing as described in Sect. 3.3.1. However, as also discussed in this section, other problems arise in making such a contact. It was assumed that by choosing long shutter times, for this first batch of GaN samples (S008–S013), the influence of the electrical contact should be small enough to actually still find the GaN films with the best properties. The QE should be about or slightly below 2% for the best sample¹⁰. In other words, for samples S008 to S013 it was avoided to get to the point where the contact to the metallisation ring is the limiting factor. If a too high internal QE of the photocathodes is achieved, one would only identify the sample with the best (not yet optimised) electrical contact and not necessarily the best GaN layer growth parameters.

¹⁰Norton et al. (2003) report 1.2–1.3% QE (at 254 nm) for 100 nm thick films of GaN without oxygen exposure (but p-doped). With an additional oxygen exposure and caesiation step, resulting in a Cs/O/Cs activation layer, the sample achieves a QE of 2.2%. Best results were obtained with ten times alternating Cs/O coatings, the QE in this case is 32%

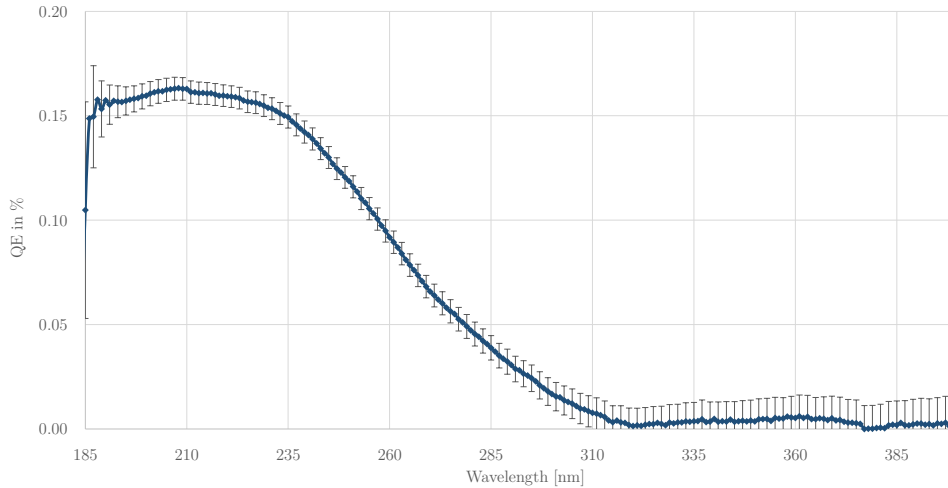


Fig. 3.16: QE of GaN test sample S008 with Cs/O/Cs activation film. Errors are estimated with the Gaussian error propagation law, taking into account the standard deviation of five individual measurements per measurement point and the calibration errors of the calibrated photodiode as shown in Fig. 3.4

Once a batch of samples has good ohmic contact between the GaN film and the metallization ring and sufficiently high conductivity (e.g. determined by four-point measurements), the QE can then be further optimised by p-doping and alternating Cs/O layers. This should increase the QE by a factor of 10 to 25.

For S008–S013, only one Cs/O/Cs activation layer could be applied because the resulting photocurrents were already limited by the electrical contact. For this one oxygen layer to form, the sample is simply exposed to the residual oxygen in the vessel, which is at $p[\text{O}_2] \approx 5 \times 10^{-12}$ mbar (see Sect. 3.1.2). Each sample is then reactivated after a few days. Of course, optimal results are obtained by actually flooding the vessel with oxygen after each caesiation until $p[\text{O}_2]$ is at about 5×10^{-8} mbar. This would not only allow reactivation after minutes, but also minimise the influence of other residual gases in the vessel on the highly reactive caesium film.

S008 achieved a QE of about 0.17%, S009 about 0.37% (@210 nm). The early low-energy drop observed in Fig. 3.16 indicates that the properties of the GaN film or the activation layer are suboptimal. For a good GaN film, one would expect the low energy cut-off to be much closer to 400 nm. Apparently, electrons excited by light with an energy slightly above the band gap of GaN

could not leave the photocathode. This could mean, for example, that:

- The effective electric field is not high enough to accelerate the electrons in the conduction band and to the anode.
- They lost their energy by scattering on lattice displacements or grain boundaries.
- A dirt layer between GaN and the activation layer only allows higher energetic electrons to pass.

Nevertheless, it is noteworthy that GaN could be grown and activated on both crystal orientations of the MgF_2 substrate and at only 450°C .

Influence of GaN growth temperatures

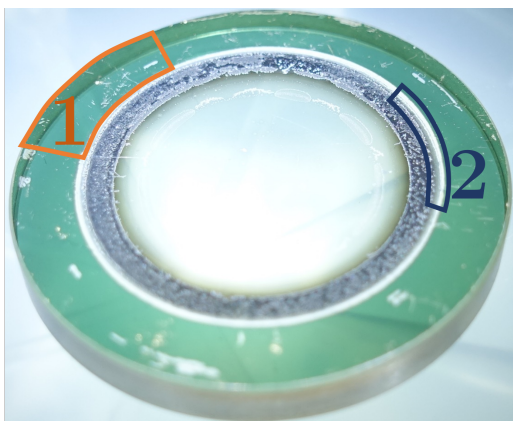


Fig. 3.17: Sample GaN-S010 after removal from the activation chamber. *Area 1*: Scratches or loss of the metallisation. *Area 2*: Transition region. It appears that there is a thin ring where neither GaN nor the metallization layer are present

Samples S010 to S013 are grown on (001) MgF_2 . Together with sample S008 they cover the whole spectrum of possible GaN growth temperatures on MgF_2 (see Tab. 3.1). The activation curves look similar to those of S008 and S009 (Fig. 3.14 and Fig. 3.15), except for S010. For sample S010, it was not possible to measure the light-dark pattern during activation, even after deposition of more than 100 \AA of Cs. It would have been possible to rotate the sample with the transfer fork to test if only poor contact with the sample holder caused this problem. When looking at Fig. 3.17 of S010 after removal from the vacuum chamber, several problems are apparent, indicating that a mere rotation would probably not have solved the problem. Caesium salts are clearly visible on the sample, indicating that indeed enough caesium was on the sample, i.e. the GaN film was activated. The layer thickness of the gold metallisation ring is too thin, as it appears green and has a relatively high transmittance. Due to

a defect in the electron beam evaporator used to apply the Ni/NiCr layers, it was obvious to use this sample to check how important a NiCr bonding layer is for the sample to work. One can clearly see the complete loss of metallization in some parts of the ring. Presumably, gold has been completely lost near the GaN film, but this also means that there is no longer any electrical contact.

As a result in the next batch of samples, always 30 nm of NiCr is electron beam deposited, and the thickness of the gold layer is increased (30 nm instead of 20 nm).

For sample S013, the electric contact is good enough to activate the GaN film, but strongly limits the QE of the photocathode, as shown in Fig. 3.18. If a sample has a poor contact, three countermeasures can be taken to still measure the QE reliably:

1. The irradiation could be reduced, for example, with an aperture between the lamp and the light source. As shown in Fig. 3.18, the dark current is on the order of 2×10^{-13} A, with a maximum of about 4×10^{-12} A. This means that the measurement points are already relatively close to the noise level, a further reduction should therefore be avoided.
2. Using the shutter to block the light, as already described in the paragraph above for the activation measurements. The photocurrent is measured with the shutter closed and with as many measurement points as possible during and after the opening of the shutter (the opening can take place within tenths of a second). The first measurement point should show a signal similar to the same photocathode with ohmic contact.
3. Adjust the monochromator so that it selects light that is subsequently completely absorbed by residual oxygen in the monochromator box. Thus, the sample is not illuminated at all for this period. By switching the monochromator to the wavelength of interest, the same effect is achieved as when using a shutter.

Thus, with a continuous measurement, a photocurrent of 2×10^{-12} A is measured at 195 nm for S010 (see Fig. 3.18 on the top left at 195 nm). With method three (see Fig. 3.18 on the top right) it can be shown that the QE can be higher by a factor of five for a short time or for weaker light sources. Thus, the

QE of S013 is about half the QE of S011, but at higher illumination it drops to 10 % QE of the QE of S011.

S011 is the sample which achieved the highest QE from the whole batch. The GaN film did not charge much, neither during activation nor during QE measurement. Due to already quite low caesium content in the dispenser, the QE is measured without reactivation. For a Mg-doped¹¹ GaN film with only one Cs-activation layer, the QE measured by Norton et al. (2003) on sapphire substrates is 1.2%. Therefore, the 0.57% QE on MgF₂ substrates (see Fig. 3.19) are at about half this level. With an ohmic contact between GaN and a Ni(/NiCr)/Au metallisation and graded p-doping with sufficiently high hole concentration, an even higher QE should be achievable, as the results from the following chapter demonstrate.

3.3.3 Activation and QE measurements of p-type GaN on magnesium fluoride

For samples S030 to S033, the influence of a better electrical contact and p-doping of the photocathode with magnesium is investigated. To optimize the contact, sufficiently thick NiCr/Au-films (30–50 nm/30 nm) were deposited for the metallisation ring for the samples. When heating the sample during the bakeout, residual oxygen on the sample and in the vessel should form an ohmic contact, as already described in Sect. 3.3.1. The charging effects are indeed much smaller for this batch of samples, as shown in Fig. 3.20. Except for the additional doping with Mg, the growth parameters are the same as those of sample S012, since the properties of the GaN layer are good in S012 and its QE is limited mainly by charging. Therefore, the QE of each of the samples S030–S033 is compared with the QE of sample S012. Again, the primary goal for this sample batch was not to achieve the highest possible QE, but to determine the QE dependence on the Mg-effusion cell temperature during GaN growth.

The effects of the p-doping on the activation curve of sample S030 can be clearly seen in Fig. 3.20. At the beginning of the activation, the photocurrent

¹¹Samples S010–S013 were not technically p-doped, but secondary ion mass spectrometry (SIMS) measurements by Meyer et al. (2020b) show that magnesium and fluorine atoms diffuse out of the window into the GaN film at growth temperatures of about 650°C and above.

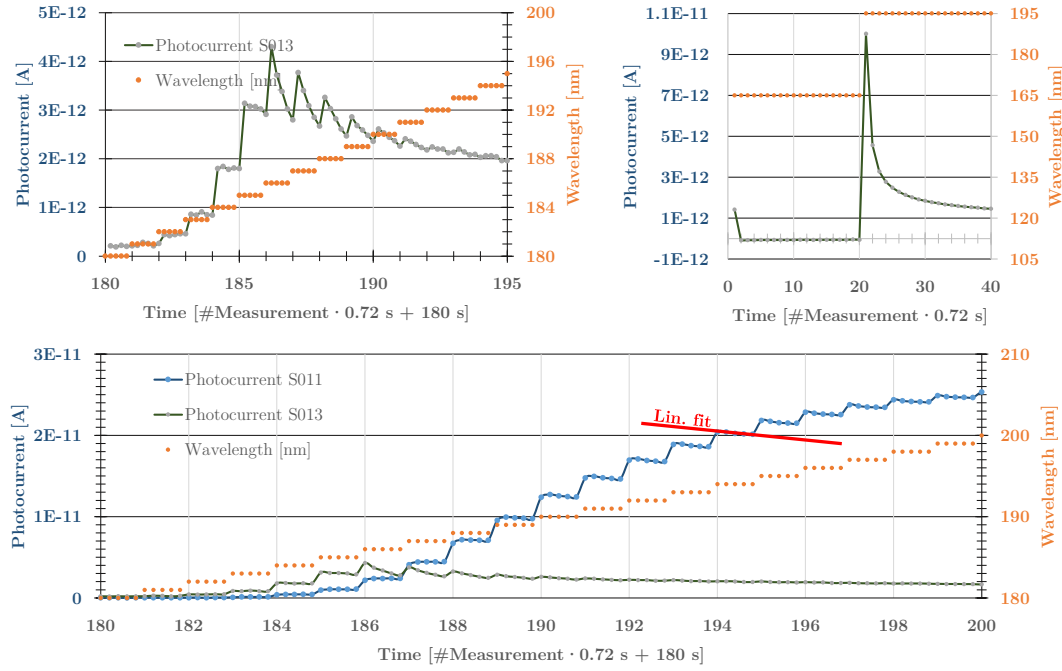


Fig. 3.18: Photocurrent of sample GaN-S013 and S011 during QE measurements near the cut-off (36 % transmittance) at about 186 nm. The time interval of the measuring points is 0.72 seconds, five measurements are recorded per wavelength, after each five measurements the monochromator increases the wavelength by one nanometre. **Top left:** In the QE measurement of S013, the photocurrent drops exponentially once the illumination becomes too high for the sample to remain uncharged. **Top right:** Photocurrent measurement according to method three (see continuous text) for determining the QE at 195 nm. **Bottom:** When comparing S013 and S011 at 186 nm, the QE of S013 is initially about twice that of S011, then the charging effects cause a sharp decrease in the QE of S013. Also S011 is not spared from charging completely, as shown by the linear fit for the five measurement points at 194 nm

Sample	Growth temp.	Mg-effusion cell temp.	QE/QE _{S012}
S030	650°C	250°C	∅ 2.3, 5.5@368 nm
S031	650°C	350°C	∅ 0.1, 0.2@201 nm
S032	650°C	400°C	∅ 0.1, 0.8@186 nm
S033	650°C	300°C	∅ 0.7, 1.8@302 nm

Tab. 3.2: Growth parameters of GaN samples S030–S033 and enhancement factor

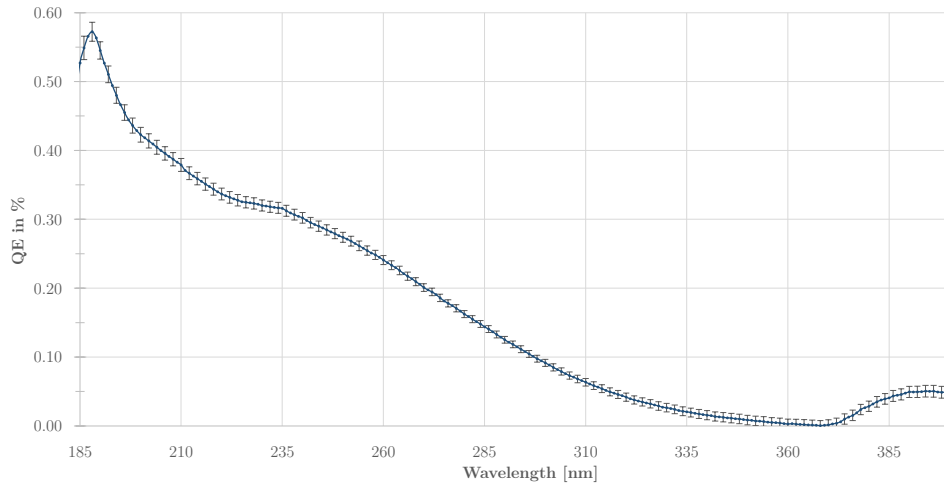


Fig. 3.19: QE measurement of sample GaN-S011 (growth temperature 600°C)

is positive. This means that electrons are excited into the conduction band, but then leave the photocathode via the metallisation contact rather than into to vacuum. About 2600 s after the start of the measurement, a first monolayer of caesium has probably been deposited on the sample (about 4 nm on the oscillating quartz), which lowers the electron affinity of the photocathode. This allows the excited electrons to leave the photocathode into the vacuum. At a certain point, approximately as many electrons leave the photocathode into the vacuum as electron holes reach the metallization ring. Thus, a resulting current of zero is measured.

This effect is not measured in samples S008–S013 and must therefore be facilitated by the (much stronger) p-doping. The fact that currents can flow along the photocathode also indicates a higher intrinsic conductivity of the GaN layer.

The increased conductivity of the film and the better contact with the metallisation ring prevent charging of the photocathode. Thus, a shorter shutter closing time can now be used, with the only restriction being that enough points are recorded to ensure that the dark current is approximately zero throughout the measurement. The better ratio of closed to open shutter allows to measure more points of the photocurrent per time interval.

Comparison of the QE of sample S012 with the p-doped samples also yields interesting results. The Mg-doping concentration of samples S031 and S032 is already too high. The QE decreases and is about zero at wavelengths longer

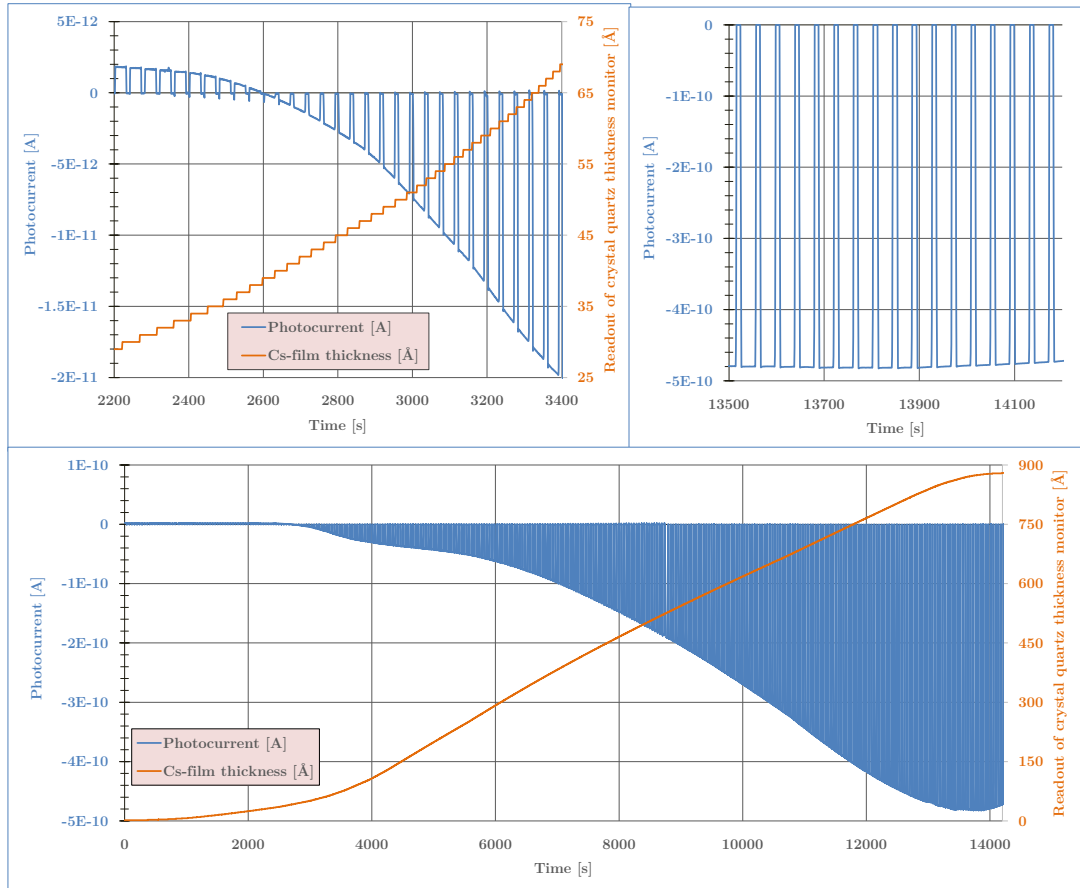


Fig. 3.20: Activation of the p-doped sample GaN-S030. The abscissa denotes the time in seconds after the start of the measurement. *Top left:* Photocurrent a few minutes after the start of the Cs-activation. *Top right:* The last minutes of the activation measurement. Charging effects are much lower compared to sample S009 (see Fig. 3.15). *Bottom:* Whole activation curve of sample S030.

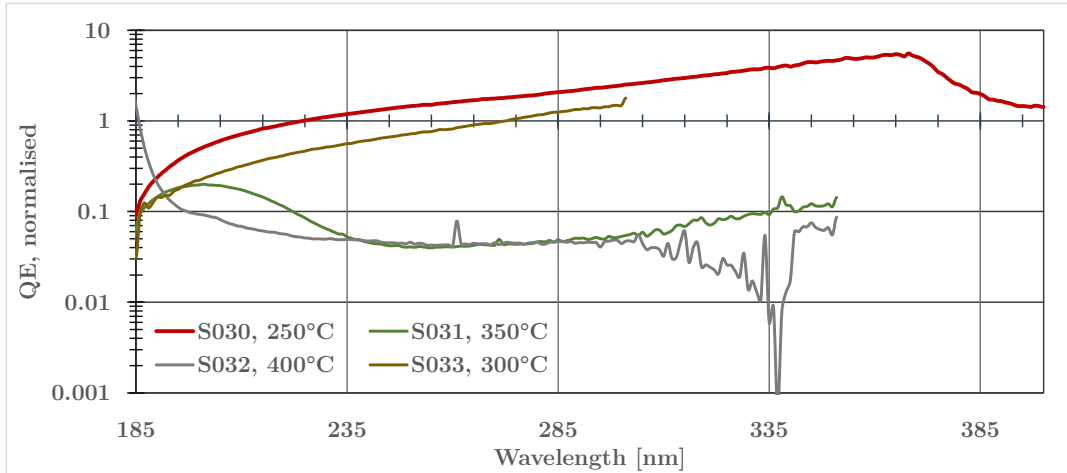


Fig. 3.21: Enhancement factor of p-doped GaN samples S030–S033 compared to S012 prepared with the same growth parameters but without p-doping.

than about 285 nm. Sample-S033 is, with a Mg-effusion cell temperature of 300°C, already at the point where the average enhancement factor over the entire wavelength is about one, with values greater than one at wavelengths longer than 275 nm. The best results are obtained for sample GaN-S030 (Mg-effusion cell temperature 250°C), with a maximum enhancement factor of 5.5 and average enhancement of about factor 2.3. This means that about a factor of two higher QE is measured for this p-type GaN sample compared to an undoped GaN sample. This is on par with the values from Norton et al. (2003) for GaN on sapphire substrates. Also it should be noted that the enhancement in QE of GaN sample S030 is higher for longer wavelengths. This is advantageous for a detector because the average QE over the entire wavelength range should be as high as possible, and it is comparatively low for undoped samples at longer wavelengths, as can be seen in Fig. 3.19. For the interpretation of the change in QE for S030, the three step model and corresponding efficiencies of each step have to be interpreted:

1. The absorption of UV photons is not affected by doping.
2. As mentioned in Chap. 2.1.3, too high doping concentrations shorten the diffusion length of the electrons in the conduction band. This seems to be the case on samples S032 and S033 with probably too high hole concentrations. The hole concentration in S030 seems low enough to not have this effect. The resistivity of p-doped GaN is lower, as the positive

holes in the now semiconducting GaN act as charge carriers. Therefore the sample charges less, which means there is no internal electric field that accelerates the electrons in the conduction band deeper into the film.

3. Due to the p-doping, the potential energy of the conduction band is higher compared to the vacuum level. Therefore the electron affinity is lower, as long as the electrons do not lose their energy in the bent-band region. The QE of S030 drops compared to S012 for high energies probably because the resulting faster electrons in the conduction band have a shorter diffusion length or even only a very short scattering length and get trapped in the bent-band region as their probability for tunnelling into the vacuum is very low. More details and corresponding figures from simulations can be found in Chap. 2.1.3.

Samples S030–S033 could successfully be used to determine a good effusion cell temperature during growth, the QE is enhanced by a factor of about two, more importantly also in the long wavelength range (275-400 nm) with a factor of almost six. To get to higher QE and allow for thicker GaN films in a next step gradient p-doped samples should be used. They combine the better conductivity, have a internal electric field that accelerates electrons to the surface and avoid the high energy drop to a smaller bent-band region.

A test setup to actually determine the hole concentration of the samples and measure their resistivity is currently under construction. This would help to optimize the effusion cell temperature more accurately, and allow comparison with other research groups and substrate types.

3.4 CsTe photocathodes – measurements

The production of high QE caesium telluride films for semi-transparent mode in the Cathode Vessel is documented in Hermanutz (2015). One of the main result is that the poor conductivity of Cs_2Te is usually the main limitation that prevents the film from achieving high QE. As described in Chap. 1.2.1 Ni, Cr and NiCr films combine a relatively low sheet resistance per thickness with a relatively high transmittance. However, a 5 nm thick Cr film already has a

transmittance of only 15-25 % in the wavelength range from 180 to 330 nm. In Hermanutz (2015) it is shown that *without* metallization a high absolute value of QE of 10 to 5 % is achieved at corresponding wavelengths of 190 to 200 nm, which is on par with the Cs₂Te photocathode in the MAMA detector of the STIS instrument on the Hubble Space Telescope. However, the QE of these films already drops to about 3 % at 240 nm and the cut-off is at around 300 nm although 330 nm would be advantageous. With metallization layer, the QE peaks at about 4-5 % but remains at this level for a much wider wavelength range.

There are two main goals to be achieved with the four batches (a batch consists of up to five samples) of caesium telluride photocathodes:

1. For the sealing test, substrates with activated photocathode and very clean sealing area are needed. Although good progress has been made, the sealing areas of GaN samples S008-S033 are not clean enough (see Fig. 3.13). Therefore, caesium telluride photocathodes with optimised sealing surfaces are the preferred option.
2. To at least reproduce the results presented in Hermanutz (2015) and, in the best case, to further optimize the QE.

3.4.1 NiCr thickness tests with samples CsTe-A1 to A5

Activation measurements of a first batch of samples are presented in Fig. 3.22. Already during activation, the influence of the full-surface metallization films, each with a different thickness (see Tab. 3.3), is clearly visible on the samples:

- The sample CsTe-A1 uses only a very thin NiCr layer (1 nm). After the first peak, the QE drops significantly as caesium telluride compounds with poor conductivity are formed. The metallization layer probably has too high resistivity to prevent the first drop, plus the layer is not necessarily continuous at these thicknesses (for details see Chap. 1.2.1 and Kim et al. (1994)). The third and final peak, is only at about 10^{-9} A.
- Sample CsTe-A2 was slightly damaged during the bake out, as shown in Fig. 3.23. Since the samples break even faster once damaged, further processing was avoided to prevent damage to the cathode vessel.

Sample	NiCr thickness	Te thickness	Cs thickness	Max. photocurrent
CsTe-A1	1.0 nm	10.0 nm	93.7 nm	9.2×10^{-10} A
CsTe-A2	2.0 nm	—	—	—
CsTe-A3	3.0 nm	10.2 nm	108.4 nm	8.4×10^{-11} A
CsTe-A4	4.0 nm	9.0 nm	97.6 nm	6.3×10^{-9} A
CsTe-A5	5.0 nm	9.4 nm	90.2 nm	2.2×10^{-8} A

Tab. 3.3: Overview about samples CsTe-A1 to A5. For the outer metallization ring, a 30 nm thick NiCr layer was deposited on all samples. The NiCr thickness refers only to the thickness of the film in the photocathode growth region. Layer thickness always refer to the thickness measured by the oscillating quartz, slightly lower thickness is obtained on the samples. Theoretically, the Cs thickness should be about 6.5 times the Te thickness to form Cs_2Te , considering only the density of the two elements. Since the sample is hotter than the oscillating quartz, more caesium is desorbed from it. The maximum photocurrent is not calibrated, but should be at least a first-order approximation for the QE that is reached at about 260 nm. Sample CsTe-A2 cracked during bake out and was not activated

- For all samples the dark current is about zero during the activation but for sample CsTe-A3. Since the NiCr film (3 nm thickness) should already absorb about 50 % of the UV light, the QE is lower. At the same time, the resistivity of the film is probably not low enough, as the first drop is less pronounced than in CsTe-A1, but still visible.
- For the sample CsTe-A4, the first drop is very small and high photocurrents are already measured.
- For the CsTe-A5 sample, there is only a tiny drop about 20 min after the start of activation. After that, the photocurrent rises to extremely high values. When the maximum is reached, the heating of the sample and the caesium dispenser is reduced and the photocurrent decreases by a factor of three. With a second, shorter activation, it can be shown that the QE can be increased back to the level of this maximum.

The QE curve of sample CsTe-A1 is exactly as expected (see Fig. 3.24). The

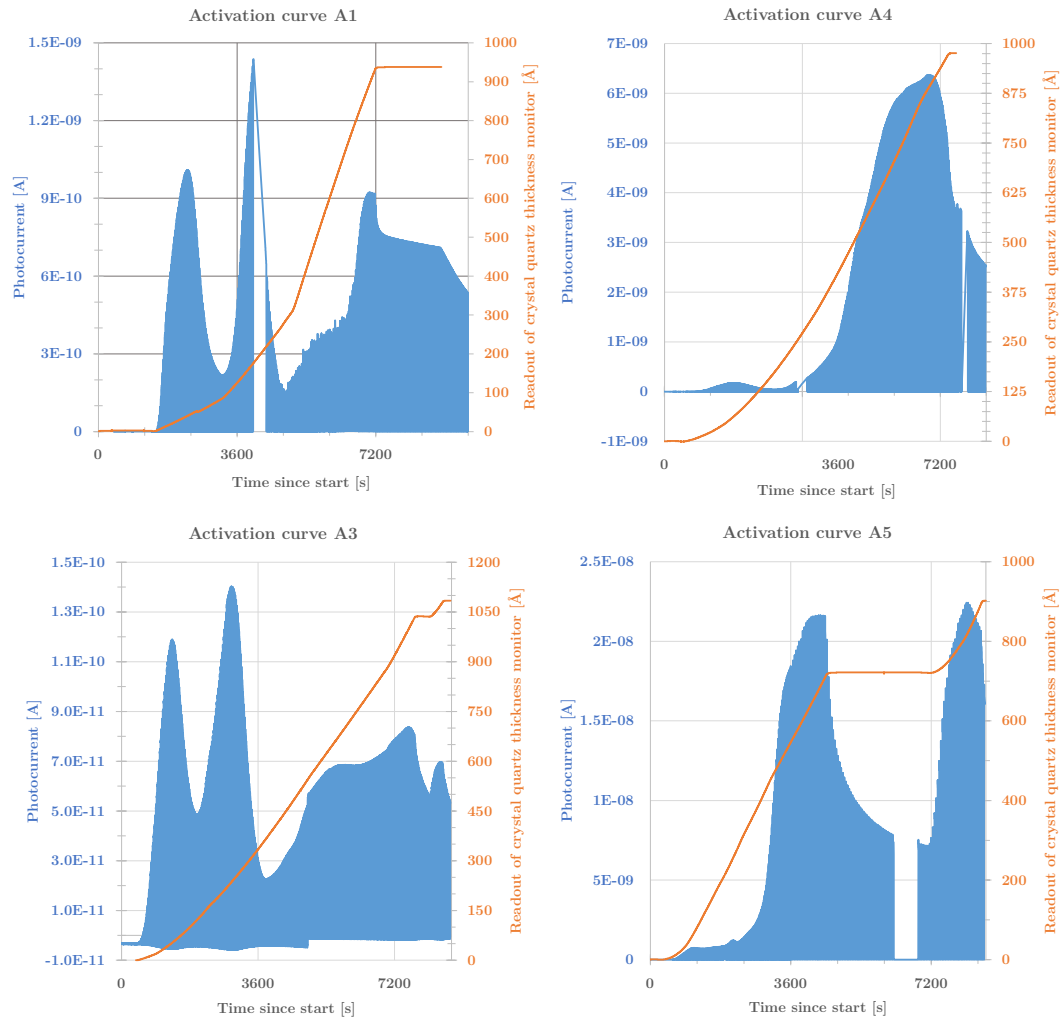


Fig. 3.22: Activation curves of samples CsTe-A1, A3, A4, and A5

QE is very high at low wavelengths, but drops off at longer wavelengths relatively quickly. This can usually be counterbalanced by the use of metallization layers, so that a higher QE is normally achieved at longer wavelengths. Thus, the QE measurements of samples CsTe-A4 and especially CsTe-A5, which have such metallization layers, do not have the expected shape. Moreover, the maximum photocurrent measured during activation of CsTe-A5 indicates a QE at 260 nm of about 5%, but should at least be significantly higher than the QE of sample CsTe-A1 at this wavelength. The deuterium bulb needed for QE measurements about one day after activation showed very unreliable results, later it was found that this behaviour is normal at the end of the lifetime of the deuterium bulb. The bulb was changed about three weeks after activation.

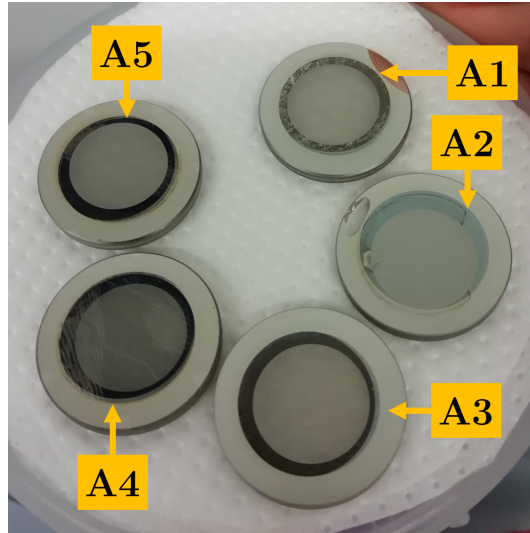


Fig. 3.23: Samples CsTe-A1 to A5 after activation

When the QE was measured again for CsTe-A4 and CsTe-A5 (see Fig. 3.24), the Cs₂Te film was already too degraded. It is normal for caesium telluride photocathodes to form a degraded tellurium film on their surface after activation, but at the same time, after an initial drop, their QE usually increases as the quality of the photocathode in their bulk increases. Stability measurements performed on a previous batch of samples showed almost no degradation even within months. Therefore, this behaviour is normally not expected for caesium telluride photocathodes as long as the partial pressure requirements are met¹².

3.4.2 Samples CsTe-B1 to CsTe-D1

As mentioned earlier, the Cathode Vessel provides five sample holders (and one open position) for samples with a diameter of 2.5 cm. Of these, three to four were usually occupied by the GaN samples S008–S033. Accordingly, one to two caesium telluride samples could be processed per batch. To avoid contamination of the GaN samples, the tellurium effusion cell was only used for the first time after the GaN tests were completed.

Two objectives were to be pursued with the caesium telluride samples. The first objective, to coat substrates such that the grown caesium telluride pho-

¹²The log files of the total pressure measurements do not show such an increase, probably the samples were damaged while the other samples were processed.

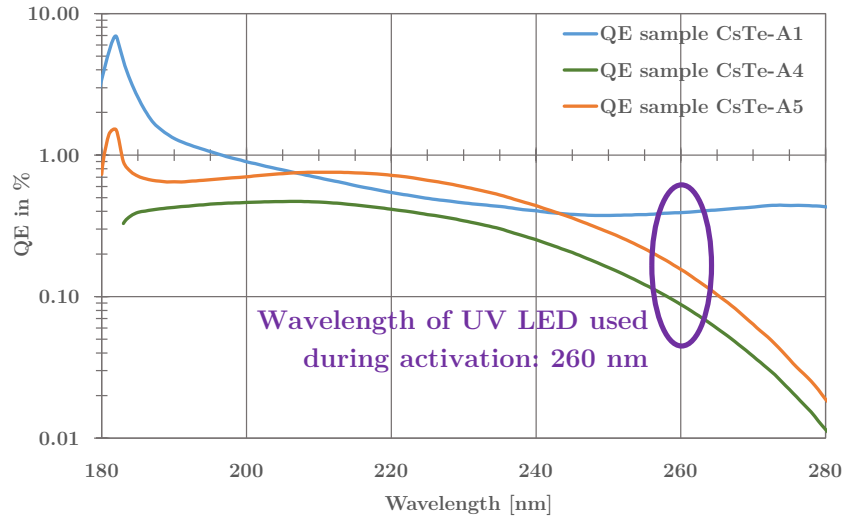


Fig. 3.24: QE measurements of samples CsTe-A1 to A5. The degradation layer on top of the photocathode of the samples CsTe-A4 and CsTe-A5 was probably very thick, and the QE dropped from about 5 % QE at 260 nm to the plotted value within a few weeks

tocathodes in sealed diodes do not degrade under air, was met, as shown in Chap. 3.2.

Therefore, the second goal, to achieve high QE over a broad spectral range, has to be achieved with these samples. Sample CsTe-A1 achieves the high QE only at short wavelengths. Despite the use of similar parameters as in Hermanutz (2015), charging effects could be avoided in the first batch (CsTe-A1 to CsTe-A5) only with much thicker full-surface metallization layers. The stability of the QE of samples A4 and A5 was also too low, so different techniques were used to avoid too much degradation of the photocathodes. Finally, with these optimised fabrication parameters, an internal QE of the photocathode of about 10 % and detection QE of about 3 % were achieved for the sample CsTe-D1 over a wide wavelength range.

Initial drop of QE

We have already seen that the QE of caesium telluride photocathodes depends on the time after their activation and on the environment to which they are exposed (e.g., $p[\text{O}_2]$). After reaching the maximum photocurrent during activation, the QE drops quite significantly by a factor of two to three. It then

Sample	Metallisation	Purpose	QE	Notes
CsTe-B1	–; NiCr/Au	Sealing	–	(1)
CsTe-B2	–; NiCr/Au	Sealing	0.2 % @ 195 nm	Sealing successful
CsTe-C1	2.0 nm; NiCr/Au	Sealing	0.4 % @ 192 nm	(2)
CsTe-C2	5.0 nm; NiCr/Au	Sealing	.43 % @ 192 nm	Sealing successful
CsTe-D1	5.0 nm; NiCr/Au	Sealing	>3 % @ 290 nm	(3)

Tab. 3.4: Overview on samples CsTe-B1 to CsTe-D1. *Note (1):* During the fabrication of the photocathode of sample CsTe-B1, the Ti sublimation pump fired, resulting in very poor QE of the photocathode. *Note (2):* QE not representative, the Cs-dispenser was already relatively empty after activation of the GaN samples. To achieve sufficiently high Cs rates, the heating current was increased. In this condition, the dispensers are extremely sensitive to changes in heating current, and a black material forms above the dispenser exit slot due to an excessively high temperature gradient. This clogs the dispenser, which is almost empty anyway, and prevents a sufficient amount of Cs from being evaporated. With new Cs-dispensers and even flatter heating and cooling curves, the problem no longer occurred. *Note (3):* Sealing was unsuccessful, but probably only because the amount of sealing solder was reduced in a previous sealing process using a GaN sample

stabilizes and increases again within a few days. An illustration of the “drop effect” is shown in Fig. 3.25. To a lesser extent, this is a temperature effect, but as described in Hermanutz (2015, Section 2.2.6), photocathode surface degradation also plays a role. The oxidized layer leads to a decrease in QE, but also slows down further degradation. The effect is smaller for caesium telluride photocathodes with higher Cs/Te ratios. This means that for Cs₂Te photocathodes, without further measures, the uppermost photocathode layers already degrade during the transfer into the Detector Vessel for sealing. Degradation of the top photocathode layers could be reduced by using storage positions, a transfer fork where the photocathode is exposed to only a small volume, and by significantly reducing p[O₂]. In the case of the sample CsTe-D1, the use of slightly more Cs than needed for the formation of Cs₂Te while lowering the temperature at the end of the activation process allows the formation of a

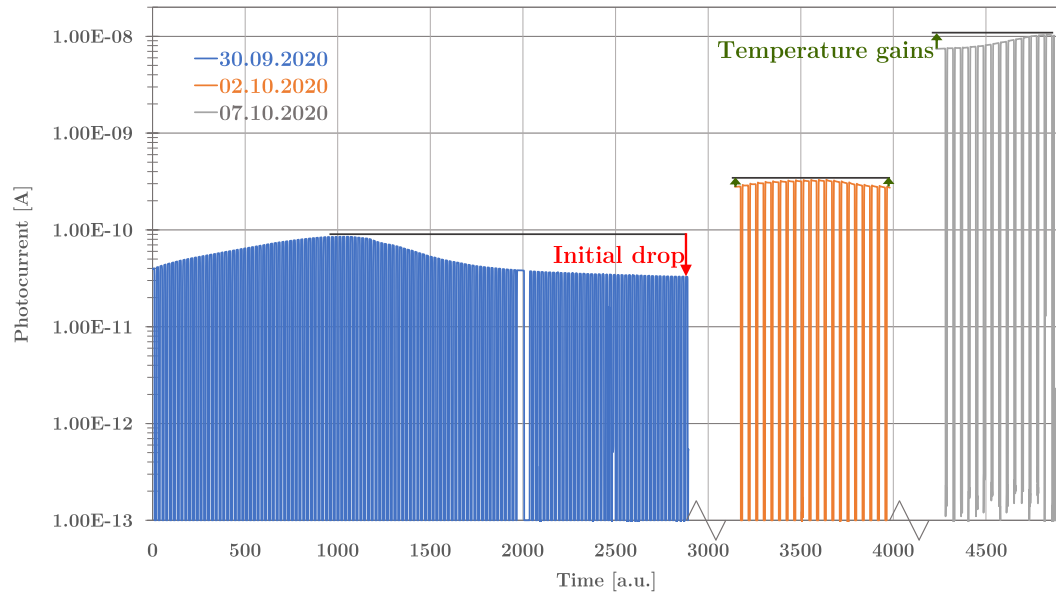


Fig. 3.25: Photocurrent of sample CsTe-D1 shortly after activation and in the following days. After reaching its maximum during activation, the QE initially drops by a factor of about 2.5. When measuring the photocurrent again after about three days, the QE is already higher. In this measurement, the sample was also heated to almost the same temperature as during activation, so that temperature effects are visible. Five days later, the QE is further increased. The effect is smaller at higher electric fields, probably because the electrons pass more easily through the degradation layer on the surface of the photocathode. Therefore, the effect should be smaller during the QE measurements

Cs-rich layer on the surface of the photocathode. This “multi-layer” approach seems to minimize the thickness of the degradation layer, as the QE raises quite significantly after the initial drop within a few days due to the higher QE in the bulk.

An example of the initial drop in QE with probably too thick degraded surface layer is illustrated in Fig. 3.10.

Production of sample CsTe-D1

Several optimization steps developed during the growth of the previous CsTe samples are used to prepare the sample CsTe-D1. The following list outlines the deviations from the standard procedure presented in Hermanutz (2015,

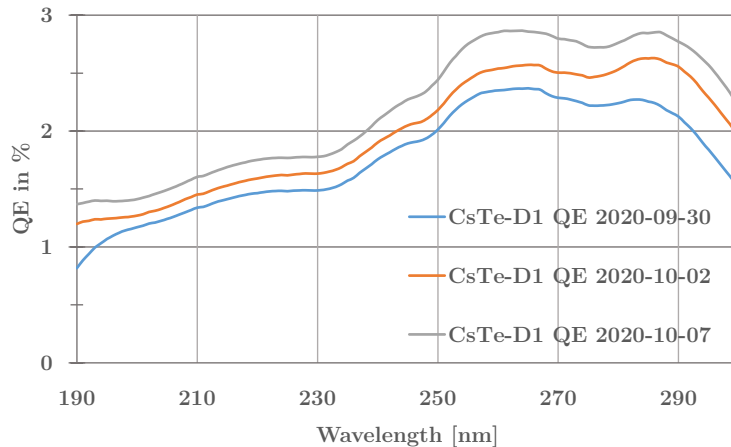


Fig. 3.26: QE of sample CsTe-D1 shortly after activation and in the following days. The difference is not as severe as in Fig. 3.25, which is probably due to higher electric fields

chap. 4.1):

- During metallization, an additional Au layer is deposited on the metallization ring, which is required for the sealing process.
- To further reduce contamination of the vessel and especially the photocathode with water, the tellurium effusion cell is heated to 270°C (with the shutter closed and using the open position of the sample dish) right after the tests with the GaN samples are completed. The total pressure in the Cathode Vessel initially increases, but then stabilizes, i.e., the increased partial pressure of tellurium leads to a slightly higher total pressure, but most of the water has evaporated¹³.
- A common technique to reduce water contamination of the first photocathode layers is to heat the sample to a slightly higher temperature (about 50 K) before deposition. First, the heater under which the sample is placed is supplied with a heating current of 4.1 A for one hour to heat the sample uniformly. This current is lowered to 4.0 A before the tellurium shutter is opened, and finally to 3.5 A when the first Te layers (0.5 nm on the crystal balance) are deposited on the sample. Since an automatic

¹³A similar approach was used before GaN activation, but with pre-heating the Cs-dispenser.

shutter was installed, the final layer thickness and the heating current can be controlled more easily and simultaneously. The thickness of the tellurium layer on CsTe-D1 is 9 nm.

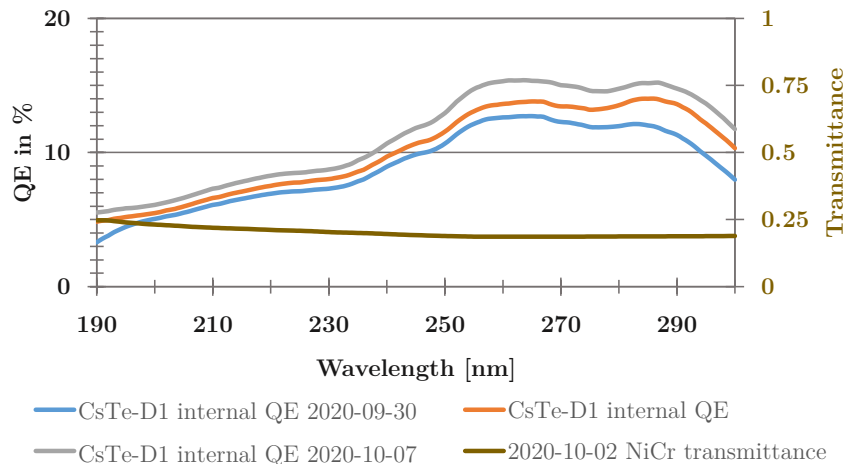


Fig. 3.27: Internal QE of the photocathode on the sample CsTe-D1 and assumed transmittance of the full-surface metallization. The transmittance includes reflection losses of a NiCr layer with 5 nm thickness (see Fig. 1.12). Thus, the internal QE specifies the conversion efficiency of the photocathode, considering only photons that actually reach it

The full-surface metallisation of sample CsTe-D1 was relatively thick at about 5 nm. In the literature, 1–2 nm thick Cr films seem to provide better results, but only if a homogeneous film is grown (Kim et al., 1994). If the Cr layer thickness is too low, aggregation occurs, which then merges at thicknesses between 1–5 nm (depending on the substrate temperature). Since the reflection of these very thin metal layers is higher than their absorption and the sample cannot be heated in the evaporation plant during evaporation, a thicker but in any case continuous layer was preferred. For the evaporation of even thinner continuous Cr layers with relatively high conductivity and transmittance, the electron-beam physical vapour deposition system could be equipped with a sample heater.

The QE of sample CsTe-D1 is highest at between 250 nm to 290 nm with 2.8 and 2.9 % respectively. A look at the internal QE (see Fig. 3.27) is useful to, e.g., figure out the influence of the metallization layer on the shape of the QE curves. The transmittance of NiCr is slightly lower at longer wavelengths, which

emphasizes the high performance of the photocathode at these wavelengths.

3.5 Discussion of the measurement results

3.5.1 Discussion and next steps for GaN samples

Two parameters, the growth temperature and the doping, were optimised so that the highest possible QE is achieved. The poor electrical contact between the GaN layer and the metallization ring limits the QE and is the next parameter to be optimised. Therefore, the samples must be annealed, but during the annealing process of test samples, they break very easily (Fig. 3.28). To avoid cracking, very dry MgF_2 substrates and flat heating curves are needed. If crystal defects are present in the sample from the manufacturing process, they are likely to break anyway. Therefore, the next step is to use “soft annealing” at lower temperatures with flat heating curves and longer annealing duration.



Fig. 3.28: Detector window (77.8 mm diameter) with GaN film but without metallisation. Despite a very flat heating curve during GaN growth, the sample gets a crack from the lower left to the centre. Three other samples could be produced without cracking problems. Thus, the sample can be used for further analysis of the GaN layer

For the samples S008 to S033, the metallisation ring was deposited before GaN growth. This approach was chosen to keep the surface of the photocathode as clean as possible. Even in a clean room, samples are exposed to humidity and other contaminants in the air. In addition, the vacuum system available for metal deposition was located in a very dusty area (without air filtration or clean room classification). The final consideration was that metal vapour might contaminate the photocathode during metallization. To eliminate these three sources of contamination, the following measures are appropriate. Moisture

contaminants are nevertheless present on the sample and must be removed after mounting in the cathode vessel with the longest possible bake-out at high temperatures. The room with the vacuum system for metal deposition has been extensively cleaned, and the air is filtered at a clean room workplace where the samples are processed most of the time. As a next step, the vacuum system itself should also be operated under a clean room tent; a corresponding setup is already in place. The extent of metal contamination due to the metallisation of the sample could be investigated, for example, with X-ray diffraction measurements. It should be relatively low, because the mean free path of the atoms during the vapour deposition is relatively high.

With the metallisation deposited after photocathode growth, ohmic contact should be achieved by “soft annealing” (24 h, 250°C). This would finally allow to:

- obtain the characteristic curve of the Mg-effusion cell temperature to the hole concentration
- measure the resistivity of the films
- use Cs/O layers for activation, with a corresponding increase in QE by at least a factor of two, but up to 20.

For the last point, a fine valve is already installed on the Cathode Vessel. After activating a photocathode, using this valve and an oxygen bottle, the total pressure should be increased to 5×10^{-8} mbar to allow the oxygen layer to form within a few minutes.

The much cleaner sealing areas should be suitable for sealing of the detector. For a successfully sealed detector, one of the challenges could be the very small distance between the photocathode and the first MCP. In addition, the role of residual gases produced by the MCPs during operation in the sealed detector and their influence on the photocathode performance has not yet been optimised. ALD-coated MCPs require much less “scrubbing” prior to their first use, so it may even be possible to maintain a good enough UHV inside the detector without needing a getter.

Cs-free GaN heterostructures would be another step to achieve good QE and improve photocathode lifetime. Monte Carlo simulations using open-source

software developed (and improved) by Marini et al. (2018b) could be used to test a variety of potential GaN layer combinations with effective NEA.

3.5.2 Discussion and next steps for caesium telluride samples

In the preparation of caesium telluride photocathodes, results similar to those obtained by Hermanutz (2015) for fully metallized samples were obtained in terms of QE. Without a metallization layer, a high QE could also be achieved using the same growth parameters, but it dropped back below 5% already at 200 nm. However, the metallized samples are more interesting for a detector because a higher QE is achieved on average over the whole wavelength range. For future sample batches, the following measures will help to further improve the QE of fully metallized (and unmetallized) CsTe samples:

- More frequent change of the oscillating quartz for the layer thickness measurements when alternating layers of, e.g., caesium and tellurium are deposited on it (see also Hermanutz (2015, 3.8.2)). This makes sure that the film thickness measurements are precise enough.
- The vessel is much cleaner because many components were replaced or components were cleaned when the Cathode Vessel was modified for coating detector windows.
- The main focus was on the preparation of GaN photocathodes. To avoid tellurium contamination of the GaN samples, these were therefore processed as the last samples. In one case, for example, the Cs dispenser was already almost empty and the sample couldn't be sufficiently activated. In all cases, when a new batch of GaN samples had to be introduced into the vessel, it was vented before further extensive QE measurements of the caesium telluride photocathodes had been made. As soon as the focus is back on CsTe samples, significantly better results should be achievable.
- For the production of thin Cr-films, the substrate should probably be heated during deposition to achieve a better surface roughness (less aggregation) and continuous film with relatively low resistivity.

Chapter 4

Analysis of UV spectra of hot white dwarfs

4.1 Stellar evolution and fundamental parameters of stars

Main sequence stars like our Sun form by the collapse of molecular clouds. Such clouds have diameters of a few parsec to hundreds of parsecs (pc, 1 pc $\approx 3.09 \times 10^{16}$ m) and masses of 10^3 to $10^7 M_{\odot}$ (Champion, 2019, chap. 1.2). In a simple model only taking gas pressure and gravitational forces into account, a cloud can collapse, if the Jeans criterion is fulfilled: The mass of a cloud must be bigger than its Jeans mass $M_J \propto T^3/(\mu^3 \times \rho_0)$ at a given initial temperature T of the cloud, density ρ_0 and molecular mass μ (for details see (Carroll and Ostlie, 2017, chap 12.2)). In a contracting cloud, fragmentation occurs, as the Jeans criterion is fulfilled for more and more smaller parts of the cloud. Therefore, binary star systems or even star clusters with hundreds of stars can form. Observations show that the formation of a single star out of (giant) molecular clouds usually does not happen, e.g. our Sun formed in such a dense star forming region but left it afterwards. Stars that could originate from the same cluster like our Sun can be identified by determining the chemical composition of a star and comparing with the well-known solar abundances (Ramírez et al., 2014), especially if they have a similar mass, i.e. also a similar luminosity and therefore lifetime on the main sequence.

To determine the chemical abundance of elements in a stellar atmosphere, an observed spectrum of that star is compared to synthetic spectra of model atmospheres. An example for an observed spectrum is given in Fig. 4.1. Such spectra are a representation of the measured energy flux over the wavelength λ with a certain spectral resolution $R = \lambda/\Delta\lambda$ of the instrument obtaining the spectra. A synthetic spectrum is computed on a given frequency grid with d_{fg} frequency points, the solution is then convolved with a function to account for the lower resolution of the observation data, e.g. a Gaussian with a full width at half maximum (FWHM) equal to an average $\Delta\lambda$. Absorption lines occur, if the observed spectra are corrected for their radial velocity shift, at wavelengths that correspond to the energy of atomic transitions of ions in the stellar atmosphere.

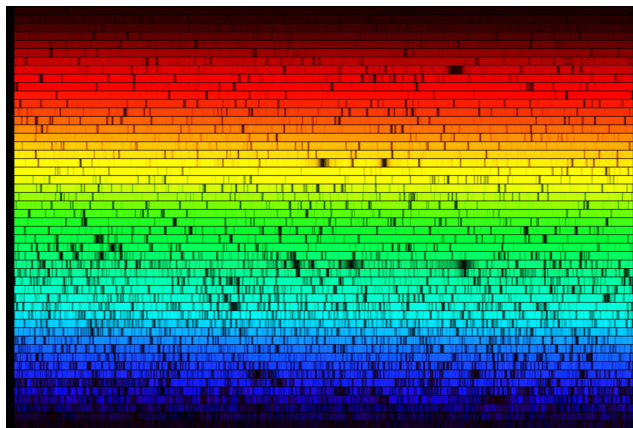


Fig. 4.1: Spectrum of the red giant star Arcturus. The spectrum covers a wavelength range from 7000 to 4000 angstroms, with each slice covering 60 angstroms. Colours are for illustration purposes. Credit for the image and details: N. A. Sharp, NOAO/AURA/NSF

The atmosphere of a star and the light originating from it are the main tool in astrophysics to determine properties like effective temperature, surface gravity $\log g$ (in cgs units), and abundances of chemical elements in the atmosphere of a star (see Chap. 4.2).

By measuring the distance to the star, the absolute magnitude M or its luminosity L can be determined. The distance to stars in our Milky Way can be determined, e.g., by parallax measurements.

By photometry and parallax measurements, stars can be plotted in the

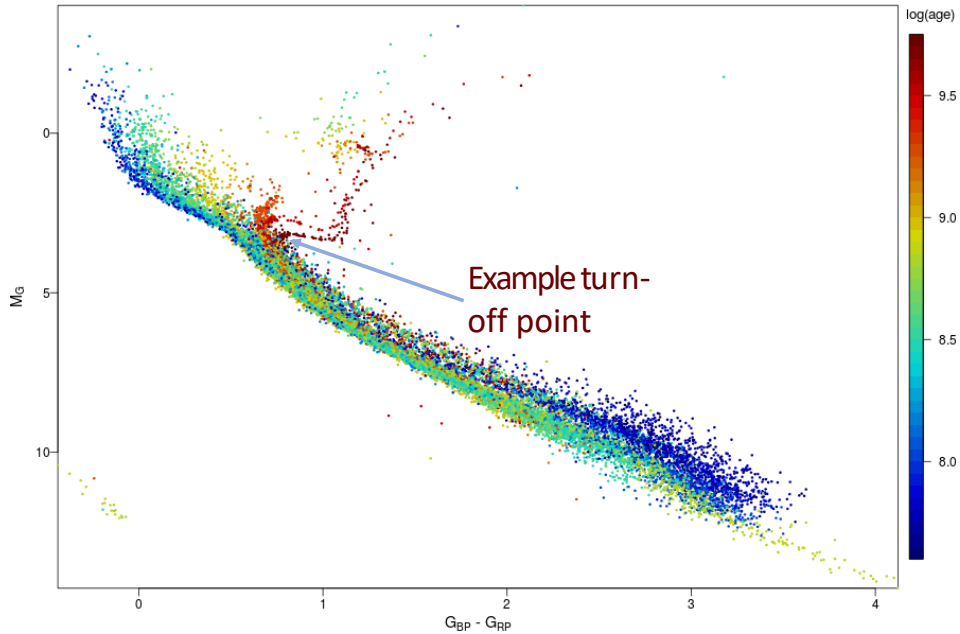


Fig. 4.2: Hertzsprung-Russell diagram of 32 open clusters, single dots are stars from the *Gaia* Data Release 2 (DR 2); image from Gaia Collaboration et al. (2018). Colours (see scale on the right) of the dots denote the age of the open clusters. The abscissa shows the Gaia $G_{BP} - G_{RP}$ color. The absolute magnitude of each star is gained from parallax measurements in the G band

Hertzsprung-Russell diagram (HRD) (see Fig. 4.2).

In the following, the evolution of stars with initial masses of less than about $8\text{--}10 M_{\odot}$ is described, as their remnants are white dwarfs. Evolutionary tracks through the HRD of such stars are shown in Fig. 4.3. The goal of the overview is to motivate the determination of the atmospheric composition of white dwarfs.

Stars with hydrogen burning in equilibrium in their cores are found on the zero age main sequence (ZAMS) immediately after their protostar phase.

The stars leave the main sequence and finally evolve to the red giant branch (RGB), if the hydrogen burning in the core ceases and hydrogen shell burning starts. Convection is the main driver in the following evolution on the RGB, evident through the change in the abundance of different elements that are transported to the surface of the star, which is the “first dredge-up”.

In the centre of the star like our Sun, He is under a very high pressure and degenerate. One of the most remarkable physical properties of degenerate matter is that increasing temperatures do not make it expand. This means

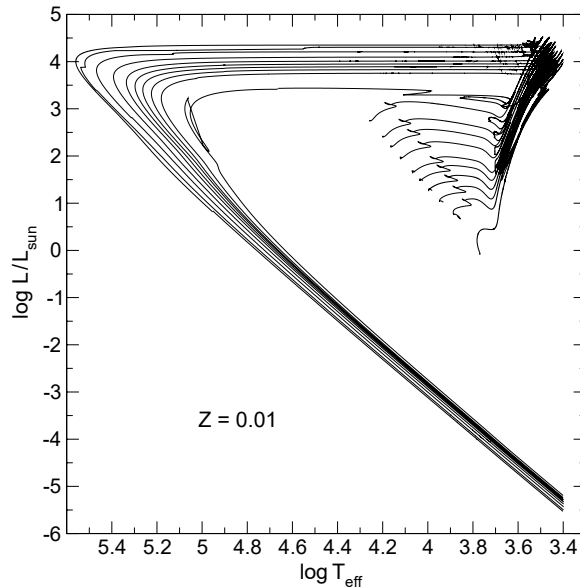


Fig. 4.3: Evolutionary tracks through the HRD of stars with initial masses of 1.0 to $5 M_{\odot}$ from Renedo et al. (2010). Very young WDs are found at the top left of the HRD and cool down within billions of years, becoming fainter and cooler.

the helium core will grow until finally the temperature is high enough to start helium burning. This results in further increased temperature and therefore highly increased fusion rates. The luminosity produced by this initial He-fusion flash can reach $10^{11} L_{\odot}$ (Carroll and Ostlie, 2017, chap. 13.2), but only for a few seconds and it is absorbed by the envelope of the red giant star. A $1 M_{\odot}$ star moves rapidly to the horizontal branch at higher temperatures, but lower luminosity compared to the late RGB phase. Further processes are on shorter timescales. At some point the helium core is exhausted and above a carbon (C) oxygen (O) core, helium shell burning becomes the main energy source of the star. Like in the hydrogen shell burning phase, the luminosity of the star rises again drastically and the star is moving onto the asymptotic giant branch (AGB).

In low mass stars, elements heavier than C and O are produced by neutron-capture nucleosynthesis. By neutron capture and β -decay, heavier elements can be formed. In Fig. 4.4¹, the fraction of the elements in the Universe formed by

¹Astronomy Picture of the Day (APOD) on 2020-08-09 <https://apod.nasa.gov/apod/ap200809.html> [18.03.2021]

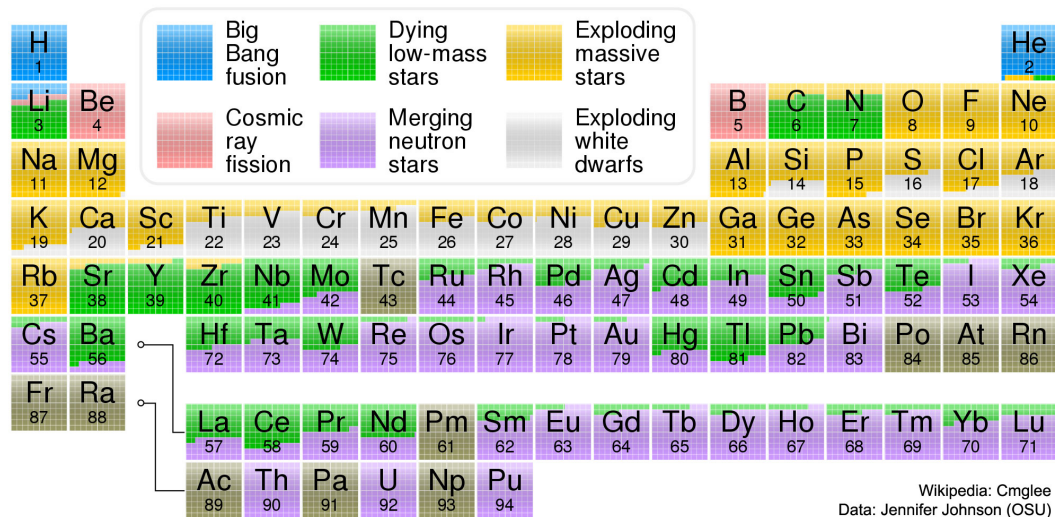


Fig. 4.4: An estimation on the percentage of the origin of different elements due to different nucleosynthesis processes

the s-process is colour-coded in green.

While on the AGB, the stars have a very high mass loss rate. For a star with an initial mass of about $8 M_{\odot}$ the mass loss rate can reach up to $10^{-4} M_{\odot}$ per year (Carroll and Ostlie, 2017, chap. 13.2). These winds and in the late AGB, the so-called superwinds, have a big influence on the surroundings of the star but also on the formation of dust grains which enrich the interstellar medium (ISM) with metals.

Inside of the AGB star, He-shell burning continues to produce more carbon and oxygen. The mass loss due to the winds prevents the degenerate core to reach the Chandrasekar limit of about $1.4 M_{\odot}$ for initial star masses below $8\text{--}10 M_{\odot}$. When the envelope of the AGB star is ejected, the hot core becomes visible. The star moves towards the blue region of the HRD, and becomes a hot white dwarf with high luminosity. Cooling tracks of WDs of different mass are shown in Fig. 4.5.

4.2 Stellar atmospheres and their modelling

When approaching the stellar atmosphere problem, a sophisticated formalism is needed to solve the respective equations with a given set of parameters. A complete review on this topic is, e.g., given in Hubeny and Mihalas (2014).

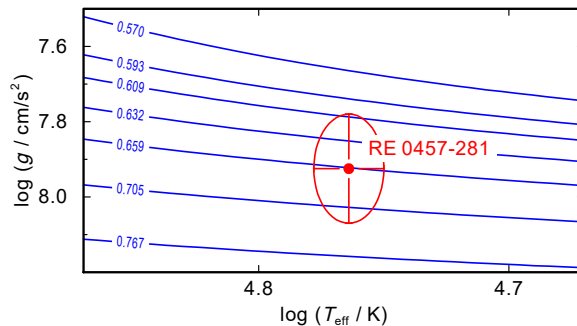


Fig. 4.5: Cooling tracks of DA-type white dwarfs with corresponding masses in M_{\odot} . In the diagram the best fit values for T_{eff} and $\log g$ including error bars for WD 0455-282 as found by Rauch et al. (2016) are plotted. Image from Rauch et al. (2016, Fig. 10)

The stellar atmosphere models presented in this chapter were obtained by using the Tübingen NLTE Model-Atmosphere Package (*TMAP*). With the package, photospheric models in Local Thermodynamic Equilibrium (LTE) and also in non-LTE (NLTE) can be computed. Non-LTE models yield good results, i.e. match the observation data well, in cases in which a LTE is not fulfilled. This is the case if due to high temperatures and relatively low densities radiative processes are dominant. Computationally much more complex NLTE model photospheres can be obtained with the program *PRO2*. This program takes a start model and begins an iterative process to solve the equations with the Accelerated Lambda Iteration (ALI) technique (see Werner (1986) and Werner and Dreizler (1999)). The input data of *PRO2* is:

- An atomic data file with the definition and frequency ν of atomic transitions. In a transition, an element in a certain ionisation stage goes from an electron configuration (and magnetic configuration) defining a state i to a corresponding state j . Each of these transition has a corresponding photon cross section $\sigma_{ij}(\nu)$. The absorption coefficient $\kappa_{ij}(\nu)$ is therefore given by the number n_i density of atoms in the state i in a unit volume times the cross section. Additionally in the atomic data file further keywords can be used, e.g. to define which transitions are calculated in LTE or NLTE, or the formula to calculate the cross section².

²The user guide to *TMAP* can be found under <http://astro.uni-tuebingen.de/~rauch/TMAP/UserGuide/UserGuide.pdf> [18.03.2021].

- A frequency grid which defines the points at which e.g. the flux is calculated.
- A suitable start model which is e.g. an LTE model with a given set of element abundances, effective temperature and surface gravity (see Sect. 4.2.2).

In Fig. 4.6 the iterative process how a final model can be gained is shown. Of each atmospheric model a synthetic spectrum is computed with the *TMAP* program *LINE1_PROF* and compared with the observational data.

LINE1_PROF then allows to estimate a synthetic spectrum with small changes to parameters of the actual input model.

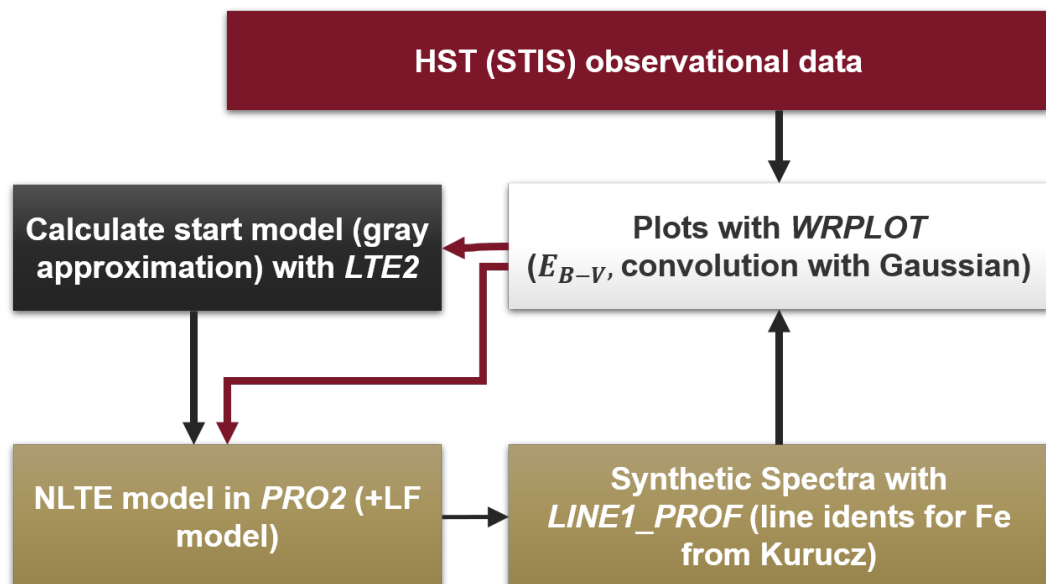


Fig. 4.6: Schematics how photospheric models were obtained with the goal of fitting the observational data of the three white dwarfs. The process was made for the determination of the abundance of each element and to determine the effective temperature. “LF model” refers to a line-formation model. In short, corresponding lines of an element can be included in the synthetic spectrum of a converged start model by only solving for the NLTE occupation numbers of the (newly) included element (for details see 4.2.3 and the *TMAP* User’s Guide)

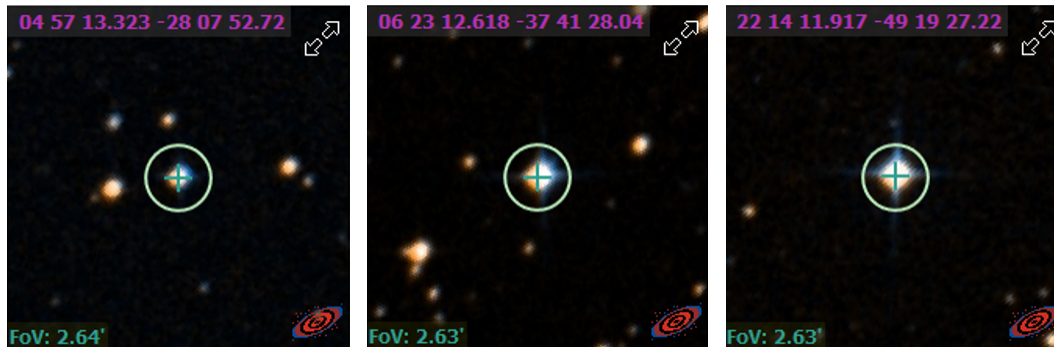


Fig. 4.7: From left to right: WD 0455-282, WD 0621-376, WD 2211-495 and their surroundings. Each image shows a section of the sky of about 2.6 arcminutes, for scale also a circle with 30 arcseconds diameter is drawn around the white dwarfs. *Acknowledgement: Images are part of the Digitized Sky Survey (DSS)*

4.2.1 Observational data

Three objects are analysed in this chapter, all of them are hot and young (cooling age about 1 Myr (Preval et al., 2019)) hydrogen-rich DA-type white dwarfs. Digitized Sky Survey (DSS) images of the objects and their surroundings are shown in Fig. 4.7. Using the example of one of the objects, WD 0455-282 (RE 0457-281), we will now look which astronomical instruments have obtained UV spectra of this object in the past with some selected results. With each spectroscopic UV instrument, its available wavelength range and its spectral resolution, strong and well known absorption lines of a certain element become detectable. The Orbiting and Retrievable Far- and Extreme Ultraviolet Spectrometer (*ORFEUS*) operated in the wavelength range from about 900 to 1400 Å. With the data obtained the abundance of He, Si, P, S and Cl of WD 0455-282 could be determined (Vennes et al., 1996). Also the Far Ultraviolet Spectroscopic Explorer (FUSE) could obtain spectra in the FUV between 905 to 1195 Å. In this case, the presence of iron can be easily determined for photospheres with $T_{eff} \lesssim 20$ kK, as for these temperatures the ionisation fraction of Fe III is high and the most dominant lines of the ion are at about 1125 Å (Vennes et al., 2006). Other instruments like the International Ultraviolet Explorer (IUE) were pointed several times at this object and very low noise spectra were obtained with several exposures of about twelve

hours each. Nevertheless the spectral resolution of IUE was not high enough to resolve iron lines. In the Space Telescope Imaging Spectrograph (STIS) several gratings with a low to very high resolution are included³, with a resolving power $R=114000$ of the E140H grating which was used to obtain the datasets listed in Tab. 4.1. In this chapter the goal is to show if iron is detectable in these very high resolution spectra of the H-rich, hot DA-type white dwarfs WD 0455-282, WD 0621-376 or WD 2211-495 and to determine the respective iron abundance.

Target Name	Dataset	Start Time	Exp. Time
WD 0455-282	OD7QD1010	2017-08-15 09:48:23	2487 s
WD 0455-282	OD7QD1020	2017-08-15 11:12:36	2964 s
WD 0455-282	OD7QD1030	2017-08-15 12:48:02	2964 s
WD 0621-376	OD7QC0030	2017-10-10 05:42:08	2881 s
WD 0621-376	OD7QC0040	2017-10-10 07:15:33	3002 s
WD 2211-495	OD7QA0020	2017-10-15 07:19:07	2966 s

Tab. 4.1: List of datasets which were used as observational data. All observations used the E140H grating in the STIS instrument and cover the wavelength range from 1320.6 Å to 1512.6 Å

4.2.2 Basic model without Fe-lines

Based on atomic data in the Tübingen Model-Atom Database (*TMAD*), a first atomic data file including the elements provided by *TMAD* can be created. When comparing two model atmospheres which differ only by one additional element, the absorption lines of the ions of the added element can be clearly identified by comparing the two models as illustrated in Fig. 4.8.

As described in the previous section, a frequency grid is required to compute an atmospheric model. To produce a suitable grid, *TMAP* provides the program *SETF2*. The frequency points are chosen in *SETF2* based on the parameters in predefined files. For example a base grid with equidistant frequency points in a given interval is created, additionally based on the wavelength of

³Spectral resolution data of STIS gratings: <https://stsci.edu/hst/instrumentation/stis/performance/spectral-resolution> [18.03.2021]

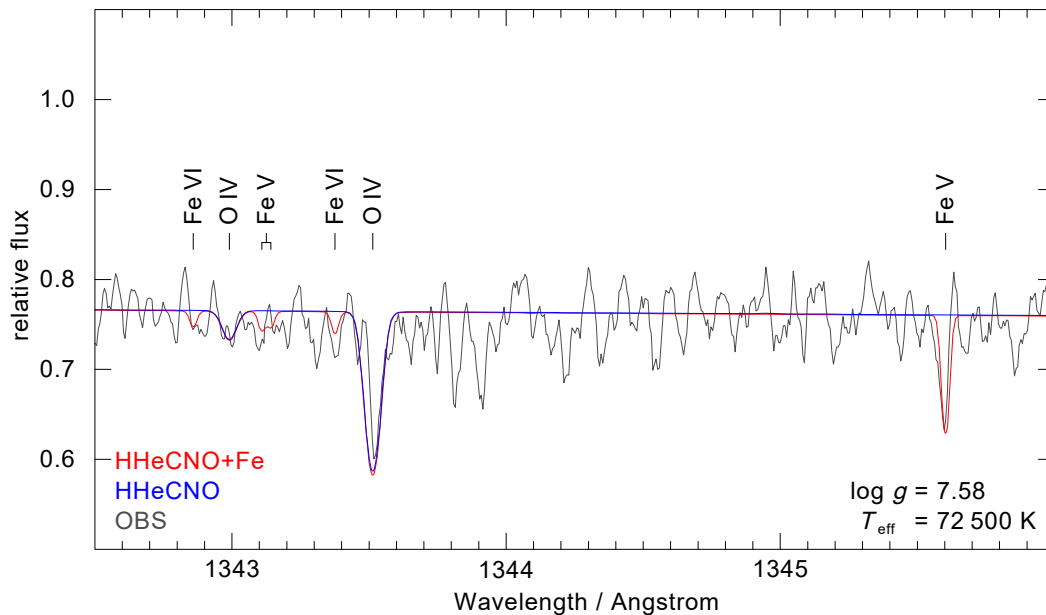


Fig. 4.8: Synthetic spectrum of two model atmospheres differing in iron abundance, and STIS observation data of WD 0455-282 in grey. Absorption lines occurring only for the red curve are therefore iron lines in the model atmosphere, some of them are also visible in the observations. The spectra are normalised to match the flux of the synthetic to the observed data. A relative flux of one equals 7.55×10^{18} erg/cm²/s

each transition defined by an atomic data file, the program can produce a finer grid around these wavelengths, such that possible corresponding absorption lines are included in synthetic spectra with high resolution.

Photospheric abundance

Spectra from white dwarfs in the FUV contain many interesting absorption lines. In addition to the spectroscopic observations, laboratory measurements are also required to precisely determine the cross section of the transition that causes this absorption line at a corresponding wavelength. As a converged start model, for the line formation model including iron lines, a less complex model with many transitions calculated in NLTE was calculated. This model then again took a converged model with atomic data files as downloaded from *TMAD*. The model included H, He, C, N and O. In this model the abundance of each element was determined by comparison with the observations. The

abundance of H and He was not determined. There are no hydrogen lines in the wavelength range of the observational data, and since the objects are DA-type WDs, there are no He lines at all. Therefore, a H-dominated atmosphere was assumed, the He abundance is expected to be zero⁴. For each plot, the synthetic spectra are convolved with a Gaussian with a FWHM equal to the spectral resolution of the astronomical instrument the observational data was obtained with. As illustrated in Chap. 4.2.1 the spectral resolution of the E140H grating is $R=114000$, i.e. the FWHM of the Gauss-profile the synthetic spectra were convolved with was chosen to be 0.01 \AA .

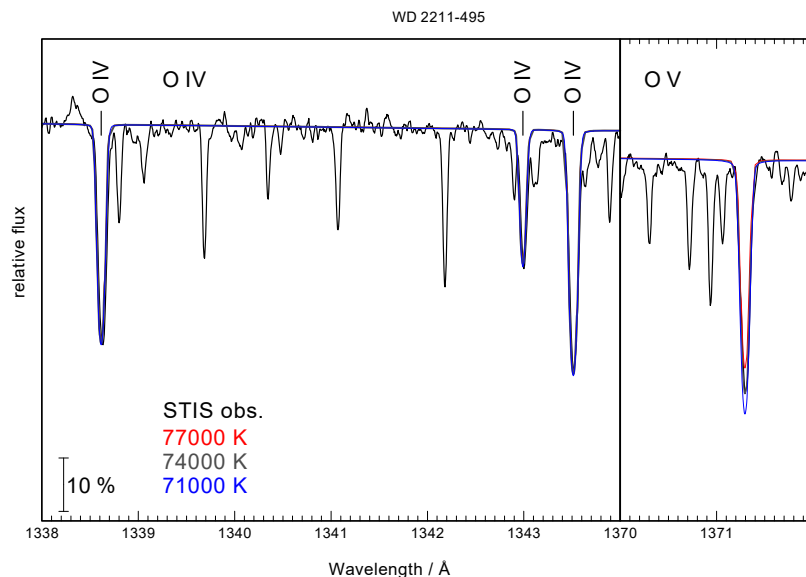


Fig. 4.9: Synthetic spectrum of a model atmosphere and the STIS observational data including O IV lines on the left and an O V line on the right. The ion fraction of O IV does not change significantly in the three models with temperatures from 71 to 77 kK. Therefore, the three curves are nearly exactly on top of each other. With such a plot T_{eff} and the abundance of an element can be determined quite accurately

⁴The models based on the data from Preval et al. (2019) are without He, own models include He, which is a mistake, for a discussion see Sect. 4.2.4.

Temperature

The population of a particular ionisation stage of a certain element can have a very weak temperature dependence within a small temperature range. Therefore the abundance of the element can be determined from respective spectral lines. The next step is to determine the effective temperature T_{eff} from ionization balances. For WD2211-495 a corresponding plot is presented in Fig. 4.9. For each of the three objects, such plots were made and T_{eff} determined to be 78.5 kK, 65 kK and 74 kK for WD 0455-282, WD 0621-376 and WD 2211-495 respectively.

In atmospheres with higher temperatures also higher ionization stages can be found and their population increases, whereas the abundance of lower ionisation stages decreases. Fig. 4.10 shows the iron ionization structure of a particular model. As a consequence, Fe I and Fe II were excluded from the atomic data file, as their population is very low. For each element and after each significant change in temperature, the ionization structure was analysed to identify ions which can be excluded from calculations.

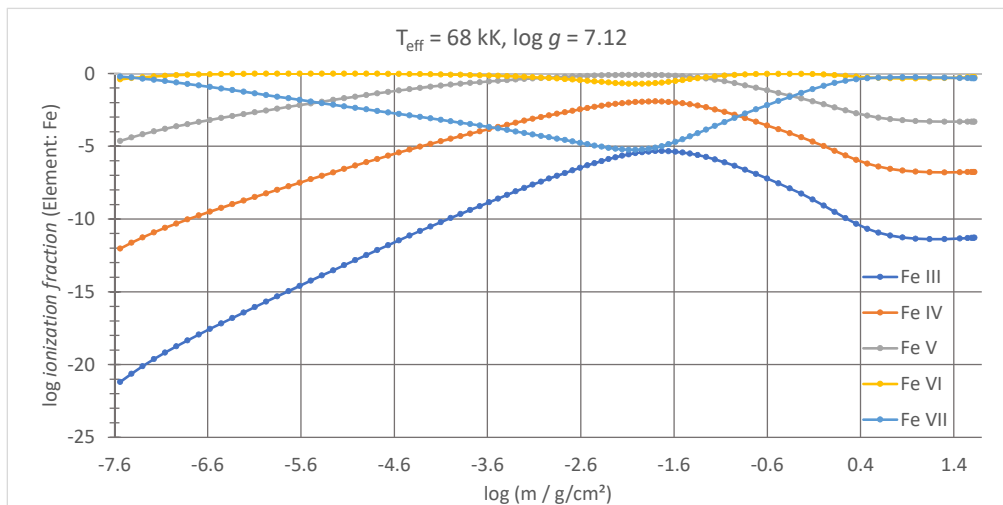


Fig. 4.10: Ionization fractions of iron versus column density in a model atmosphere of WD 0621-376.

After *PRO2* calculates a new model, also an output file with the temperature stratification should be generated. These output files can be plotted to determine, if the temperature structure is stable, e.g., no spikes occur. If not, an Unsöld-Lucy temperature correction can be used. A plot with the tempe-

perature structure over column density of the model atmosphere for the three WDs is presented in Fig. 4.11.

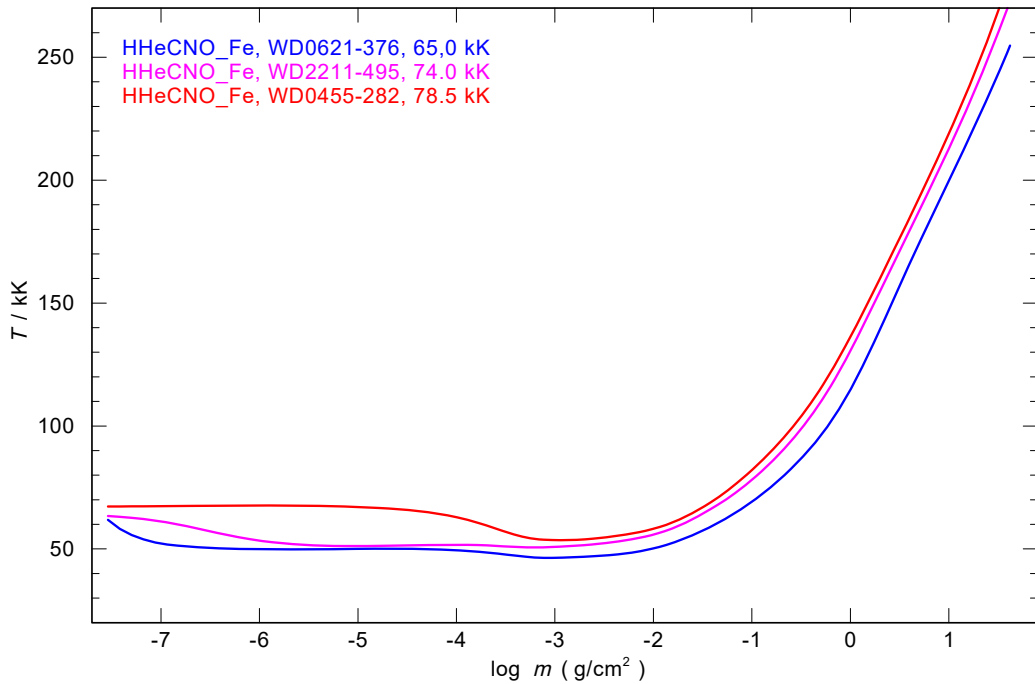


Fig. 4.11: Temperature structure of models including Fe

Interstellar reddening

The amount of extinction of star light by gas and dust in the line of view is wavelength dependent, with an increased amount of scattering and absorption for shorter wavelengths. To correct for the resulting reddening of the computed spectrum, a photometric measurement of the star with a defined filter in the infrared can be taken to normalize the spectrum (see Tab. 4.2). The normalized flux is then multiplied with the Fitzpatrick reddening law with the reddening $R_V = A_V/E_{B-V} = 3.1$ (A_V : extinction in V band, E_{B-V} : colour excess).

With this method the best value for E_{B-V} was obtained like illustrated in Fig. 4.12 for WD 2211-495 as an example. Corresponding plots⁵ for all three analysed objects can be found in the appendix, see B.1 et seqq. Where applicable, plots are corrected for reddening with the values given in Tab. 4.3.

⁵ *WRPLOT* manual: http://astro.uni-tuebingen.de/~rauch/TMAP/WRPLOT/WRPLOT_Guide.pdf [18.03.2021]

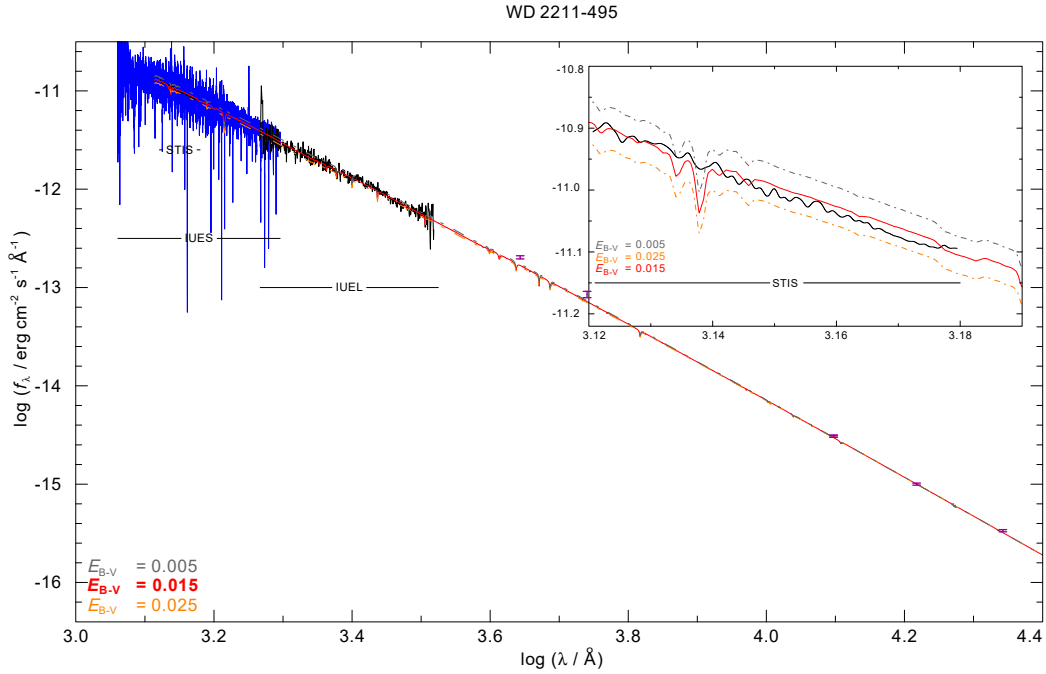


Fig. 4.12: Log-log diagram of the flux over the wavelength to determine the colour excess E_{B-V} of WD 2211-495. The points in purple with error bars are measurements of fluxes with different filters, see Tab. 4.2. A measurement in the K or H band with small error bars was used as a calibration point for each of the three objects. Also observational data is included: From the IUE data with long and short wavelength segments and on the leftmost from 1320 Å to 1512 Å the STIS data. Finally the grey, orange and red curves are three flux curves obtained with *PRO2* with $T_{eff} = 74.0$ kK, $\log g = 7.46$ and different parameters for the colour excess. On the top right a smaller section of the plot was included to show also small deviations. Due to convolution with a Gaussian with very high FWHM = 4 Å, absorption lines of the model and observational data do not match, as the purpose of the plot was mainly to determine the colour excess from the spectral energy distribution. A value of $E_{B-V}=0.015$ fits the observations best

Filter	centre wave-length [log Å]	Brightness [mag]	log flux [log erg/cm ² /s/Å]
WD 0455-282			
B	3.6435	13.65 ± 0.03 (Zacharias et al., 2012)	−13.6407 ± 0.024
V	3.7404	13.92 ± 0.02 (Zacharias et al., 2012)	−14.0109 ± 0.016
R	3.8062	14.23 ± 0.09 (Zacharias et al., 2012)	−14.3390 ± 0.072
J	4.0973	14.68 ± 0.03 (Cutri et al., 2003)	−15.4081 ± 0.024
H	4.2175	14.85 ± 0.07 (Cutri et al., 2003)	−15.8947 ± 0.056
K	4.3424	14.72 ± 0.11 (Cutri et al., 2003)	−16.3048 ± 0.088
WD 0621-376			
B	3.6435	11.88 ± 0.08 (Høg et al., 2000)	−12.9327 ± 0.064
V	3.7404	12.42 ± 0.21 (Høg et al., 2000)	−13.4109 ± 0.168
R	3.8062	12.6 (Monet et al., 2003)	−13.6870
J	4.0973	12.849 ± 0.026 (Cutri et al., 2003)	−14.6757 ± 0.021
H	4.2175	12.964 ± 0.022 (Cutri et al., 2003)	−15.1403 ± 0.018
K	4.3424	13.088 ± 0.027 (Cutri et al., 2003)	−15.6520 ± 0.022
WD 2211-495			
B	3.6435	11.28 ± 0.04 (Høg et al., 2000)	−12.6927 ± 0.032
V	3.7404	11.57 ± 0.08 (Høg et al., 2000)	−13.0709 ± 0.064
R	3.8062	11.7 (Monet et al., 2003)	−13.3270
J	4.0973	12.441 ± 0.025 (Cutri et al., 2003)	−14.5125 ± 0.020
H	4.2175	12.611 ± 0.026 (Cutri et al., 2003)	−14.9991 ± 0.021
K	4.3424	12.642 ± 0.029 (Cutri et al., 2003)	−15.4736 ± 0.023

Tab. 4.2: Photometric measurements and calculated fluxes of WD 0455-282 (first six rows), WD 0621-376 (middle) and WD 2211-495 (bottom six rows).

The values of WD 0455-282 and WD 2211-495 are in agreement with literature, for WD 0621-376 a lower value was found and used.

Object	E_{B-V}	E_{B-V} literature value
WD 0455-282	0.025 ± 0.005	0.0201 (Rauch et al., 2016) 0.0203 ± 0.0004 (Schlafly and Finkbeiner, 2011)
WD 0621-376	0.005 ± 0.005	0.0859 ± 0.0011 (Schlafly and Finkbeiner, 2011) Preval et al. (2019) assume ≈ 0.0
WD 2211-495	0.015 ± 0.005	0.015 (Gudennavar et al., 2012) 0.0137 ± 0.0011 (Schlafly and Finkbeiner, 2011)

Tab. 4.3: Values for E_{B-V} for the three analysed WDs. The data from Schlafly and Finkbeiner (2011) is accessible via the Galactic Dust Reddening and Extinction Map on <https://irsa.ipac.caltech.edu/applications/DUST/>

4.2.3 Atmospheric model including Fe lines

To include iron opacities, the Tübingen Iron-Group Opacity tool (TIRO⁶) is used. As input parameters, the program is given the line temperature ($T_L = 0.75 \times T_{eff}$), a frequency grid based on a previous model, ionisation stages, and information on the iron group elements to be included. Based on these inputs, the program generates an atomic data file, which is then used to compute a new LF-model. The Fe abundance in the model is adjusted slightly, until the observational data is matched in corresponding plots. In addition, the parameters determined by Preval et al. (2019) for these objects were taken to calculate corresponding model atmospheres.

To determine the Fe abundance as precisely as possible, the spectra can also be rectified, for an example see Fig. 4.13.

4.2.4 Comparison of the results and discussion

In previous analyses of the photospheric abundance using *TMAP* by Rauch et al. (2016), which included the analysis of WD 0455-282 (RE 0457-281), an

⁶The TIRO tool (<http://astro.uni-tuebingen.de/~TIRO>) was constructed as part of the activities of the German Astrophysical Virtual Observatory.

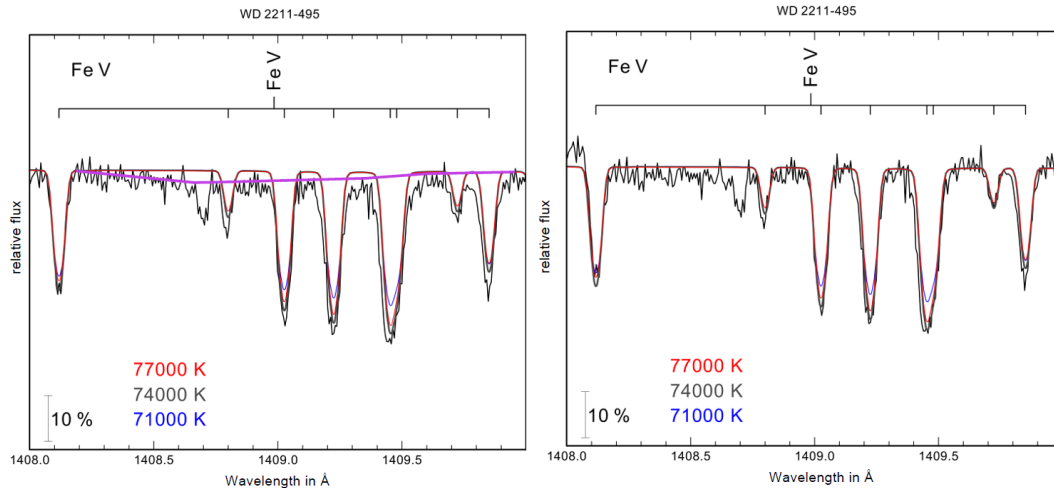


Fig. 4.13: Example for the rectification of a spectrum

upper abundance limit for Fe of 0.01 times solar ($N(\text{Fe})/N(\text{H}) < 10^{-6}$) was determined. For this object and based on the STIS data given in Tab. 4.1, Preval et al. (2019) determined a higher abundance $N(\text{Fe})/N(\text{H}) = 2.72 \cdot 10^{-6}$. A synthetic spectrum obtained with the parameters⁷ from Preval et al. (2019) in *TMAP* does not fit the observational data well. For WD 0621-376 a corresponding plot is presented in Fig. 4.14, for WD 0455-282 and WD 2211-495 see Fig. B.14 to Fig. B.17. The fit parameters and further input parameters of the respective models are presented in Tab. 4.4.

Normally, the atmospheric code *TLUSTY* used by Preval et al. (2019) and *TMAP* used for the calculations presented in this chapter would be expected to produce similar results. Therefore, the deviations that can be seen, e.g., in Fig. 4.14, are surprisingly high. In own calculations, with abundances about three times as high, the observations are fit the best. However, these own models also included helium, which is not correct for DA-type WDs. Therefore, the values for T_{eff} and the abundances must be recalculated. First recalculations show that with this correction, also the very high effective temperature of WD 0455-282 and WD 2211-495 get closer to the model parameters of Preval et al. (2019).

The analysis of UV spectra of hot white dwarfs had three main goals. To have a good understanding of how data obtained with the UV MCP detector

⁷Si, P, S, and Ni were not included in the corresponding model atmospheres, as their number fractions are smaller than 10^{-6} and should be negligible

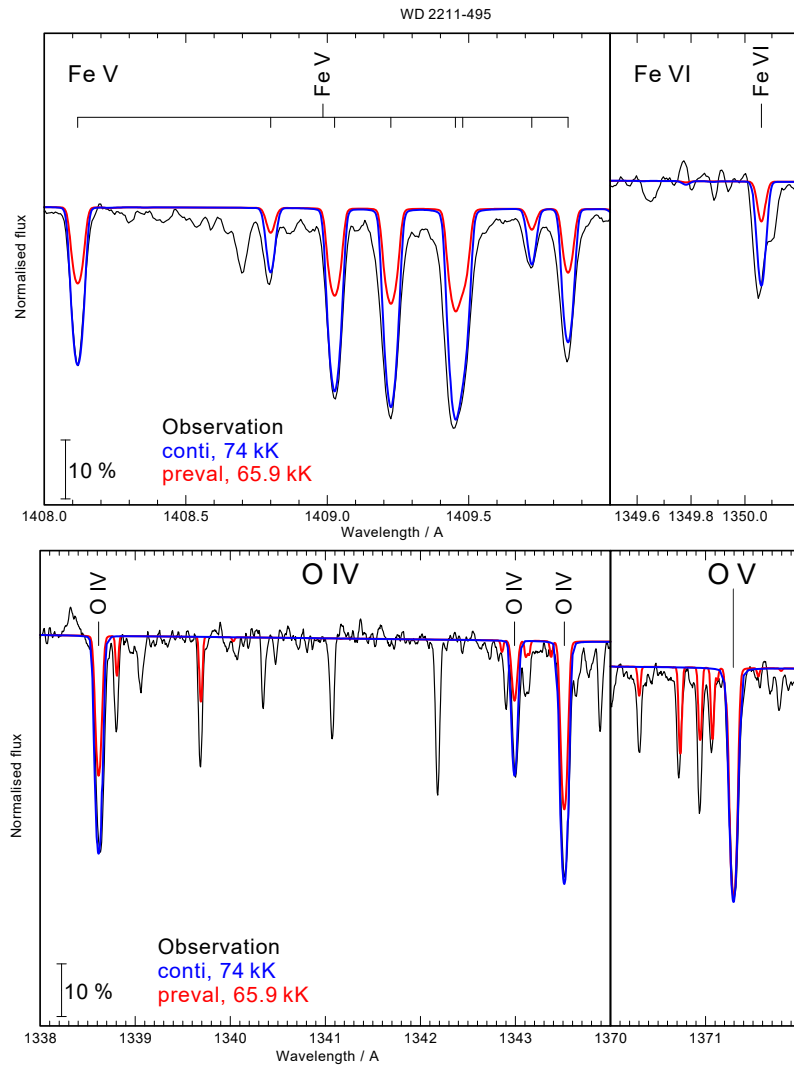


Fig. 4.14: Synthetic spectra including O and Fe lines with parameters from Preval et al. (2019) (red line), own models (blue line) and observational data (black line) of WD 2211-495. The flux of the observational data is normalised by dividing with a factor of 1.51×10^{-11} , the synthetic spectra are then normalised to a point on the continuum. In the plot showing O IV and O V, also some Fe lines are present. The synthetic spectra with higher temperature and higher abundances seem to match the observational data better

		WD 0455-282	WD 0621-376	WD 2211-495
Conti	T_{eff} (kK)	78.5	65.0	74.0
Preval+	T_{eff} (kK)	65.4	64.5	65.9
Conti	$\log g$ (cgs)	7.58	7.12	7.46
Preval+	$\log g$ (cgs)	7.87	7.60	7.58
Conti	v_{rad} (km/s)	+81.0	+36.0	+29.5
Preval+	v_{rad} (km/s)	+81.5	+37.4	+30.0
Conti	n(O)/n(H)	4.66×10^{-7}	5.96×10^{-6}	6.67×10^{-6}
Preval+	n(O)/n(H)	1.58×10^{-7}	2.46×10^{-6}	2.00×10^{-6}
Conti	n(Fe)/n(H)	7.60×10^{-6}	1.29×10^{-4}	2.87×10^{-5}
Preval+	n(Fe)/n(H)	2.72×10^{-6}	1.84×10^{-5}	1.21×10^{-5}

Tab. 4.4: Comparison of fit- and model-parameters. Lines with “Preval+” present model parameters from Preval et al. (2019, table 5). The values for the surface gravity $\log g$ are taken from Gianninas et al. (2011)

should look like, analysing existing data is the first step. Thus, the first goal was to get hands-on experience in working with observational data, e.g. by plotting the data, and rectification. At the end of a mission, the data obtained with the detector may need to be analysed. Accordingly, the second objective was to acquire the knowledge needed for this purpose by analysing existing data. These two goals were achieved, the measure of how successfully is determined by the third goal. When the obtained results were compared with the literature, some discrepancies were noticed. Although the generated synthetic spectra match the observational data quite well (see Fig. B.5 to B.13), the determined effective temperatures and abundances are still uncertain, since solar helium abundances were used in the models, while the objects analysed are free of helium. New models must be calculated to obtain final results.

Chapter 5

Conclusions

Due to technological advances and miniaturisation, smaller and lightweight instruments already contribute significantly to scientific progress. The capabilities of small space telescopes, cubesats, or stratospheric balloon-borne observatories should not be underestimated. Compared to flagship missions, they have shorter lead times and can compensate for their lower throughput due to small mirror size, by being optimised for a specific scientific goal and allocating all their observation time on it.

For this purpose, an advanced UV-MCP detector is currently being developed at IAAT, which is sensitive from the NUV to the FUV. Its low power consumption, size and mass allow integration into an instrument the size of a cubesat. In addition, the design is relatively flexible, i.e., optimised windows, photocathode materials, MCPs, to name a few, can be used depending on the scientific objective. In a first publication (Conti et al., 2018), the development status of the detector was discussed. First images could be obtained in a test stand, but the sealing process needed further optimization, and GaN was not yet used as photocathode material.

For the purpose of further optimization, possible material (combinations), coatings and their advantages and disadvantages were discussed for each part used in the detector head. Based on this discussion, several design decisions were made. For full surface metallization of the window, which is required in the case of caesium telluride photocathodes, 3 nm thick Cr (or Ni) coatings are the best solution. ALD-coated GCA-MCPs have been implemented in the current detector, and it has been confirmed that their higher gain modulations

are compatible with our detector electronics. Due to their higher extractable charge, the lifetime of the detector is longer. The wetting of sealing surfaces was analysed and consequently Au coatings were used as substrates for the sealing tests.

The theoretical description of the photocathode processes and detailed discussion of the optimised NEA photocathodes was useful to interpret the results obtained in photocathode growth. The photocathode production included caesium telluride and GaN photocathodes. For fully metal-coated substrates with caesium telluride photocathodes, results from previous work could be reproduced. Further optimization steps include vapour deposition of more homogeneous Cr layers at even lower thickness on the sample. For this purpose, it should be considered to include a heating device in the evaporation chamber. Using GaN films on MgF_2 substrates, tests on the QE dependence on the growth temperature, and the temperature of the Mg effusion cell were performed to obtain p-type GaN. The parameter tree was successfully narrowed down for these two growth parameters, but the electrical contact between the GaN layers and the metallization ring was still not optimal. Cracking occurred when the samples were annealed because MgF_2 could not withstand the temperature gradient normally required for successful annealing. For future samples, a “soft annealing” procedure will be used, annealing them only at 250°C , but for 24 hours. The better contact should allow high or even very high QE with Cs/O activation layers. In the sealing tests, two sealed diodes with activated caesium telluride photocathode were fabricated. No measurable degradation occurred within several weeks. Excellent stability and reproducibility were achieved in the QE measurements in the nitrogen test stand with warm-up times as short as 30 min. The progress achieved was also presented in Conti et al. (2020).

The high-resolution STIS spectra of the hot white dwarfs WD0455-282, WD0621-376, and WD2211-495 were analysed. The surface temperature, O, and Fe abundances were varied to fit the synthetic spectra to the observational data. Comparison of the results with the literature revealed interesting discrepancies. Improved model atmospheres should be calculated for further comparisons.

Appendix A

Supplements to the photocathode measurements

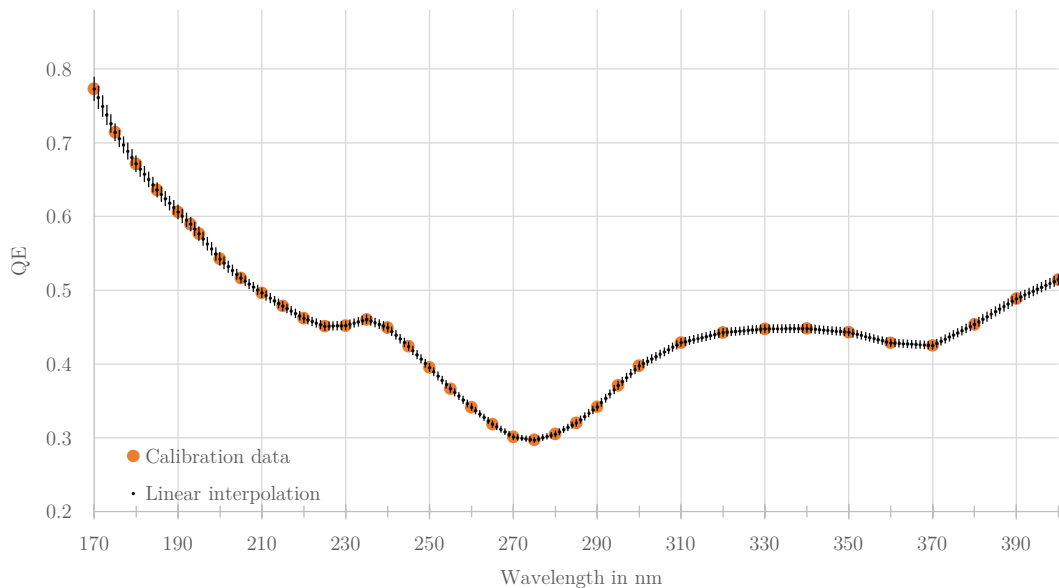


Fig. A.1: Interpolation of the PTB calibration data with error bars

Measurement and calibration of data plotted in Fig. 3.7

First the quadrupole head was degassed¹ for one minute, to avoid contaminants on the filament to have an impact on the actual measurement. During degassing, the pressure in the UHV chamber can rise by one order of magnitude. The measurement was started after the pressure returned to its initial value. To acquire the data plotted in Fig. 3.7, 232 measurement points per molecule

¹Details in the “Dycor System 2000 Software Manual”, <https://www.ametekpi.com/products/brands/dycor/system-2000-software> [18.03.2021]

were taken over the course of one hour. As the mass spectrometer does not actually measure pressures but ion currents, a corresponding offset and gain factor was calculated based on the already calibrated pressure measurement of the ion pump in the cathode vessel at the beginning of the measurement. During the measurement, the pressure decreased slightly. For correction, i.e. to obtain the mean value and standard deviation of the partial pressures if the pressure had remained at its initial value, a linear fit to the measurement points was plotted. The difference between the linear fit and initial value defines the correction value for each measurement point.

In the case of tellurium, the ion current of the isotope ^{130}Te was measured. The abundance of this already most abundant isotope of tellurium is only about 34%. Consequently, the partial pressure was divided by 0.34 to obtain the partial pressure of all main isotopes of tellurium.

Each measurement point was obtained with an integration time of 120 ms, except for Cs and Te with 500 ms integration time to achieve a better signal to noise ratio. For all molecules, only single charged molecules were taken into account, as discussed in Sect. 3.1.2.

Channel	Part. pres./mbar	Channel	Part. pres./mbar	Channel	Part. pres./mbar
1	6.57E-11	48	1.10E-13	95	1.20E-14
2	8.30E-12	49	3.10E-14	96	1.44E-15
3	1.00E-13	50	9.19E-14	97	1.30E-14
4	6.85E-14	51	8.55E-14	98	9.57E-15
5	0.00E+00	52	6.30E-14	99	4.75E-15
6	0.00E+00	53	7.57E-14	100	8.07E-15
7	0.00E+00	54	5.48E-14	101	2.99E-15
8	2.93E-13	55	1.76E-14	102	7.61E-15
9	0.00E+00	56	1.55E-13	103	9.95E-15
10	0.00E+00	57	1.35E-13	104	8.30E-16
11	1.84E-13	58	7.62E-14	105	1.03E-14
12	1.31E-11	59	2.23E-14	106	9.38E-15
13	2.29E-13	60	1.04E-13	107	9.21E-15
14	6.26E-12	61	1.47E-15	108	1.59E-14
15	1.61E-11	62	2.46E-14	109	9.76E-15
16	5.77E-11	63	4.18E-14	110	4.05E-15
17	1.02E-10	64	1.30E-13	111	3.58E-15
18	3.98E-10	65	6.98E-14	112	4.44E-15
19	3.64E-12	66	1.35E-13	113	3.05E-15
20	1.18E-12	67	7.27E-14	114	5.98E-15
21	2.65E-14	68	3.12E-14	115	9.24E-15
22	1.12E-13	69	4.42E-14	116	7.07E-15
23	8.45E-16	70	4.33E-14	117	4.47E-15
24	3.51E-13	71	3.51E-14	118	5.63E-15
25	9.47E-13	72	2.28E-14	119	4.56E-15
26	3.64E-12	73	1.09E-14	120	9.47E-15
27	7.88E-12	74	1.68E-14	121	8.96E-16
28	7.11E-11	75	9.86E-15	122	2.16E-14
29	5.30E-12	76	1.37E-14	123	1.84E-14
30	2.20E-12	77	4.10E-14	124	3.24E-14
31	1.43E-12	78	5.31E-14	125	6.43E-14
32	1.89E-12	79	4.00E-14	126	1.21E-13
33	5.16E-14	80	1.55E-14	127	7.62E-14
34	3.52E-14	81	2.21E-14	128	2.07E-13
35	6.80E-14	82	1.81E-14	129	8.84E-15
36	1.29E-13	83	2.42E-14	130	2.05E-13
37	2.28E-13	84	1.97E-14	131	2.17E-14
38	3.06E-13	85	1.49E-14	132	3.21E-13
39	8.34E-13	86	8.31E-15	133	1.01E-12
40	1.78E-12	87	4.04E-16	134	5.92E-15
41	1.24E-12	88	5.00E-15	135	8.08E-15
42	1.38E-12	89	4.38E-15	136	6.00E-15
43	3.80E-12	90	8.93E-16	137	1.24E-14
44	1.31E-10	91	3.41E-14	138	1.40E-14
45	2.72E-12	92	1.53E-14	139	2.54E-14
46	7.91E-13	93	1.61E-14	140	2.81E-14
47	4.33E-14	94	9.10E-16		

Tab. A.1: List of the partial pressures plotted in Fig. 3.7

Appendix B

Supplements to the analysis of the UV spectra of hot white dwarfs

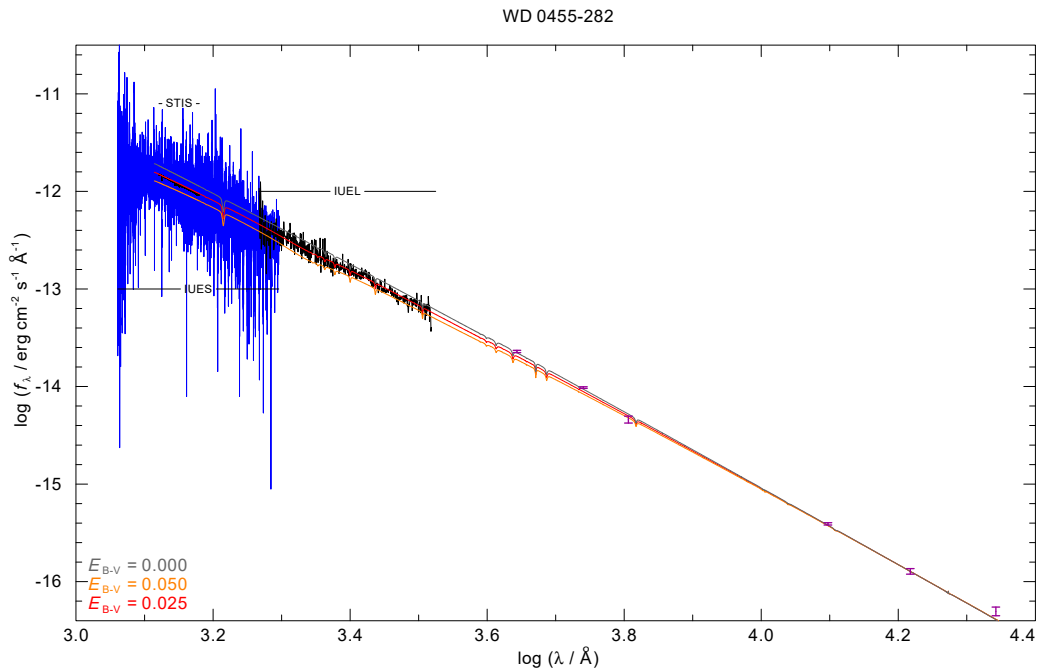


Fig. B.1: Plot for determination of E_{B-V} of WD 0455-282, see Fig. 4.12 for descriptions. Note that the slope of the best fit curve is slightly different from the slope of the STIS data, therefore a rather big error bar for E_{B-V} was assigned. Data of *PRO2* model: $T_{\text{eff}} = 78.5$ kK, $\log g = 7.58$

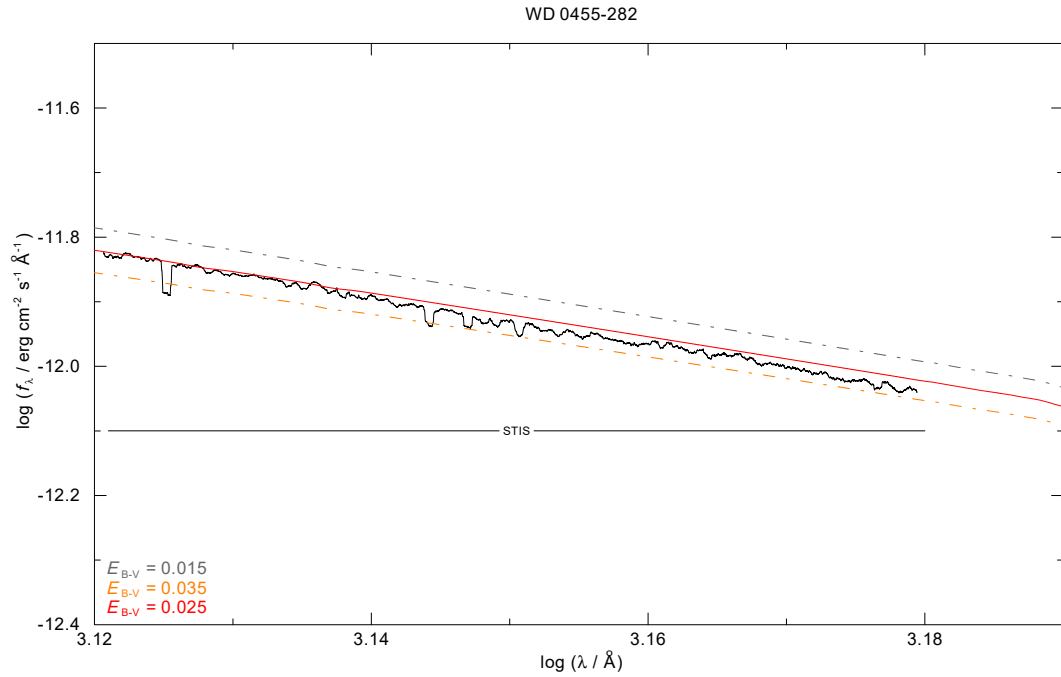


Fig. B.2: Detailed plot for the determination of E_{B-V} of WD 0455-282

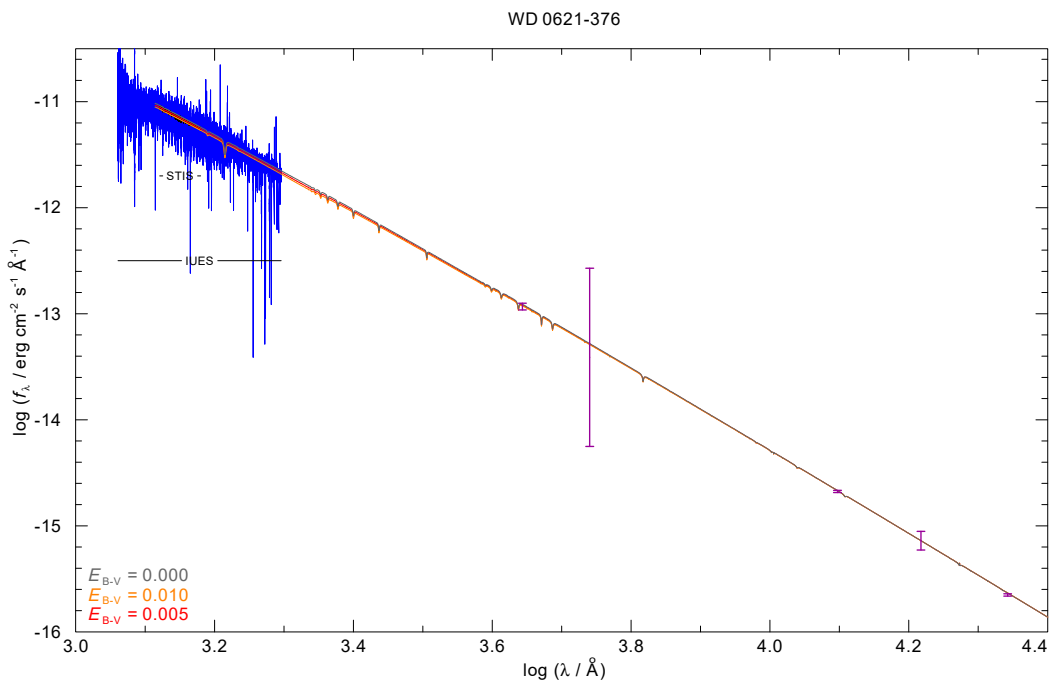


Fig. B.3: Plot for determination of E_{B-V} of WD 0621-376, see Fig. 4.12 for descriptions. *PRO2* model: $T_{\text{eff}} = 65.0$ kK, $\log g = 7.12$

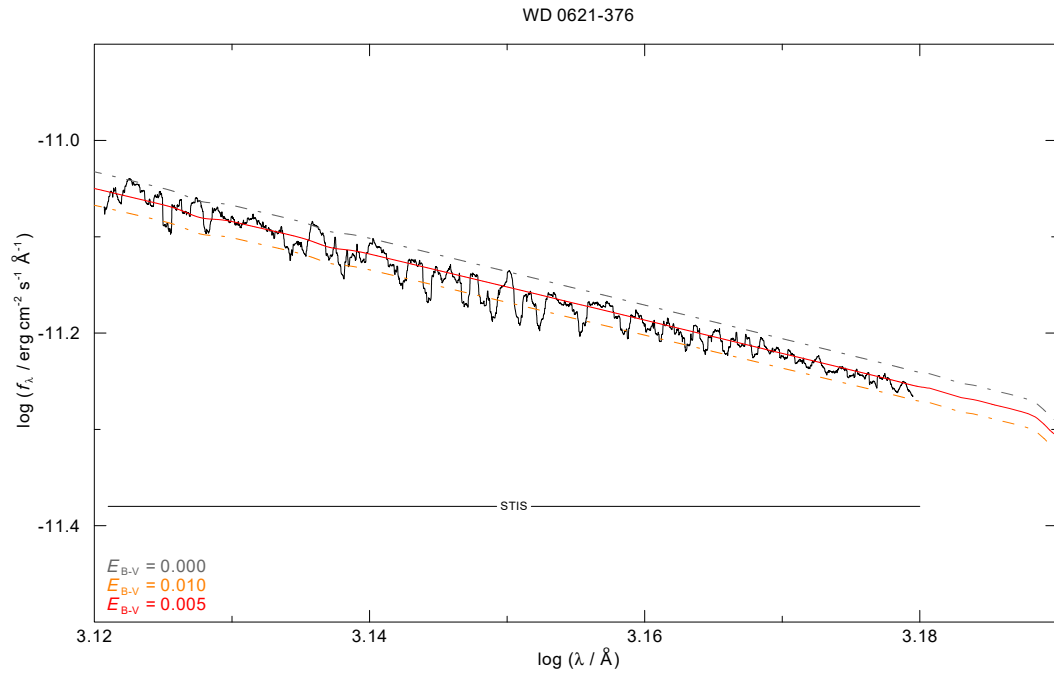


Fig. B.4: Detailed plot for the determination of E_{B-V} of WD 0621-376

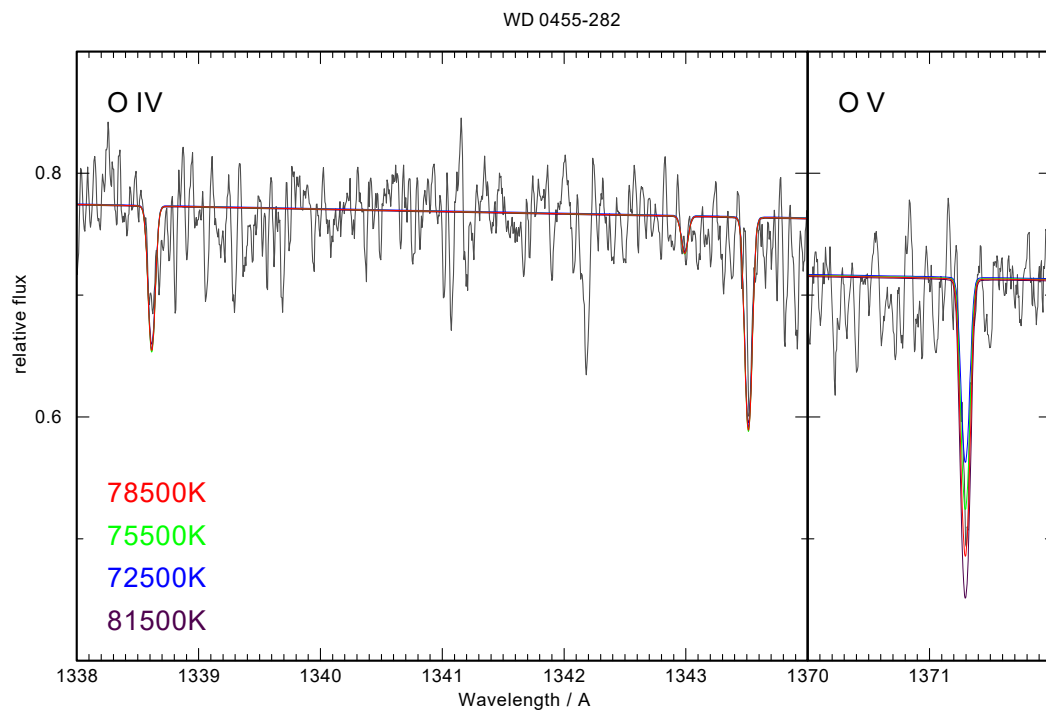


Fig. B.5: Plot to determine the O abundance and T_{eff} of WD 0455-282

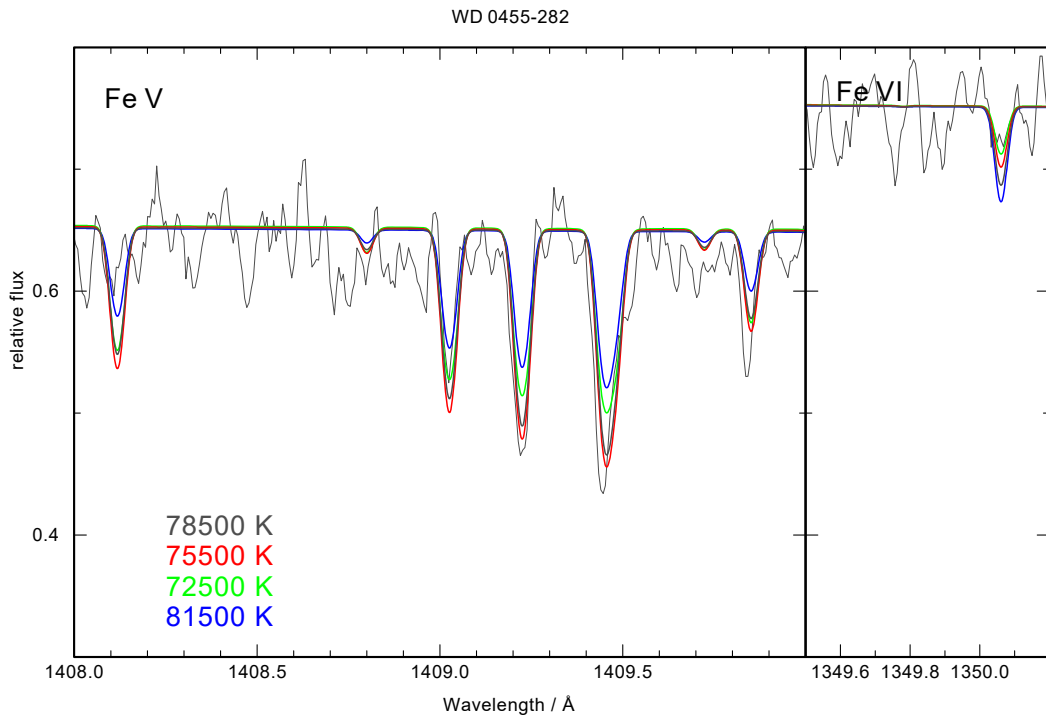


Fig. B.6: Plot to determine the Fe abundance of WD 0455-282. The synthetic spectra with +3 kK and -6 kK with respect to T_{eff} are plotted for comparison

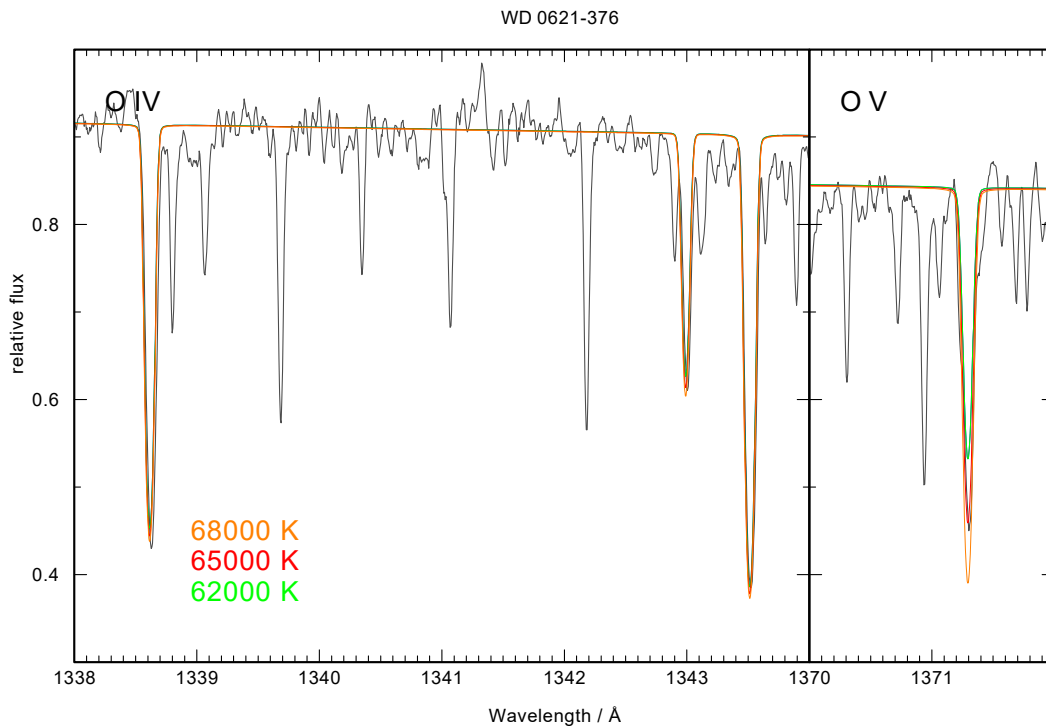


Fig. B.7: Plot to determine the O abundance and T_{eff} of WD 0621-376

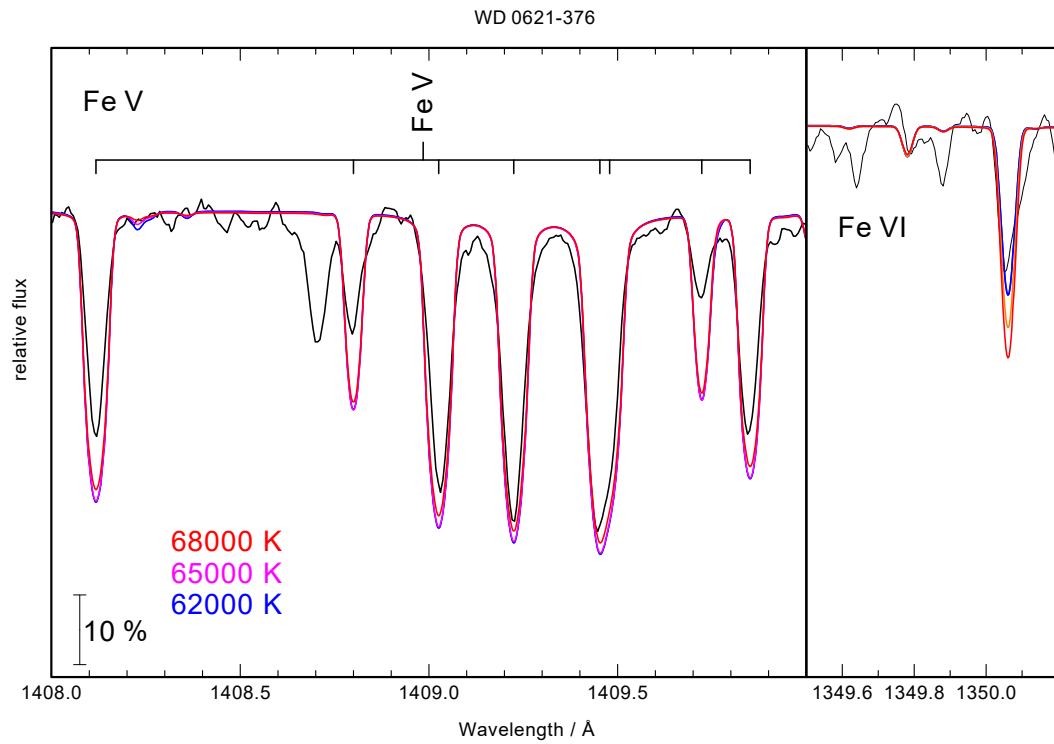


Fig. B.8: Plot to determine the Fe abundance of WD 0621-376. The synthetic spectra with +3 kK and -3 kK with respect to T_{eff} are plotted for comparison

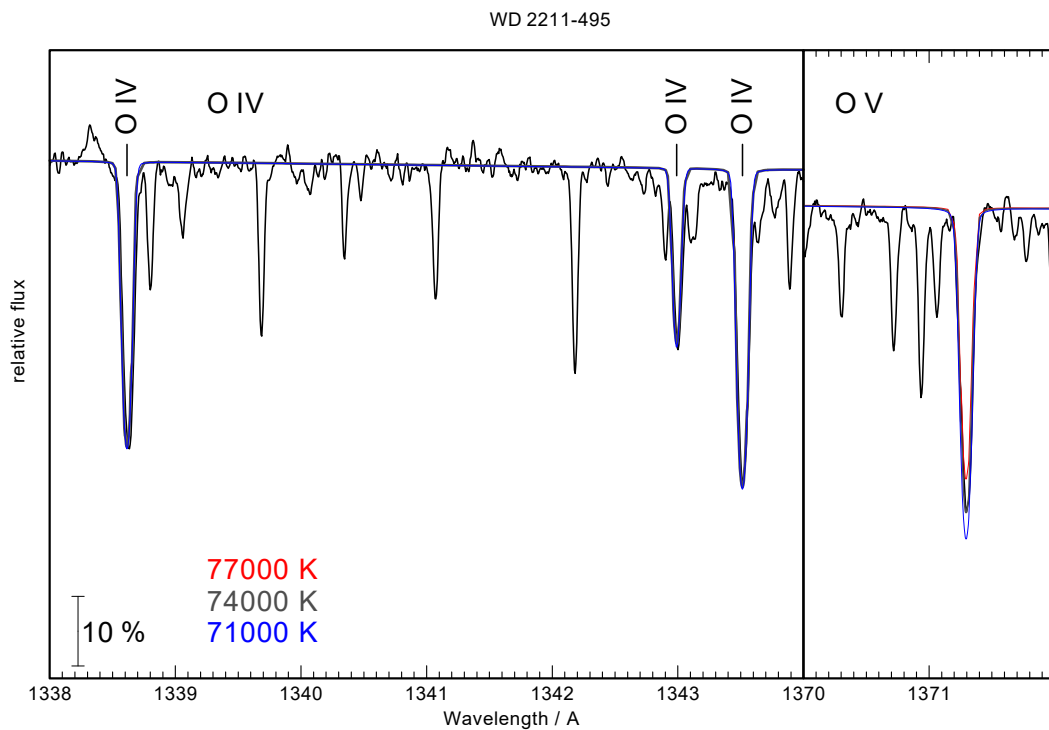


Fig. B.9: Plot to determine the O abundance and T_{eff} of WD 2211-495

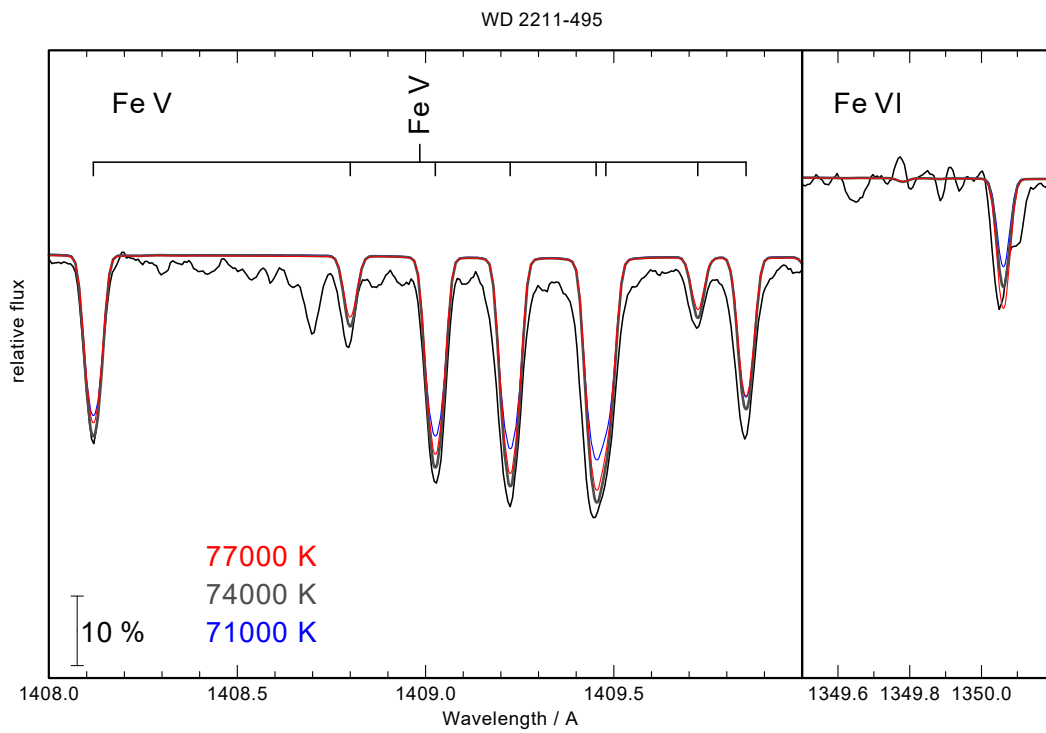


Fig. B.10: Plot to determine the Fe abundance of WD 2211-495. The synthetic spectra with +3 kK and -3 kK with respect to T_{eff} are plotted for comparison

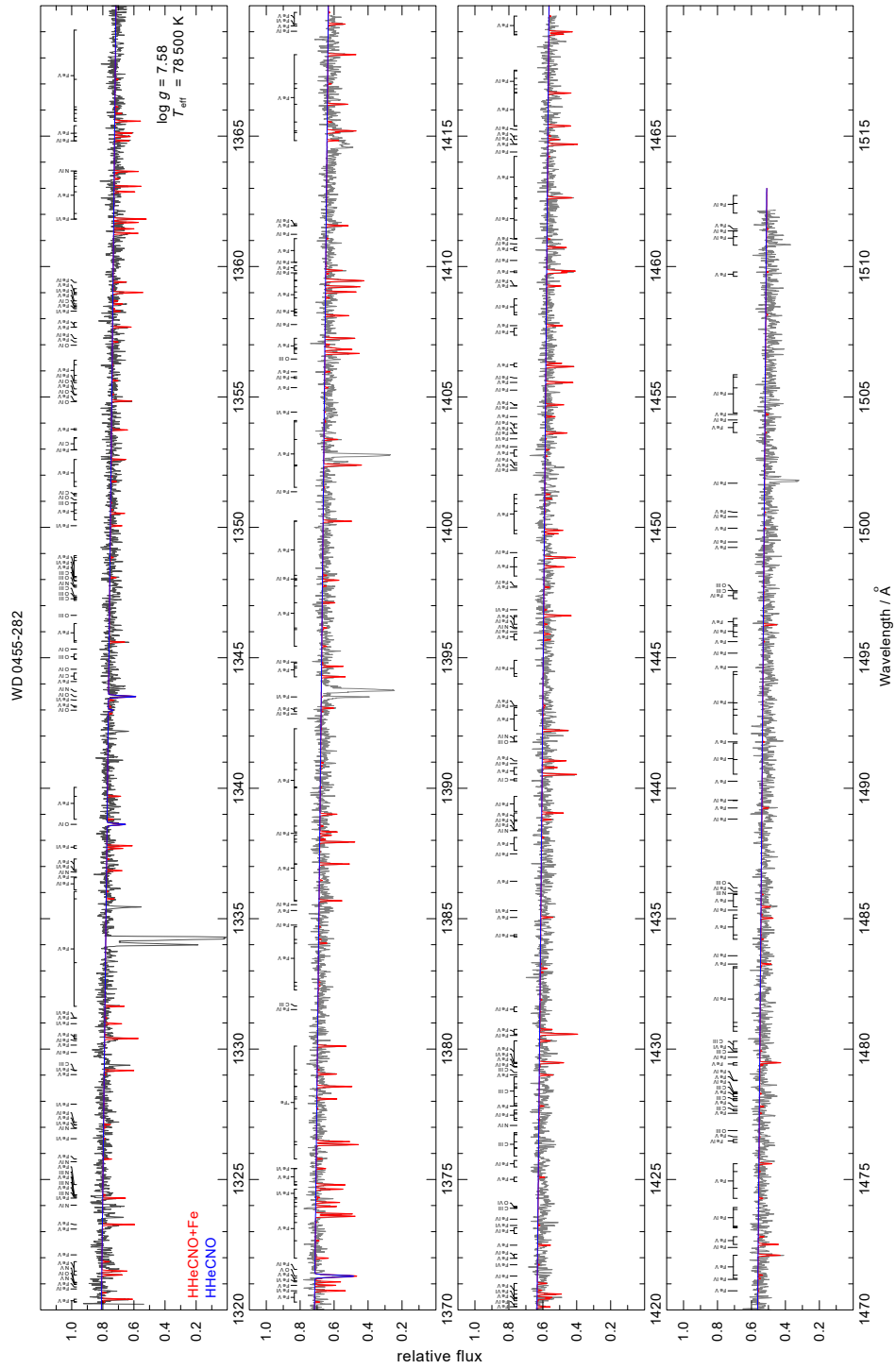


Fig. B.11: Plot of the STIS data presented in Tab. 4.1 of WD 0455-282 with corresponding synthetic spectra

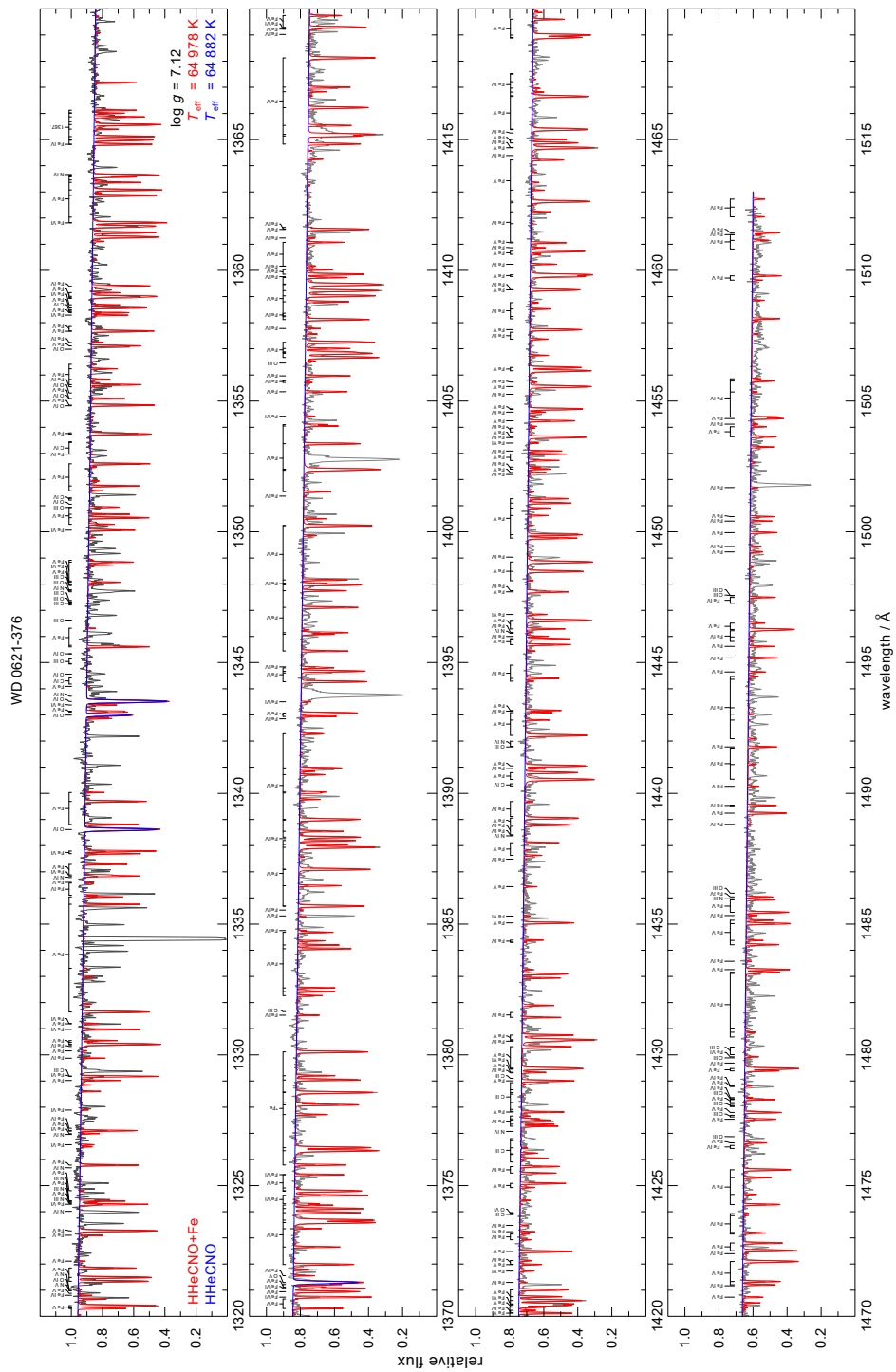


Fig. B.12: Plot of the STIS data listed in Tab. 4.1 of WD0621-376 with corresponding synthetic spectra

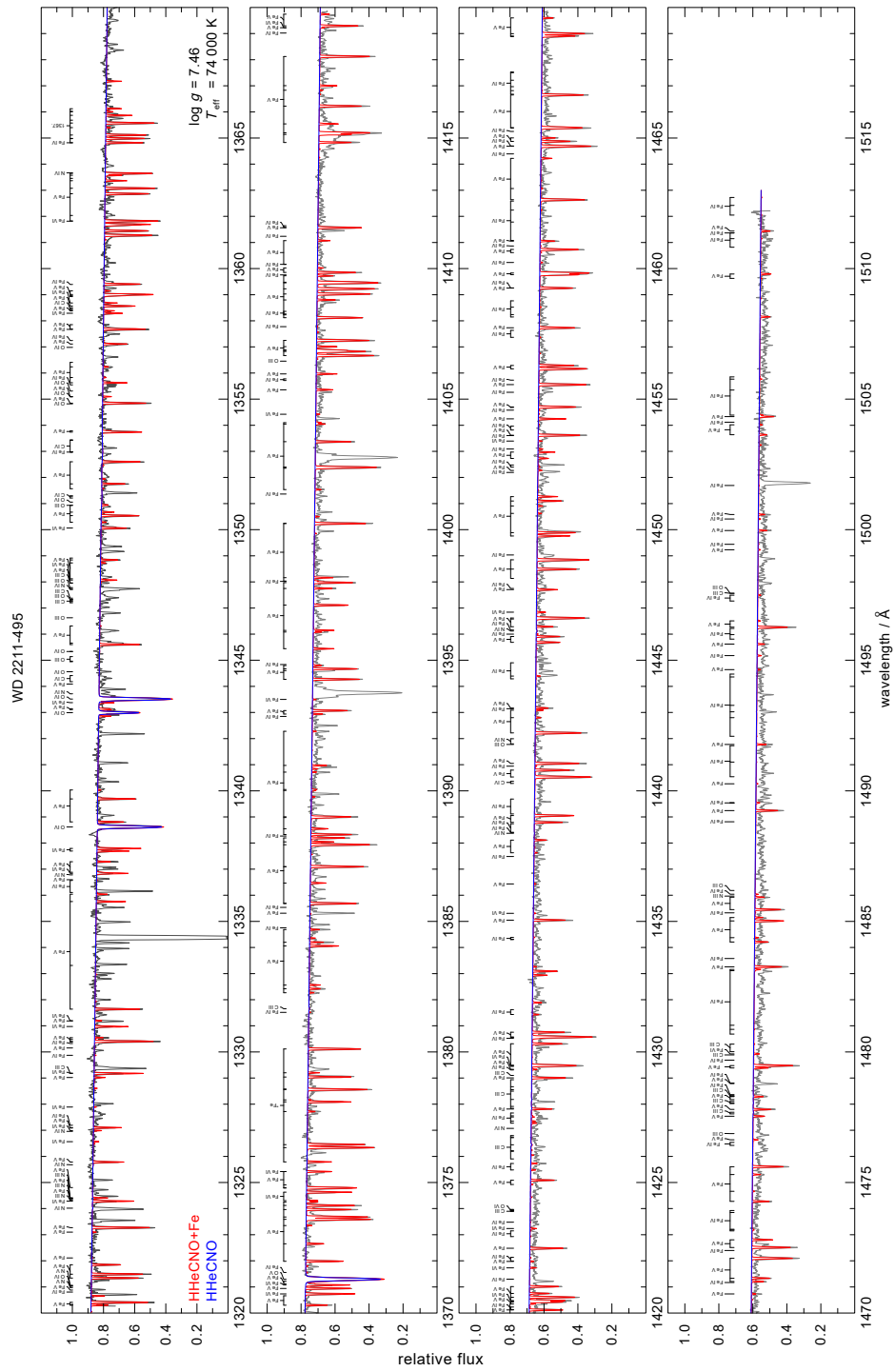


Fig. B.13: Plot of the STIS data given in Tab. 4.1 of WD2211-495 with corresponding synthetic spectra

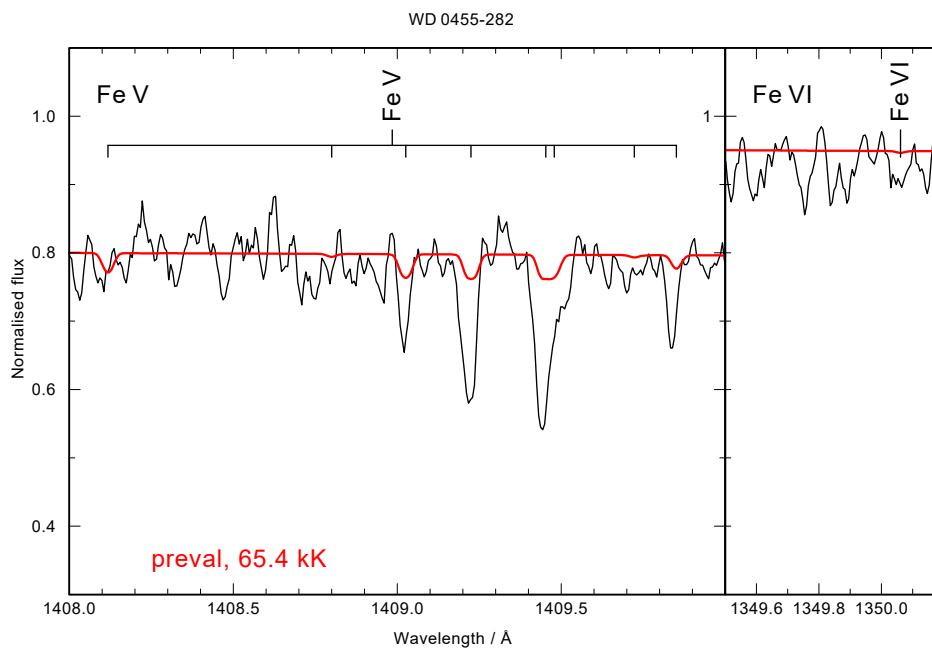


Fig. B.14: Synthetic spectra of a region with Fe lines with parameters from Preval et al. (2019) and observational data of WD 0455-282

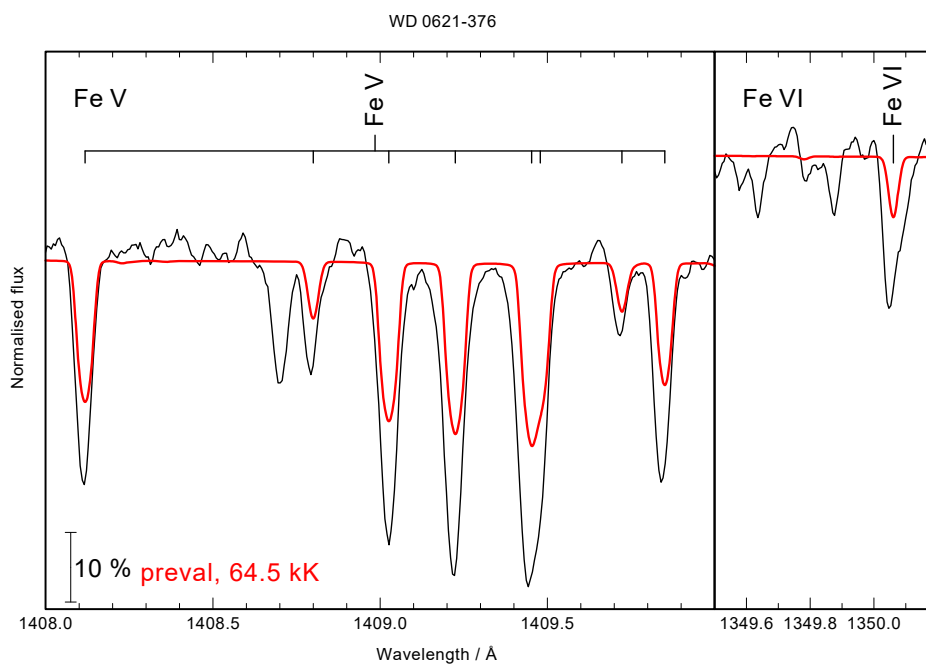


Fig. B.15: Synthetic spectra of a region with Fe lines parameters from Preval et al. (2019) and observational data of WD 0621-376

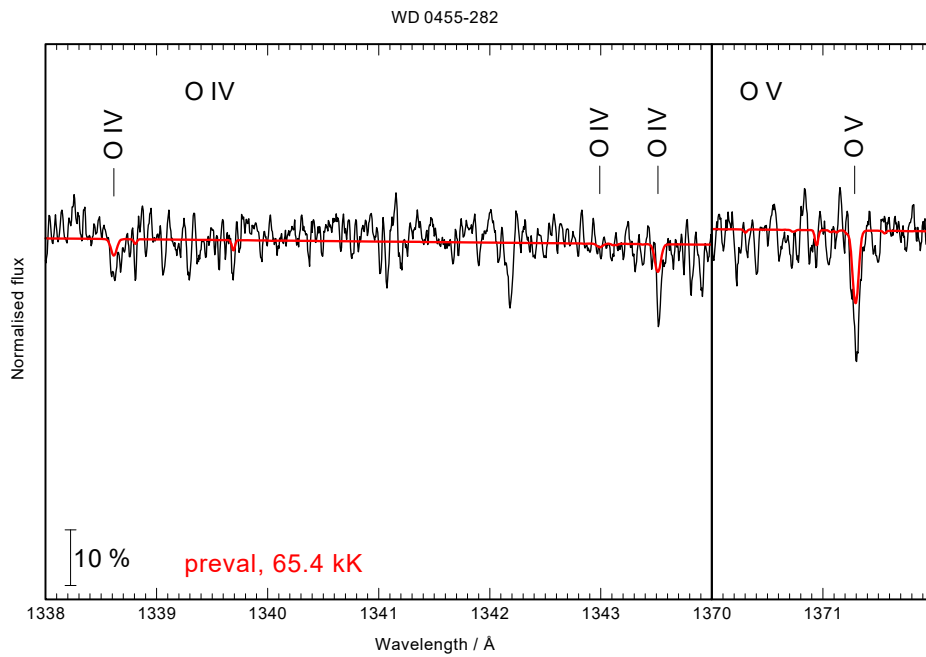


Fig. B.16: Synthetic spectra of a region with O lines parameters from Preval et al. (2019) and observational data of WD 0455-282

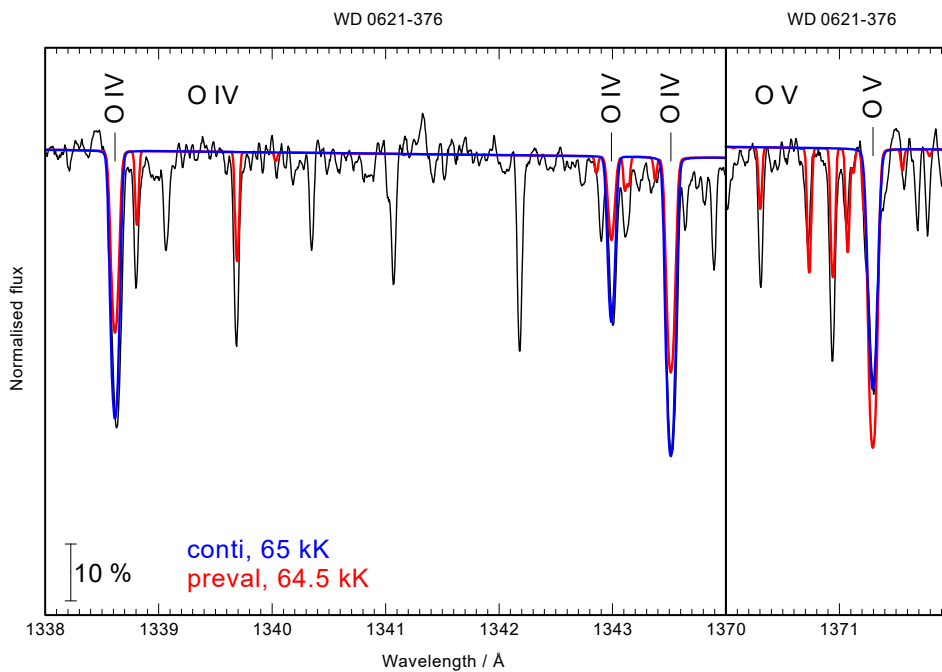


Fig. B.17: Synthetic spectra of a region with O lines parameters from Preval et al. (2019), own parameters and observational data of WD 0621-376

Bibliography

- S. Aslam, R. E. Vest, D. Franz, F. Yan, Y. Zhao, and B. Mott. External quantum efficiency of Pt/n-GaN Schottky diodes in the spectral range 5–500nm. *Nuclear Instruments and Methods in Physics Research Section A: Accelerators, Spectrometers, Detectors and Associated Equipment*, 539(1-2):84–92, Feb. 2005a. doi: 10.1016/j.nima.2004.09.042.
- S. Aslam, F. Yan, D. E. Pugel, D. Franz, L. Miko, F. Herrero, et al. Development of ultra-high sensitivity wide-band gap UV-EUV detectors at NASA goddard space flight center. In S. Fineschi and R. A. Viereck, editors, *Solar Physics and Space Weather Instrumentation*. SPIE, Aug. 2005b. doi: 10.1117/12.639415.
- J. Barnstedt. Entwicklung eines photonenzählenden transportablen Kerasystems für astronomische Anwendungen im sichtbaren Spektralbereich. PhD thesis, Eberhard Karls Universität Tübingen, Apr. 1985.
- J. Barnstedt. Advanced Practical Course - Microchannel plate detectors. Eberhard Karls Universität Tübingen, July 2016. Experiment instructions.
- F. Bloch. Über die Quantenmechanik der Elektronen in Kristallgittern. *Zeitschrift für Physik*, 52(7-8):555–600, 1929. doi: 10.1007/BF01339455.
- S. Bloom, G. Harbeke, E. Meier, and I. B. Ortenburger. Band Structure and Reflectivity of GaN. *physica status solidi (b)*, 66(1):161–168, Nov. 1974. doi: 10.1002/pssb.2220660117.
- M. Born. Quantenmechanik der Stoßvorgänge. *Zeitschrift für Physik*, 38(11-12):803–827, Nov. 1926. doi: 10.1007/BF01397184.

- W. L. Bragg and W. H. Bragg. The structure of some crystals as indicated by their diffraction of X-rays. *Proceedings of the Royal Society of London. Series A, Containing Papers of a Mathematical and Physical Character*, 89 (610):248–277, Sept. 1913. doi: 10.1098/rspa.1913.0083.
- B. W. Carroll and D. A. Ostlie. An Introduction to Modern Astrophysics. Cambridge University Press, Sept. 2017. ISBN 1108422160.
- J. Champion. Photoevaporation of protoplanetary disks by Far-UV photons arising from neighbouring massive stars: observation of proplyds and modeling. *arXiv: Earth and Planetary Astrophysics*, 2019.
- L. Conti, J. Barnstedt, L. Hanke, C. Kalkuhl, N. Kappelmann, T. Rauch, et al. MCP detector development for UV space missions. *Astrophysics and Space Science*, 363(4), Mar. 2018. doi: 10.1007/s10509-018-3283-4.
- L. Conti, J. Barnstedt, S. Buntrock, S. Diebold, L. Hanke, C. Kalkuhl, et al. Microchannel-plate detector development for ultraviolet missions. In J.-W. A. den Herder, S. Nikzad, and K. Nakazawa, editors, *Space Telescopes and Instrumentation 2020: Ultraviolet to Gamma Ray*, volume 11444, pages 94–106. International Society for Optics and Photonics, SPIE, 2020. doi: 10.1117/12.2560663.
- T. Cremer, M. Aviles, C. D. Ertley, M. R. Foley, A. V. Lyashenko, M. J. Minnot, et al. Imaging-quality ALD-GCA-MCPs for high-resolution, large area UV-VIS spectrometers. In A. D. Holland and J. Beletic, editors, *X-Ray, Optical, and Infrared Detectors for Astronomy IX*, volume 11454. International Society for Optics and Photonics, SPIE, 2020. doi: 10.1117/12.2563353.
- I. P. Csorba. Modulation transfer function of image tube lenses. *Applied Optics*, 16(10):2647, Oct. 1977. doi: 10.1364/ao.16.002647.
- R. M. Cutri, M. F. Skrutskie, S. van Dyk, C. A. Beichman, J. M. Carpenter, T. Chester, et al. VizieR Online Data Catalog: 2MASS All-Sky Catalog of Point Sources. *VizieR Online Data Catalog*, art. II/246, June 2003.
- P. Dawson. Quadrupole mass spectrometry and its applications. Elsevier, Amsterdam New York, 1976. ISBN 0444413456.

- J. E. Dickinson Jr and B. R. Wheaton. Processes for polishing glass and glass-ceramic surfaces using excimer laser radiation, Apr. 21 1998. US patent 5 742 026.
- S. Diebold, J. Barnstedt, S. Hermanutz, C. Kalkuhl, N. Kappelmann, M. Pfeifer, et al. UV MCP Detectors for WSO-UV: Cross Strip Anode and Readout Electronics. *IEEE Transactions on Nuclear Science*, 60(2):918–922, 2013. doi: 10.1109/TNS.2013.2248096.
- J. W. Elam, A. U. Mane, J. A. Libera, J. N. Hryn, O. H. W. Siegmund, J. McPhate, et al. Synthesis, characterization, and application of tunable resistance coatings prepared by Atomic Layer Deposition. *ECS Transactions*, 58(10):249–261, 2013. doi: 10.1149/05810.0249ecst.
- C. Ertley, O. Siegmund, T. Cremer, C. Craven, M. Minot, J. Elam, et al. Performance studies of atomic layer deposited microchannel plate electron multipliers. *Nuclear Instruments and Methods in Physics Research Section A: Accelerators, Spectrometers, Detectors and Associated Equipment*, 912:75–77, 2018. doi: 10.1016/j.nima.2017.10.050.
- J. S. Escher. NEA Semiconductor Photoemitters. In *Semiconductors and Semimetals*, volume 15, pages 195–300. Elsevier, 1981. doi: 10.1016/s0080-8784(08)60286-0.
- C. Feng, Y. Zhang, Y. Qian, B. Chang, F. Shi, G. Jiao, et al. Photoemission from advanced heterostructured $\text{Al}_x\text{Ga}_{1-x}\text{As}/\text{GaAs}$ photocathodes under multilevel built-in electric field. *Optics Express*, 23(15):19478, July 2015. doi: 10.1364/oe.23.019478.
- G. W. Fraser. X-ray Detectors in Astronomy. Cambridge Astrophysics. Cambridge University Press, May 1989. ISBN 9780521326636. doi: 10.1017/CBO9780511735554.
- A. Fresnel. Oeuvres complètes d’augustin Fresnel. Imprimerie impériale, 1868.
- W. Friedrich, P. Knipping, and M. Laue. Interferenzerscheinungen bei Röntgenstrahlen. *Annalen der Physik*, 346(10):971–988, 1913. doi: 10.1002/andp.19133461004.

- X.-Q. Fu, B.-K. Chang, X.-H. Wang, B. Li, Y.-J. Du, and J.-J. Zhang. Photoemission of graded-doping GaN photocathode. *Chinese Physics B*, 20(3): 037902, Mar. 2011. doi: 10.1088/1674-1056/20/3/037902.
- Gaia Collaboration, A. G. A. Brown, A. Vallenari, T. Prusti, J. H. J. de Bruijne, C. Babusiaux, et al. Gaia Data Release 2. Summary of the contents and survey properties. *Astronomy and Astrophysics*, 616:A1, Aug. 2018. doi: 10.1051/0004-6361/201833051.
- S. M. George. Atomic Layer Deposition: An Overview. *Chemical Reviews*, 110(1):111–131, 2010. doi: 10.1021/cr900056b.
- A. Gianninas, P. Bergeron, and M. T. Ruiz. A spectroscopic survey and analysis of bright, hydrogen-rich white dwarfs. *The Astrophysical Journal*, 743(2):138, Nov. 2011. doi: 10.1088/0004-637x/743/2/138.
- N. Gogurla, A. K. Sinha, S. Santra, S. Manna, and S. K. Ray. Multifunctional Au-ZnO plasmonic nanostructures for enhanced UV photodetector and room temperature NO sensing devices. *Scientific Reports*, 4(1):6483, Sept. 2014. doi: 10.1038/srep06483.
- D. A. Gollmer, C. Lorch, F. Schreiber, D. P. Kern, and M. Fleischer. Shaping and polarizing fluorescence emission of a polycrystalline organic semiconductor film by plasmonic nanogratings. *Journal of the Optical Society of America B: Optical Physics*, 36(7):E9–E14, July 2019. doi: 10.1364/JOSAB.36.0000E9.
- S. B. Gudennavar, S. G. Bubbly, K. Preethi, and J. Murthy. A compilation of interstellar column densities. *The Astrophysical Journal Supplement Series*, 199(1):8, Feb. 2012. doi: 10.1088/0067-0049/199/1/8.
- T.-H. Han, Y. Lee, M.-R. Choi, S.-H. Woo, S.-H. Bae, B. H. Hong, et al. Extremely efficient flexible organic light-emitting diodes with modified graphene anode. *Nature Photonics*, 6(2):105–110, Jan. 2012. doi: 10.1038/nphoton.2011.318.
- L. Hanke. Optimierung des Auswertungsalgorithmus für einen UV-MCP-Detektor. Master's thesis, Eberhard Karls Universität Tübingen, 2018.

- S. Hermanutz. Untersuchungen zur Beschichtung von Tscherenkow-Teleskop-Spiegeln am Beispiel von H.E.S.S. Master's thesis, Eberhard Karls Universität Tübingen, 2011.
- S. Hermanutz. Entwicklung von Cs₂Te Photokathoden für UV-Detektoren. PhD thesis, Eberhard Karls Universität Tübingen, 2015.
- S. D. Hersee, X. Sun, and X. Wang. The Controlled Growth of GaN Nanowires. *Nano Letters*, 6(8):1808–1811, Aug. 2006. doi: 10.1021/nl060553t.
- J. Hildebrand, K. Hecht, J. Bliedtner, and H. Müller. Laser Beam Polishing of Quartz Glass Surfaces. *Physics Procedia*, 12:452–461, 2011. doi: 10.1016/j.phpro.2011.03.056.
- E. Høg, C. Fabricius, V. V. Makarov, S. Urban, T. Corbin, G. Wycoff, et al. The Tycho-2 catalogue of the 2.5 million brightest stars. *Astronomy and Astrophysics*, 355:L27–L30, Mar. 2000.
- J. R. Howorth, A. L. Harmer, E. W. L. Trawny, R. Holtom, and C. J. R. Sheppard. Electric field enhancement of escape probability on negative-electron-affinity surfaces. *Applied Physics Letters*, 23(3):123–124, Aug. 1973. doi: 10.1063/1.1654828.
- I. Hubeny and D. Mihalas. *Theory of Stellar Atmospheres*. Princeton University Press, 2014. ISBN 0691163294.
- W. R. Hunter. Optical Constants of Metals in the Extreme Ultraviolet. II. Optical Constants of Aluminum, Magnesium, and Indium at Wavelengths Shorter than Their Critical Wavelengths. *Journal of the Optical Society of America*, 54(2):208–212, Feb. 1964. doi: 10.1364/JOSA.54.000208.
- W. R. Hunter and S. A. Malo. The temperature dependence of the short wavelength transmittance limit of vacuum ultraviolet window materials—I. Experiment. *Journal of Physics and Chemistry of Solids*, 30(12):2739–2745, Dec. 1969. doi: 10.1016/0022-3697(69)90047-x.
- Y. Ishigami, K. Akiyama, T. Nagata, K. Kato, T. Ihara, K. Nakamura, et al. Development of a high-sensitivity UV photocathode using GaN film that works in transmission mode. In E. M. Carapezza, editor, *Sensors, and*

- Command, Control, Communications, and Intelligence (C3I) Technologies for Homeland Security and Homeland Defense XI*. SPIE, May 2012. doi: 10.1117/12.918396.
- L. Jianjun, Y. Jinliang, S. Liang, and L. Ting. Electrical and optical properties of deep ultraviolet transparent conductive Ga₂O₃/ITO films by magnetron sputtering. *Journal of Semiconductors*, 31(10):103001, Oct. 2010. doi: 10.1088/1674-4926/31/10/103001.
- P. B. Johnson and R. W. Christy. Optical Constants of the Noble Metals. *Physical Review B*, 6:4370–4379, Dec. 1972. doi: 10.1103/PhysRevB.6.4370.
- P. B. Johnson and R. W. Christy. Optical constants of transition metals: Ti, V, Cr, Mn, Fe, Co, Ni, and Pd. *Physical Review B*, 9:5056–5070, June 1974. doi: 10.1103/PhysRevB.9.5056.
- S. J. Jokela, I. V. Veryovkin, A. V. Zinovev, J. W. Elam, A. U. Mane, Q. Peng, et al. Secondary Electron Yield of Emissive Materials for Large-Area Micro-Channel Plate Detectors: Surface Composition and Film Thickness Dependencies. *Physics Procedia*, 37:740–747, 2012. doi: 10.1016/j.phpro.2012.03.718.
- T. Kawashima, H. Yoshikawa, S. Adachi, S. Fuke, and K. Ohtsuka. Optical properties of hexagonal GaN. *Journal of Applied Physics*, 82(7):3528–3535, Oct. 1997. doi: 10.1063/1.365671.
- J. Kim, M. Zukic, J. H. Park, M. W. McColgan, C. E. Keffer, and D. G. Torr. Transparent conductive coatings in the far ultraviolet. In S. Fineschi, editor, *X-Ray and Ultraviolet Polarimetry*, volume 2010, pages 220–227. International Society for Optics and Photonics, SPIE, 1994. doi: 10.1117/12.168585.
- C. Kittel. *Einführung in die Festkörperphysik*. Oldenbourg Wissenschaftsverlag, 2013. ISBN 9783486597554.
- G. Krämer, J. Barnstedt, N. Eberhard, M. Grewing, W. Gringel, C. Haas, et al. Far and Extreme Ultraviolet Astronomy with ORFEUS. *International Astronomical Union Colloquium*, 123:177–184, 1990. doi: 10.1017/S0252921100077010.

- A. Lehmann, A. Britting, W. Eyrich, M. Pfaffinger, F. Uhlig, A. Belias, et al. Tremendously increased lifetime of MCP-PMTs. *Nuclear Instruments and Methods in Physics Research Section A: Accelerators, Spectrometers, Detectors and Associated Equipment*, 845:570–574, 2017. doi: 10.1016/j.nima.2016.05.017.
- D. Li, X. Sun, H. Song, Z. Li, Y. Chen, H. Jiang, et al. Realization of a High-Performance GaN UV Detector by Nanoplasmonic Enhancement. *Advanced Materials*, 24(6):845–849, 2012. doi: 10.1002/adma.201102585.
- L. Lin, Y. Ou, X. Zhu, E. Stamate, K. Wu, M. Liang, et al. InGaN/GaN ultraviolet LED with a graphene/AZO transparent current spreading layer. *Opt. Mater. Express*, 8(7):1818–1826, July 2018. doi: 10.1364/OME.8.001818.
- S. Löchner. Development, Optimisation and Characterisation of a Radiation Hard Mixed-Signal Readout Chip for LHCb. PhD thesis, Max-Planck-Institut für Kernphysik Heidelberg, 2006.
- S. Löchner and M. Schmelling. The Beetle Reference Manual - chip version 1.3, 1.4 and 1.5. Technical Report LHCb-2005-105. CERN-LHCb-2005-105, CERN, Geneva, Nov. 2006.
- F. Machuca and Z. Liu. Fabrication of group III-nitride photocathode having Cs activation layer, Nov. 2008. US patent 7 455 565 B2.
- F. Machuca, Z. Liu, Y. Sun, P. Pianetta, W. E. Spicer, and R. F. W. Pease. Simple method for cleaning gallium nitride (0001). *Journal of Vacuum Science & Technology A: Vacuum, Surfaces, and Films*, 20(5):1784–1786, Sept. 2002. doi: 10.1116/1.1503782.
- F. Machuca, Z. Liu, Y. Sun, P. Pianetta, W. E. Spicer, and R. F. W. Pease. Oxygen species in Cs/O activated gallium nitride (GaN) negative electron affinity photocathodes. *Journal of Vacuum Science & Technology B: Microelectronics and Nanometer Structures*, 21(4):1863, 2003. doi: 10.1116/1.1589512.
- P. Maier, J. Wolf, T. Keilig, A. Krabbe, R. Duffard, J.-L. Ortiz, et al. Towards a European Stratospheric Balloon Observatory: the ESBO design study.

- In H. K. Marshall and J. Spyromilio, editors, *Ground-based and Airborne Telescopes VII*, volume 10700, pages 1470–1481. International Society for Optics and Photonics, SPIE, 2018. doi: 10.1117/12.2319248.
- A. U. Mane and J. W. Elam. Nanostructured composite thin films with tailored resistivity by atomic layer deposition. In T. G. Mackay, A. Lakhtakia, Y.-J. Jen, and M. Suzuki, editors, *Nanostructured Thin Films VI*, volume 8818, pages 110–116. International Society for Optics and Photonics, SPIE, 2013. doi: 10.1117/12.2024482.
- J. Marini, L. D. Bell, and F. Shahedipour-Sandvik. Monte Carlo simulation of III-nitride photocathodes. *Journal of Applied Physics*, 123(12):124502, Mar. 2018a. doi: 10.1063/1.5022200.
- J. Marini, I. Mahaboob, E. Rocco, L. D. Bell, and F. Shahedipour-Sandvik. Polarization engineered N-polar Cs-free GaN photocathodes. *Journal of Applied Physics*, 124(11):113101, Sept. 2018b. doi: 10.1063/1.5029975.
- C. Martin, P. Jelinsky, M. Lampton, R. F. Malina, and H. O. Anger. Wedge-and-strip anodes for centroid-finding position-sensitive photon and particle detectors. *Review of Scientific Instruments*, 52(7):1067–1074, 1981. doi: 10.1063/1.1136710.
- P. Merz, H. J. Quenzer, H. Bernt, B. Wanger, and M. Zoberbier. A novel micromachining technology for structuring borosilicate glass substrates. In *TRANSDUCERS '03. 12th International Conference on Solid-State Sensors, Actuators and Microsystems*, volume 1, pages 258–261. IEEE, 2003. doi: 10.1109/SENSOR.2003.1215302.
- K. Meyer, J. Barnstedt, L. Conti, L. Hanke, C. Kalkuhl, N. Kappelmann, et al. GaN films grown on (001) and (110) MgF₂ substrates by plasma-assisted molecular beam epitaxy (PA-MBE). *Journal of Crystal Growth*, 531:125303, 2020a. doi: 10.1016/j.jcrysgro.2019.125303.
- K. Meyer, M. Buchholz, D. Uxa, L. Dörrer, H. Schmidt, and D. M. Schaadt. X-ray diffraction and secondary ion mass spectrometry investigations of GaN

- films grown on (001) and (110) MgF_2 substrates by plasma-assisted molecular beam epitaxy (PA-MBE). *Materials Science in Semiconductor Processing*, 119:105262, Nov. 2020b. doi: 10.1016/j.mssp.2020.105262.
- D. G. Monet, S. E. Levine, B. Canzian, H. D. Ables, A. R. Bird, C. C. Dahn, et al. The USNO-B Catalog. *The Astronomical Journal*, 125(2):984–993, Feb. 2003. doi: 10.1086/345888.
- J. F. Muth, J. D. Brown, M. A. L. Johnson, Z. Yu, R. M. Kolbas, J. W. Cook, et al. Absorption Coefficient and Refractive Index of GaN, AlN and AlGaIn Alloys. *MRS Internet Journal of Nitride Semiconductor Research*, 4(S1): 502–507, 1999. doi: 10.1557/s1092578300002957.
- S.-I. Na, S.-S. Kim, J. Jo, and D.-Y. Kim. Efficient and Flexible ITO-Free Organic Solar Cells Using Highly Conductive Polymer Anodes. *Advanced Materials*, 20(21):4061–4067, 2008. doi: 10.1002/adma.200800338.
- K. K. Ng. Complete Guide to Semiconductor Devices. Wiley - IEEE. Wiley, 2002. ISBN 9780471202400.
- T. J. Norton, B. E. Woodgate, J. Stock, G. Hilton, M. P. Ulmer, S. Aslam, et al. Results from Cs activated GaN photocathode development for MCP detector systems at NASA GSFC. In O. H. W. Siegmund, editor, *UV/EUV and Visible Space Instrumentation for Astronomy II*, volume 5164, pages 155–164. International Society for Optics and Photonics, SPIE, 2003. doi: 10.1117/12.507528.
- D. A. Orlov, R. Glazenberg, R. Ortega, and E. Kernen. UV/visible high-sensitivity MCP-PMT single-photon GHz counting detector for long-range lidar instrumentations. *CEAS Space Journal*, 11(4):405–411, June 2019. doi: 10.1007/s12567-019-00260-0.
- A. Pahler, M. Ångermann, J. Barnstedt, S. Bougueroua, A. Colin, L. Conti, et al. Status of the STUDIO UV balloon mission and platform. In H. K. Marshall, J. Spyromilio, and T. Usuda, editors, *Ground-based and Airborne Telescopes VIII*, volume 11445, pages 416–430. International Society for Optics and Photonics, SPIE, 2020. doi: 10.1117/12.2575932.

- S. J. Pearton, F. Ren, E. Patrick, M. E. Law, and A. Y. Polyakov. Ionizing radiation damage effects on GaN devices. *ECS Journal of Solid State Science and Technology*, 5(2):Q35–Q60, Nov. 2015. doi: 10.1149/2.0251602jss.
- M. Pfeifer, J. Barnstedt, S. Diebold, S. Hermanutz, C. Kalkuhl, N. Kappelmann, et al. Characterisation of low power readout electronics for a UV microchannel plate detector with cross-strip readout. In T. Takahashi, J.-W. A. den Herder, and M. Bautz, editors, *Space Telescopes and Instrumentation 2014: Ultraviolet to Gamma Ray*, volume 9144, pages 1002–1009. International Society for Optics and Photonics, SPIE, 2014. doi: 10.1117/12.2054742.
- A. Polyakov, C. Senft, K. F. Thompson, J. Feng, S. Cabrini, P. J. Schuck, et al. Plasmon-Enhanced Photocathode for High Brightness and High Repetition Rate X-Ray Sources. *Physical Review Letters*, 110:076802, Feb. 2013. doi: 10.1103/PhysRevLett.110.076802.
- M. A. Popecki, B. Adams, C. A. Craven, T. Cremer, M. R. Foley, A. Lyashenko, et al. Microchannel plate fabrication using glass capillary arrays with Atomic Layer Deposition films for resistance and gain. *Journal of Geophysical Research: Space Physics*, 121(8):7449–7460, 2016. doi: 10.1002/2016JA022580.
- S. P. Preval, M. A. Barstow, M. Bainbridge, N. Reindl, T. Ayres, J. B. Holberg, et al. A far-UV survey of three hot, metal-polluted white dwarf stars: WD0455-282, WD0621-376, and WD2211-495. *Monthly Notices of the Royal Astronomical Society*, 487(3):3470–3487, June 2019. doi: 10.1093/mnras/stz1506.
- D. Qiao, L. S. Yu, S. S. Lau, J. Y. Lin, H. X. Jiang, and T. E. Haynes. A study of the Au/Ni ohmic contact on p-GaN. *Journal of Applied Physics*, 88(7):4196, 2000. doi: 10.1063/1.1311809.
- I. Ramírez, A. T. Bajkova, V. V. Bobylev, I. U. Roederer, D. L. Lambert, M. Endl, et al. Elemental abundances of solar sibling candidates. *The Astrophysical Journal*, 787(2):154, May 2014. doi: 10.1088/0004-637x/787/2/154.
- T. Rauch, P. Quinet, D. Hoyer, K. Werner, P. Richter, J. W. Kruk, et al.

- Stellar laboratories. *Astronomy & Astrophysics*, 590:A128, May 2016. doi: 10.1051/0004-6361/201628131.
- I. Renedo, L. G. Althaus, M. M. M. Bertolami, A. D. Romero, A. H. Córscico, R. D. Rohrmann, et al. New cooling sequences for old white dwarfs. *The Astrophysical Journal*, 717(1):183–195, June 2010. doi: 10.1088/0004-637x/717/1/183.
- M. Ritala, M. Leskelä, J.-P. Dekker, C. Mutsaers, P. J. Soininen, and J. Skarp. Perfectly Conformal TiN and Al₂O₃ Films Deposited by Atomic Layer Deposition. *Chemical Vapor Deposition*, 5(1):7–9, Jan. 1999. doi: 10.1002/(sici)1521-3862(199901)5:1<7::aid-cvde7>3.0.co;2-j.
- L. V. Rodríguez-de Marcos, J. I. Larruquert, J. A. Méndez, and J. A. Aznárez. Self-consistent optical constants of MgF₂, LaF₃, and CeF₃ films. *Opt. Mater. Express*, 7(3):989–1006, Mar. 2017. doi: 10.1364/OME.7.000989.
- P. Roth and G. W. Fraser. Microchannel plate resistance at cryogenic temperatures. *Nuclear Instruments and Methods in Physics Research, Section A: Accelerators, Spectrometers, Detectors, and Associated Equipment*, 439(1):134–137, 2000. doi: 10.1016/S0168-9002(99)00792-5.
- E. R. Schindhelm, J. C. Green, O. H. W. Siegmund, C. Ertley, B. T. Fleming, K. C. France, et al. Microchannel plate detector technology potential for LUVOIR and HabEx. *UV, X-Ray, and Gamma-Ray Space Instrumentation for Astronomy XX*, Aug. 2017. doi: 10.1117/12.2274281.
- E. F. Schlafly and D. P. Finkbeiner. Measuring reddening with Sloan Digital Sky Survey stellar spectra and recalibrating SFD. *The Astrophysical Journal*, 737(2):103, Aug. 2011. doi: 10.1088/0004-637x/737/2/103.
- O. H. W. Siegmund, A. S. Tremsin, A. Martin, J. Malloy, M. P. Ulmer, and B. Wessels. GaN photocathodes for UV detection and imaging. In O. H. W. Siegmund, editor, *UV/EUV and Visible Space Instrumentation for Astronomy II*. SPIE, Dec. 2003. doi: 10.1117/12.510429.
- O. H. W. Siegmund, A. S. Tremsin, J. V. Vallerga, J. B. McPhate, J. S. Hull, J. Malloy, et al. Gallium nitride photocathode development for imaging

- detectors. In D. A. Dorn and A. D. Holland, editors, *High Energy, Optical, and Infrared Detectors for Astronomy III*. SPIE, Aug. 2008. doi: 10.1117/12.790076.
- L. L. Smith, S. W. King, R. J. Nemanich, and R. F. Davis. Cleaning of GaN surfaces. *Journal of Electronic Materials*, 25(5):805–810, May 1996. doi: 10.1007/bf02666640.
- W. E. Spicer. Photoemissive, Photoconductive, and Optical Absorption Studies of Alkali-Antimony Compounds. *Physical Review*, 112(1):114–122, Oct. 1958. doi: 10.1103/PhysRev.112.114.
- W. E. Spicer and A. Herrera-Gomez. Modern theory and applications of photocathodes. In K. J. Kaufmann, editor, *Photodetectors and Power Meters*. SPIE, Oct. 1993. doi: 10.1117/12.158575.
- J. Stock, G. Hilton, T. Norton, B. Woodgate, S. Aslam, and M. Ulmer. Progress on development of UV photocathodes for photon-counting applications at NASA GSFC. In O. H. W. Siegmund, editor, *UV, X-Ray, and Gamma-Ray Space Instrumentation for Astronomy XIV*. SPIE, Aug. 2005. doi: 10.1117/12.617517.
- V. L. Stout and M. D. Gibbons. Gettering of Gas by Titanium. *Journal of Applied Physics*, 26(12):1488–1492, 1955. doi: 10.1063/1.1721936.
- A. S. Tremsin, O. H. W. Siegmund, J. V. Vallerga, J. S. Hull, and R. Abiad. Cross-strip readouts for photon counting detectors with high spatial and temporal resolution. *IEEE Transactions on Nuclear Science*, 51(4):1707–1711, Aug. 2004. doi: 10.1109/TNS.2004.832987.
- Y. P. Varshni. Temperature dependence of the energy gap in semiconductors. *Physica*, 34(1):149–154, Jan. 1967. doi: 10.1016/0031-8914(67)90062-6.
- F. Vega, N. B. Lupon, J. Armengol, and F. Laguarda. Laser application for optical glass polishing. *Optical Engineering*, 37:272–279, Jan. 1998. doi: 10.1117/1.601614.
- S. Vennes, P. Chayer, M. Hurwitz, and S. Bowyer. Discovery of photospheric sulfur and phosphorus in ORFEUS spectra of the hot white dwarfs g191-b2b

- and MCT o455-2812. *The Astrophysical Journal*, 468:898, Sept. 1996. doi: 10.1086/177745.
- S. Vennes, P. Chayer, J. Dupuis, and T. Lanz. Iron in hot DA white dwarfs. *The Astrophysical Journal*, 652(2):1554–1562, Dec. 2006. doi: 10.1086/508509.
- K. Werner. Construction of non-LTE model atmospheres using approximate lambda operators. *Astronomy and Astrophysics*, 161:177–182, June 1986.
- K. Werner and S. Dreizler. The classical stellar atmosphere problem. *Journal of Computational and Applied Mathematics*, 109(1):65–93, 1999. ISSN 0377-0427. doi: 10.1016/S0377-0427(99)00154-5.
- J. L. Wiza. Microchannel plate detectors. *Nuclear Instruments and Methods*, 162(1):587–601, 1979. doi: 10.1016/0029-554X(79)90734-1.
- C. I. Wu and A. Kahn. Electronic states and effective negative electron affinity at cesiated p-GaN surfaces. *Journal of Applied Physics*, 86(6):3209–3212, Sept. 1999. doi: 10.1063/1.371191.
- S. Xia, L. Liu, Y. Kong, and M. Wang. Uniaxial strain effects on the optoelectronic properties of GaN nanowires. *Superlattices and Microstructures*, 97: 327–334, Sept. 2016. doi: 10.1016/j.spmi.2016.06.040.
- S. Xia, L. Liu, Y. Diao, and S. Feng. Research on quantum efficiency and photoemission characteristics of exponential-doping GaN nanowire photocathode. *Journal of Materials Science*, 52(21):12795–12805, July 2017. doi: 10.1007/s10853-017-1394-x.
- J. Yang, F. Luo, T. S. Kao, X. Li, G. W. Ho, J. Teng, et al. Design and fabrication of broadband ultralow reflectivity black Si surfaces by laser micro/nanoprocessing. *Light: Science & Applications*, 3(7):e185–e185, July 2014. doi: 10.1038/lssa.2014.66.
- T. Young. An essay on the cohesion of fluids. *Philosophical Transactions of the Royal Society of London*, 95:65–87, Dec. 1805. doi: 10.1098/rstl.1805.0005.
- Y. Yuan and T. R. Lee. Contact Angle and Wetting Properties. Springer, Berlin, Heidelberg, 2013. ISBN 9783642342431. doi: 10.1007/978-3-642-34243-1_1.

- N. Zacharias, C. T. Finch, T. M. Girard, A. Henden, J. L. Bartlett, D. G. Monet, et al. VizieR Online Data Catalog: UCAC4 Catalogue. *VizieR Online Data Catalog*, art. I/322A, July 2012.
- C. Zener. Remarkable optical properties of the alkali metals. *Nature*, 132 (3347):968–968, Dec. 1933. doi: 10.1038/132968a0.
- D.-x. Zhou, E. Parrott, D. Paul, and J. Zeitler. Determination of complex refractive index of thin metal films from terahertz time-domain spectroscopy. *Journal of Applied Physics*, 104:053110–053110, Oct. 2008. doi: 10.1063/1.2970161.

Danksagung

Der in dieser Arbeit vorgestellte Detektor ist ein Gemeinschaftswerk, das nur durch gute Zusammenarbeit im Team den aktuellen Entwicklungsstand erreichen konnte. Viele in der Dissertation vorgestellte Ergebnisse stellen die Fortführung von bereits geleisteter, oftmals eindrucksvoller Arbeit dar. Zudem war ich vom ersten Tag an fasziniert von den komplexen, exzellenten, aber auch meist sehr teuren Vakuumanlagen und Geräten, die für so eine Detektorentwicklung benötigt werden. Zunächst möchte mich bei folgenden Personen für ihren Beitrag bei dieser Arbeit bedanken:

- Prof. Dr. Klaus Werner dafür, dass ich in dieser produktiven und gleichzeitig harmonisch zusammenarbeitenden Arbeitsgruppe meine Dissertation verfassen durfte. Für nicht nur eine offene Türe, sondern auch ein offenes Ohr und die stetige und geduldige Begleitung beim Verfassen dieser Arbeit. Ebenso danke ich Prof. Dott. Andrea Santangelo, der diese Dissertation als zweiter Gutachter betreut hat.
- Dr. Jürgen Barnstedt, der seinen enormen Erfahrungsschatz bei der Detektorentwicklung stets tatkräftig geteilt hat und in sehr vielen Bereichen eine große Hilfe war. Viele der praktischen Arbeiten im UHV-Labor wurden mit ihm durchgeführt, viele der Erfolge sind nicht zuletzt auch seiner vorbildhaften analytischen Herangehensweise zu verdanken.
- Dr. Norbert Kappelmann dafür, dass er die Erfolge in der Detektorentwicklung in neue interessante Projekte umgemünzt hat. Seine Erfahrungen sind nicht nur inspirierend, sondern waren an vielen Stellen sehr wertvoll für die Projektarbeit und Dissertation. Seinen Einsatz für das Team und mich habe ich immer sehr geschätzt.
- Dr. Thomas Rauch für seine Einführung und geduldige Hilfe bei der Erstellung der Sternatmosphärenmodelle. Er hat zudem nicht nur die administrativen Aufgaben übernommen, die bei so einer Arbeit mitunter häufig anfallen, sondern neben seinen vielen anderen Aufgaben auch eine krankheitsbedingt ausgefallene Stelle fast vollständig aufgefangen, so dass ich mich weiter auf meine Arbeit konzentrieren konnte.

- Dr. Sebastian Diebold, über dessen Neuankunft in der UV Detektorgruppe ich mich besonders freue. Von seinen Anmerkungen zur letzten Publikation bin ich nachhaltig beeindruckt, und habe vieles was ich von ihm lernen konnte bereits in dieser Arbeit umgesetzt.
- Dem „Team UV-MCP-Detektor“ danke ich für die gute Zusammenarbeit: Prof. Dr. Beate Stelzer, Christoph Kalkuhl, Lars Hanke, Thomas Schanz, Sebastian Buntrock, Thomas Kaufmann. Dr. Stephan Hermannutz danke ich für die umfassende Dokumentation seiner Arbeit. Zudem den Mitarbeiterinnen und Mitarbeitern der feinmechanischen Werkstatt, insbesondere Siegbert Renner, Sonja Riekert und Andrej Korneev, die mit großem Einsatz und Fachkenntnis eine Vielzahl von Einzelteilen gefertigt haben, die für die Detektorentwicklung unabdingbar waren.
- Den Kollegen an der TU Claustal, Prof. Dr. Daniel M. Schaadt, Kevin Meyer und Martin Buchholz. Nur dank ihres großen Einsatzes konnten die Fortschritte in Bezug auf die GaN-Proben erzielt werden. Alle umgesetzten Ideen zum Thema GaN sind in gegenseitiger Absprache erzielt worden, alle Ergebnisse wurden schon mit Spannung erwartet und evaluiert. Für die gute Arbeitsatmosphäre und natürlich die Herstellung der GaN-Schichten bedanke ich mich herzlich.
- Den Kollegen von der Universität Stuttgart, bei denen als „USTUTT“ beim ESBO *DS* Projekt die Fäden zusammen liefen und allen anderen Kollegen des Projekts aus ganz Europa. Das Projekt zu begleiten ist ein großer Erfahrungsschatz und es wird nicht zuletzt durch die gute Zusammenarbeit getragen.
- Dr. Hans Rudolf Elsener von der Empa. In der Zusammenarbeit wurden die versiegelten Diodenkörper und Detektorkörper hergestellt. Zudem sind die Ergebnisse der DSA-Messungen zentral dafür gewesen, die Versiegelung der Diodenkörper erfolgreich umzusetzen.
- Dr. Lisa Löbling und Alexander Landstorfer für ihre offenen Ohren, nicht nur bei den Sternatmosphären. Allen weiteren Kolleginnen und Kollegen am IAAT, insbesondere Dr. Chris Tenzer, der sich immer für die Belange des Instituts engagiert und somit eine angenehme Arbeitsatmosphäre

schaft, und allen, die mit ihrer aktiven Teilnahme den Journal Club bereichert haben.

- Meinen Freunden, inklusive meinen Mitbewohnerinnen und Mitbewohnern, deren Unterstützung und Verständnis mir in vielen Situationen sehr geholfen hat.
- Ganz besonderer Dank gebührt natürlich meiner Familie: meinen Eltern Brigitte und Claudio Conti, meiner Schwester Dr. Natalia Sterz und meinem Schwager Ludwig Sterz, meiner Frau Isabell Alsheimer und meiner Schwiegerfamilie, Annette, Gerd und Johannes Alsheimer, die mir den Rückhalt geschenkt haben, der die Voraussetzung dafür ist, eine solche Arbeit verfassen zu können. Vielen Dank, dass ihr mich so gut unterstützt habt!

Abschließend danke ich folgenden Institutionen für ihre Unterstützung:

- der *Universität Tübingen* und der guten Arbeit, die in den Dezernaten oftmals im Hintergrund geleistet wird.
- dem *Bundesministerium für Wirtschaft und Technologie*, das über das *Deutsche Zentrum für Luft- und Raumfahrt e. V.* (DLR) meine Arbeit im Rahmen der Projekte 50 QT 1501 und 50 QT 2001 finanziell unterstützt hat.